PH.D. DISSERTATION / TESIS DOCTORAL

UNIVERSIDAD
DE GRANADA

Programa de Doctorado en Física y Ciencias del Espacio

Activation properties of particles as cloud condensation nuclei

Fernando Rejano Martínez

Instituto Interuniversitario de Investigación del Sistema Tierra en Andalucía
Departamento Física Aplicada
Universidad de Granada

Grupo Física
de la Atmósfera

IISTA
Instituto Interuniversitario de Investigación
del Sistema Tierra en Andalucía

Unidad de
Excelencia
UGR

Editor: Universidad de Granada. Tesis Doctorales
Autor: Fernando Rejano Martínez
ISBN: 978-84-1195-100-5
URI: https://hdl.handle.net/10481/85724

UNIVERSIDAD DE GRANADA

DEPARTAMENTO DE FÍSICA APLICADA
GRUPO DE FÍSICA DE LA ATMÓSFERA

TESIS DOCTORAL

ACTIVATION PROPERTIES OF PARTICLES AS CLOUD CONDENSATION NUCLEI

Tesis presentada por D. Fernando Rejano Martínez para optar al título de Doctor por la Universidad de Granada.

Directores de la Tesis:

Dr. Francisco José Olmo Reyes
Catedrático de Universidad
Departamento Física Aplicada
Universidad de Granada

Dr. Gloria Titos Vela
Profesora de la UGR
Departamento Física Aplicada
Universidad de Granada

Granada, septiembre de 2023

El trabajo de investigación que se expone en la presente memoria, titulado: ***ACTIVATION PROPERTIES OF PARTICLES AS CLOUD CONDENSATION NUCLEI***, para aspirar al título de Doctor por la Universidad de Granada dentro del Programa de Doctorado en Física y Ciencias del Espacio que presenta D. Fernando Rejano Martínez, ha sido realizado en la Universidad de Granada gracias a la ayuda "*Contratos predoctorales de Formación de Profesorado Universitario (FPU) 2019* "(FPU19/05340) concedida por el Ministerio de Universidades, bajo la dirección de:

Directores de la Tesis:

Dr. Francisco José Olmo Reyes

Dra. Gloria Titos Vela

Doctorando

Fdo.: D. Fernando Rejano Martínez

El doctorando / *The doctoral candidate* D. Fernando Rejano Martínez y los directores de la tesis / *and the thesis supervisors* Dr. Francisco José Olmo Reyes y Dra. Gloria Titos Vela.

Garantizamos, al firmar esta tesis doctoral, que el trabajo ha sido realizado por el doctorando bajo la dirección de los directores de la tesis y hasta donde nuestro conocimiento alcanza, en la realización del trabajo, se han respetado los derechos de otros autores a ser citados, cuando se han utilizado sus resultados o publicaciones.

Guarantee, by signing this doctoral thesis, that the work has been done by the doctoral candidate under the direction of the thesis supervisor/s and, as far as our knowledge reaches, in the performance of the work, the rights of other authors to be cited (when their results or publications have been used) have been respected.

Granada, septiembre de 2023

Directores de la Tesis / *Thesis supervisors*

Fdo.: Dr. Francisco José Olmo Reyes

Fdo.: Dra. Gloria Titos Vela

Doctorando / *Doctoral candidate*

Fdo.: D. Fernando Rejano Martínez

A mi familia

To my family

“Don’t adventures ever have an end?
I suppose not.
Someone else always has to carry on the story”
J.R.R Tolkien

Agradecimientos

Tras prácticamente cuatro años desde que inicié mi pequeña historia en este gran grupo de investigación que es el GFAT, en el cual se van recopilando año tras año tantas historias de mucha gente y que, al final, constituye la historia de nuestro grupo, quiero agradecer todo lo vivido y aprendido como un miembro más. Un grupo donde los que llegan tratan de continuar la historia que otros empezaron, de manera que este ciclo se va sucediendo en el tiempo y las historias (esas líneas de investigación) que nuestro querido GFAT va escribiendo, continúan sin tener un final. Esto es lo que yo he vivido durante mis años de doctorado en el CEAMA (o IISTA para los más modernos), que al final se resume en una maratón de aprendizaje continuo y que, llegado un tiempo, también uno tiene que saber transmitir a otra gente para que estos puedan continuar y perfeccionar la historia que uno empezó. Como dice el refrán "es de bien nacido ser agradecido", por eso quiero poner la guinda al pastel con estos párrafos finales.

Quiero empezar por el principio de esta historia. Por eso, en primer lugar, tengo que agradecer a mis directores de tesis: Dr. Francisco José Olmo y Dra. Gloria Titos. Gracias, Paco, por darme la oportunidad de incorporarme al GFAT y abrirme el mundo de la investigación de la atmósfera, cosa que en un principio yo no había considerado. Tú me ofreciste la oportunidad de subirme "a bordo" del GFAT y así lo hice. Si no fuera por tu experiencia investigadora durante tantos años y la calidad científica del GFAT, gracias también al Dr. Lucas Alados (capitán de este barco), no hubiese sido posible obtener el contrato FPU que me ha permitido investigar durante estos años. Por otro lado, quiero agradecer en mayúsculas a quien ha sido mi referente en el día a día de cómo hacer las cosas con rigor científico y que tanto me ha enseñado en estos años: Gloria Titos. Gracias, Gloria, porque durante estos

años me has enseñado qué es ser científico y si he progresado en algo ha sido gracias a tu paciencia (cuántas veces me habrás corregido los mismos errores…) y la disponibilidad de tiempo que siempre me has mostrado (ya sean domingos o incluso en vacaciones). Durante esta maratón siempre estabas ahí para echar una mano, revisar y corregir (siempre con una de cal y otra de arena) o encontrar la solución a los problemas que yo no les veía salida. Por eso no hay palabras para describir todo lo que me has aportado durante esta tesis doctoral y has conseguido que en mi cabeza se grabe una máxima importantísima en esta vida: "*Despacito y buena letra, que el hacer las cosas bien importa más que el hacerlas*". Muchas gracias a mis directores de tesis porque sin vosotros no hubiese sido posible alcanzar la meta.

Me gustaría mencionar ahora a todas aquellas personas que me han acompañado durante estos años y que han sido de vital importancia. Cómo no, agradecer a quien ha sido un referente cercano y lo más parecido a un "hermano mayor" científico: Dr. Juan Andrés Casquero Vera. Gracias por tu compañía y disponibilidad para echar un mano en lo que fuera necesario, pero sobre todo por tus consejos de quien se ha topado con las mismas situaciones previamente. Esas frases de gran ayuda… desde "cuál es el objetivo del trabajo" o "hay que estructurar mejor las ideas" hasta "¡Fernando, espabila!" o "si eso ya te lo dije hace tiempo". También quiero agradecer a quien me marcó mucho durante mis primeros años, Dr. Hassan Lyamani uno de los auténticos maestros del GFAT y que tantos frutos ha dejado durante su larga trayectoria. Gracias por tus sabios consejos y discusiones que ayudan a pensar más profundamente y, sobre todo, por esos buenos ratos de conversación entre cervezas en *La Cabaña*, donde como decíais Juan Andrés, Jose Benavent, Daniel Pérez y tú: "Aquí es donde se hace ciencia realmente". En cada historia siempre hay gente que está presente en todas las situaciones a la que te enfrentas y su compañía ayuda a que puedas superar todos los obstáculos que te encuentras, por eso tengo que mencionar a Andrea Casans (nuestra aragonesa de

Triana). Sin duda, ha sido la persona del GFAT con la que más tiempo he pasado durante estos cuatro años, con lo que eso conlleva: horas y horas de laboratorio, largas discusiones, muchas risas y también enfados, momentos de euforia y frustración, en función de cómo salieran los resultados. Gracias por todo el apoyo prestado durante este tiempo y, sobre todo, por la innumerable lista de anécdotas absurdas que han ido ocurriendo durante estos años que, obviamente, no puedo comentarlas en estas páginas.

También me gustaría agradecer al resto de los miembros del GFAT con los que he compartido tantas reuniones y horas de trabajo (en particular, Alberto Cazorla y nuestras subidas a Sierra Nevada, que empezaron allá por 2019) o, simplemente, he disfrutado de vuestra compañía en el día a día durante este tiempo. Desde los más veteranos que me habéis conocido y acogisteis desde que llegué al grupo (mención especial a Daniel y sus continuas bromas absurdas) hasta toda la nueva hornada de miembros del GFAT conocidos como "GFATILLOS". Este grupo tan diverso, que recoge personajes de lo más variopinto (desde Euskadi hasta Cádiz y Huelva, pasando por Extremadura y Almería, e incluyendo el continente americano). A estos últimos, y no por ello menos importantes, tengo que agradecer los buenos ratos de desconexión y risas durante las comidas o las míticas cervezas de los viernes, que tan importantes son para sobrevivir en los momentos más duros. También mencionar a mis queridos granadinos-polacos Pablo y Fátima por los buenos ratos compartidos estos años. Gracias a TODOS los miembros de la familia GFAT, que tan numerosa y diversa es, por las buenas experiencias compartidas y las enseñanzas aprendidas.

I switch to English to thank Prof. Paul Zieger for giving me the opportunity to join his group at ACES for a few months during my research stay in Stockholm. I am greatly acknowledged to Paul and Gabriel for your help and your willingness to discuss scientific topics during those *Fika* times. I would also like to thank Rahul

and Theo for the good times we shared both at the university and playing pool in *RoQ* bar.

Finalmente, me gustaría acabar agradeciendo a mis amigos y mi familia que durante estos años me han ido acompañando y apoyando en la realización de esta tesis doctoral. Primero agradecer en general el cariño mostrado por todos vosotros a través de esas preguntas inocentes (como por ejemplo “Oye y ¿qué tal van las nubes?” o ¿Cuándo saldrás en la tele dando el tiempo?”) que realmente esconden un sincero interés en qué las cosas me vayan bien. Me gustaría hacer mención especial a mi amigo Alfredo quien por circunstancia de la vida ha coincidido conmigo durante mis etapas de grado, máster y doctorado. Creo que solo por escucharme durante tantos años podrías convalidar varias asignaturas de Física. Gracias por tu compañía y tus ánimos, sobre todo en los momentos de mayor cansancio y colapso mental (tomarse algo fresquito lo cura todo). El agradecimiento más importante va sin lugar a duda a mis padres a quien les debo TODO: por darme la vida, la familia y la educación que me ha permitido llegar hasta aquí, sin ellos nada de esto hubiese sido posible. Gracias por darme el regalo de esta familia tan numerosa que ha resultado ser una escuela de valores y experiencias que no tiene precio. Agradecer a todos mis hermanos (María, José, Antonio, Ángeles y Ana) por su compañía y amistad durante toda mi vida, ya que al fin y al cabo han ido configurado la persona que soy. Este trabajo ha sido posible gracias a todos vosotros.

Contents

Abstract

This PhD dissertation focuses on the activation properties of aerosol particles as cloud condensation nuclei (CCN) to improve the existing knowledge on how aerosol particles evolve in the atmosphere to become effective CCN. To this end, physicochemical properties of atmospheric aerosol particles and their activation properties as CCN have been analyzed using ground-based in-situ techniques at two different environments.

To study the activation properties of aerosol particles at the height where clouds might form and asses the influence of anthropogenic influence at remote sites, firstly, the CCN activation properties of aerosol particles are characterized at two different sites in southern Spain: an urban background station in Granada city and a high-altitude mountain station in the Sierra Nevada National Park, with a horizontal separation of 21 km and vertical distance of 1820 m. CCN activity of aerosol particles at the urban environment is driven by primary sources, mainly road traffic. High CCN concentrations occurred during traffic rush hours, although this was also when the fraction of activated particles over total particles was the lowest. This is due to the characteristics of the rush hour aerosol population consisting of ultrafine and less hygroscopic particles. In contrast, the mountain site exhibited larger and more hygroscopic particles, with CCN activity driven by the joint effect of new particle formation (NPF) events and subsequent growth and vertical transport of anthropogenic particles from Granada urban area by orographic buoyant upward flow. This led to the maximum concentrations of CCN and aerosol particles occurring at midday at the mountain site. Clear differences in the diurnal evolution

of CCN between NPF event days and nonevent days were observed at the Sierra Nevada station, demonstrating the large contribution of newly formed particles to CCN concentrations after growth. The isolated contribution of NPF to CCN concentration has been estimated to be 175% higher at supersaturation ratio of 0.5% relative to what it would be without NPF events, revealing that CCN concentrations can be highly modified during these events. Also, two empirical models were proposed to parameterize CCN concentrations in terms of aerosol optical or physical parameters. The models could explain measurements successfully at the urban station, whereas at the mountain site both models could not reproduce satisfactorily the observations probably due to the aerosol properties changes caused by upslope transport of urban particles and NPF events.

As urban particles were found to affect the CCN activity at the mountain site during summer and autumn, a new field campaign was performed at the urban site during summer to get a deepen insight of the different aerosol sources and processes affecting urban aerosol particles and disentangle its influence on the CCN concentrations. An unsupervised clustering model was used to classify the main aerosol categories and processes occurring in the urban atmosphere and then, the influence of the identified aerosol populations on the CCN properties was analyzed. According to the physical properties of each cluster, its diurnal timing, and additional air quality parameters, the clusters were grouped into five main aerosol categories: nucleation, growth, traffic, aged traffic, and urban background. The results showed that aged traffic and urban background categories are the most efficient CCN sources. By contrast, traffic category was observed as the main aerosol source with the highest frequency of occurrence (32%), however, its impact in the CCN activity is very limited likely due to lower particle mean diameter and hydrophobic chemical composition. Similarly, nucleation and growth categories, associated to NPF events, present high total particle number concentration with large frequency of occurrence (22% and 28%, respectively) but the CCN concentration

for these categories is about half of the CCN concentration observed for the aged traffic category. Overall, these results showed the limited direct influence of traffic emissions on the CCN budget, however, when these particles undergo ageing processes, they have a significant influence on the CCN concentrations and may be an important CCN source (aged traffic category showed activation fraction of 0.41 at supersaturation ratio of 0.5%). Thus, urban particles could be transported to other remote environments, where clouds might form, modifying the CCN budget at those sites.

Finally, to improve the CCN predictive capability at the high-altitude mountain site and understand the aerosol properties changes at this site, a new field campaign was performed focused on the chemical composition of particles and its relation to the activation properties. A more direct method to calculate CCN based on particle number size distribution measurements and aerosol hygroscopicity was investigated. At this site the sub-micron aerosol mass concentration was constituted of 70% of organic aerosol and, therefore, play a crucial role in defining the overall aerosol hygroscopicity. Different organic aerosol schemes were proposed to assess the organic hygroscopicity influence on CCN prediction. The main organic aerosol sources were identified using the Positive Matrix Factorization method. Results revealed the predominance of secondary organic aerosol with high degree of oxidation in the overall aerosol population. The CCN closure for all organic schemes showed good agreement with observations, with slope and correlation coefficients between predicted and measured CCN concentrations of 1.02-1.40 and 0.89-0.94, respectively, depending on the prediction scheme. However, when the aerosol population is affected by the atmospheric boundary layer (ABL) during morning and midday hours (affected by vertical transport of particles or NPF events), predicted CCN concentrations overestimate the measurements in a wider range (from 0 to 35%). These results evidenced that detailed knowledge of organic sources and organic hygroscopicity are not sufficient to obtain reliable CCN predictions at

all atmospheric conditions, especially during ABL influence conditions. Thus, even at mountain environments where the aerosol population shows typically free troposphere conditions, changes on the aerosol properties and mixing state conditions might play a crucial role in CCN predictions.

Resumen

Esta tesis doctoral se centra en el estudio de las propiedades de activación de partículas del aerosol atmosférico como núcleos de condensación de nubes (CCN), con el fin de mejorar el conocimiento existente sobre cómo evolucionan las partículas en la atmósfera para convertirse en CCN efectivos. Para llevar a cabo este objetivo se han analizado las propiedades fisicoquímicas de las partículas y sus propiedades de activación como CCN mediante técnicas in-situ en dos entornos diferentes.

Para estudiar las propiedades de activación de las partículas del aerosol como CCN a la altura a la que podrían formarse las nubes y evaluar la influencia antropogénica en ambientes remotos, en primer lugar se han caracterizado las propiedades de activación de las partículas en dos emplazamientos diferentes del sur de España: una estación urbana en la ciudad de Granada y una estación de montaña de gran altitud en el Parque Nacional de Sierra Nevada, con una separación horizontal entre ambas de 21 km y vertical de 1820 m. La actividad de las partículas del aerosol como CCN en el entorno urbano está controlada por fuentes primarias, principalmente el tráfico rodado. Se observaron altas concentraciones de CCN durante las horas punta de tráfico, coincidiendo con valores bajos de la fracción de activación. Esto se debe a las características de la población de partículas del aerosol durante las horas de mayor influencia del tráfico, que está dominada por partículas ultrafinas y de baja higroscopicidad. Por el contrario, en el emplazamiento de montaña se observó la presencia de partículas de mayor tamaño y caracterizadas por una mayor higroscopicidad. Estas características están relacionadas con una

actividad de CCN impulsada por el efecto conjunto de los eventos de formación de nuevas partículas (NPF) y el transporte vertical de partículas antropogénicas desde la zona urbana de Granada por flujo ascendente orográfico. Esta situación atmosférica conlleva concentraciones máximas de CCN y partículas del aerosol a mediodía. En la estación de Sierra Nevada se observaron claras diferencias en la evolución diurna de los CCN entre los días con y sin eventos de NPF. Se ha estimado que la contribución aislada de los NPF a la concentración de CCN a sobresaturaciones de vapor de agua (SS) de 0.5% es un 175% mayor en relación con lo que sería un día sin NPF, revelando que las concentraciones de CCN pueden ser altamente modificadas durante los eventos de NPF. Asimismo, se han propuesto dos modelos empíricos para parametrizar las concentraciones de CCN en términos de parámetros ópticos o físicos de las partículas del aerosol para ambas estaciones de medida. Los modelos propuestos explican satisfactoriamente las medidas en la estación urbana, mientras que en la estación de montaña ninguno de los modelos reproduce satisfactoriamente las observaciones, probablemente debido a los cambios en las propiedades de las partículas causadas por el transporte de las partículas urbanas desde alturas más bajas y los eventos de NPF.

Dado que se observó que las partículas del aerosol urbano afectaban a la actividad de los CCN en el emplazamiento de montaña durante el verano, se llevó a cabo una nueva campaña en el emplazamiento urbano durante el verano para obtener una visión más profunda de las diferentes fuentes y procesos que afectan a las partículas y desentrañar su influencia en las concentraciones de CCN. Se utilizó un modelo de agrupamiento o *clustering* para clasificar las principales categorías de partículas y los procesos que tienen lugar en la atmósfera urbana y, a continuación, se analizó la influencia de las poblaciones de partículas identificadas en las propiedades de los CCN. De acuerdo con las propiedades físicas de cada grupo, su patrón de variación diurna y parámetros adicionales, los *clústers* se agruparon en cinco categorías principales de partículas: nucleación, crecimiento, tráfico, tráfico

envejecido y fondo urbano. Los resultados mostraron que las categorías de tráfico envejecido y fondo urbano son las fuentes de CCN más eficientes. Por el contrario, la categoría de tráfico se observó como la principal fuente de partículas del aerosol y con la mayor frecuencia de observación (32% de todos los datos), sin embargo, su impacto en la actividad CCN es muy limitado debido al menor diámetro medio de las partículas y a su composición química hidrófoba. De forma similar, las categorías de nucleación y crecimiento, asociadas a eventos NPF, presentan grandes concentraciones de partículas y gran frecuencia de ocurrencia (22% y 28%, respectivamente), pero la concentración de CCN para estas categorías es aproximadamente la mitad de la concentración de CCN observada para la categoría de tráfico envejecido. En general, estos resultados muestran que la influencia directa de las emisiones de tráfico en la concentración de CCN es limitada, sin embargo, cuando estas partículas sufren procesos de envejecimiento, tienen una influencia significativa en las concentraciones de CCN y pueden ser una fuente importante de CCN. Así, las partículas urbanas podrían ser transportadas a otros entornos remotos modificando la concentración de CCN en esos lugares, donde sí se pueden dar las condiciones para la formación de una nube.

Por último, para mejorar la capacidad de predicción de la concentración de CCN en el emplazamiento de alta montaña y comprender los cambios en las propiedades de las partículas del aerosol en este emplazamiento, se realizó una campaña de medidas centrada en el estudio de la composición química de las partículas y su relación con las propiedades de activación como CCN. Se llevó a cabo un método más directo para calcular las concentraciones de CCN basado en medidas de la distribución de tamaño del aerosol y el cálculo del parámetro de higroscopicidad utilizando medidas de la composición química. En este emplazamiento, la concentración másica del aerosol submicrométrico estaba constituida en un 70% de aerosol orgánico y, por tanto, los compuestos orgánicos desempeñan un papel crucial en la definición de la higroscopicidad total del aerosol.

Se propusieron diferentes esquemas de higroscopicidad de las partículas orgánicas para evaluar la influencia de la higroscopicidad de los compuestos orgánicos en la predicción de la concentración de CCN. Las principales fuentes de partículas orgánicas se identificaron mediante el método de Factorización Matricial Positiva. Los resultados evidenciaron el predominio de partículas orgánicas secundarias con alto grado de oxidación en la población total del aerosol en Sierra Nevada. Las predicciones de CCN para todos los esquemas de orgánicos mostraron un buen acuerdo con las observaciones, con pendientes y coeficientes de correlación entre las concentraciones de CCN predichas y medidas de 1.02-1.40 y 0.89-0.94, respectivamente, dependiendo del esquema de predicción. Sin embargo, cuando la población de partículas se ve afectada por la influencia de la capa límite atmosférica (ABL) durante las horas de la mañana y del mediodía (afectada por el transporte vertical de partículas o por eventos de NPF), las concentraciones de CCN predichas sobreestiman las medidas en un rango más amplio (de 0 a 35%). Estos resultados demuestran que el conocimiento detallado de las fuentes del aerosol y la higroscopicidad de los compuestos orgánicos no son suficientes para obtener predicciones fiables de CCN en todas las condiciones atmosféricas, especialmente durante las situaciones de influencia de la ABL. En este sentido, incluso en entornos de montaña donde la población de partículas del aerosol se espera que muestren condiciones típicas de troposfera libre, los cambios en las propiedades de partículas y las condiciones del estado de mezcla de estas podrían desempeñar un papel crucial a la hora de predecir los CCN.

1 Introduction

Climate change is nowadays one of the most important trending topics because it directly affects our lifestyle, welfare and even it has become a topic for discussion by policymakers. The increase in the frequency and intensity of some atmospheric phenomena (such as intensity of hot extremes, heatwaves, heavy precipitation, intense tropical cyclones, reduction of Arctic ice cover and permafrost) reveals a global climate change which is due to the perturbation in the Earth's energy balance and the associated changes in surface temperature (IPCC 2021). Comprehending the mechanisms driving these impactful changes is a crucial scientific challenge.

Radiative forcing is a concept used in climate science to quantify the perturbation in the Earth's energy balance caused by changes in the atmosphere and the Earth's surface. It is a measure of the ability of a specific factor, for example greenhouse gases or solar radiation, to alter the amount of energy that enters or leaves the Earth's atmosphere, affecting global climate. Thus, understanding radiative forcing drivers is essential for assessing the potential climate impacts of different human activities and natural processes. Climate models use radiative forcing to project future climate changes and to evaluate the effectiveness of climate change mitigation strategies. In this sense, the Intergovernmental Panel on Climate Change (IPCC) Sixth Assessment Report (AR6) on the physical science basis of climate change states that overall factors affecting the radiative forcing the one with the greatest uncertainty associated with it is the atmospheric aerosol (IPCC, 2021).

Atmospheric aerosol consists of those solid or liquid particles suspended in the atmosphere, excluding clouds (Horvath, 2000). Aerosol radiative forcing is due to two different interaction mechanisms between aerosol particles and radiation. The

first mechanism consists of the direct absorption or scattering of solar and terrestrial radiation by aerosol particles. It is called the direct effect of atmospheric aerosol or aerosol-radiation interactions (ARI). The second mechanism consists of the cloud properties adjustments, such as changes in cloud droplet number concentration (CDNC) or cloud droplet size, because aerosol particles serve as seeds upon which cloud droplets form and involve changes in cloud radiative properties. This is the so-called indirect effect of aerosol or aerosol-cloud interactions (ACI). The AR6 attributes for atmospheric aerosol with *medium confidence* a net effective radiative forcing of -1.1 [-1.7 to -0.4] Wm^{-2} (Figure 1-1), accounting ACI for the 75-80% of the total uncertainty (IPCC, 2021). Therefore, the impact of aerosol particles on clouds (i.e., ACI) is the least understood radiative forcing mechanism and improving the scientific knowledge of ACI will allow us to develop better predictions of global climate models (Seinfeld et al., 2016) and potential mitigation strategies.

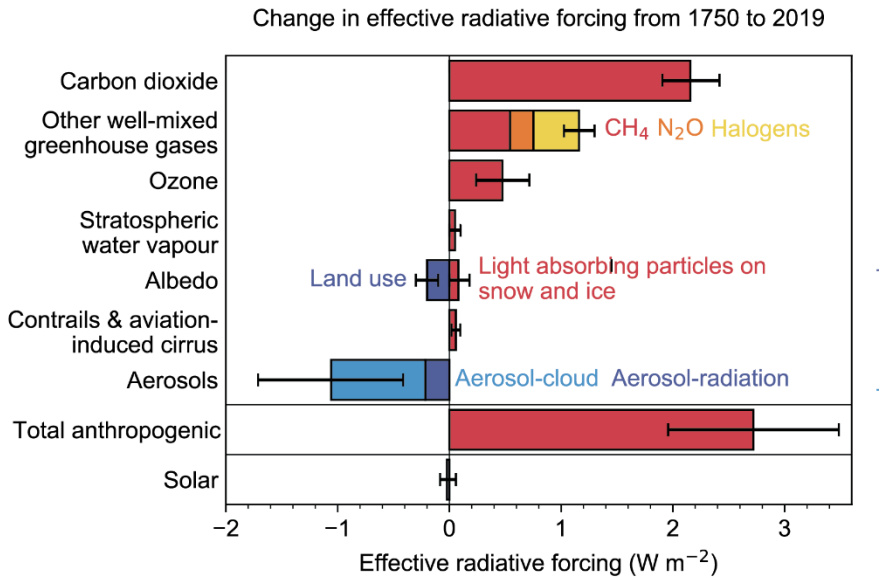

Figure 1-1. IPCC radiative forcing panel. Figure adapted from Chapter 7 of IPCC AR 6, 2021.

Aerosol-cloud interactions (ACI) are driven by a subset of aerosol particles that can form cloud droplets and are known as cloud condensation nuclei (CCN).

Changes in the available amount of CCN in the atmosphere or in their properties can affect cloud radiative properties, cloud lifetime and/or precipitation efficiency (Lohmann and Feichter, 2005). For example, in warm clouds when the CCN concentration is high then CDNC increases (for a fixed cloud liquid water content), but the droplet size decreases. This fact causes a bigger droplet surface area that can interact with radiation, resulting in a higher cloud albedo (Twomey, 1977). Besides, a reduction in the cloud droplet size may retard and reduce precipitation and may increase the cloud lifetime (Albrecht, 1989). Thus, CDNC and cloud droplet size are the main variables linking aerosol and cloud properties and depend on CCN properties and cloud updraft velocity (Pruppacher and Klett, 2010; Reutter et al., 2009). Reducing the uncertainty of global CCN simulations by a certain amount implies a two-fold reduction in the uncertainty of CDNC (Karydis et al., 2012; Moore et al., 2013; Sotiropoulou et al., 2006), which is the parameter used by global climate models to calculate climate predictions and asses aerosol indirect effect. Therefore, reducing the uncertainty in aerosol particles and CCN simulations is necessary to increase our confidence in global climate models (IPCC, 2021). One of the leading causes of this uncertainty is a lack of broad knowledge about particle sources and how particles evolve to become effective CCN (Fanourgakis et al., 2019). Thus, the quantification of CCN concentrations, the characterization of the relevant aerosol properties involved in the activation process as CCN, the identification of CCN sources and their temporal and spatial variability are critical aspects to reduce this uncertainty (e.g., Crosbie et al., 2015; Dusek et al., 2006; Paramonov et al., 2015; Schmale et al., 2018).

The main aerosol properties affecting the CCN activity, if ambient conditions that regulate water vapor supersaturation ratio (SS) are disregarded, are size, chemical composition and mixing state of the aerosol population (e.g., Cubison et al., 2008; Deng et al., 2018; Dusek et al., 2006; Kuang et al., 2020; Wang et al., 2010). Particle number size distribution (PNSD) is the main factor controlling CCN

activity (Crosbie et al., 2015; Dusek et al., 2006) since the larger the aerosol particle size the less ambient SS it will need to form a cloud droplet (Köhler, 1936). In this sense, several studies explained the activation properties of aerosol particles and temporal variability of CCN number concentrations (N_{CCN}) in terms of the PNSD (Bougiatioti et al., 2020; Cheung et al., 2020), because PNSD provides valuable insights into the formation, transformation and removal processes of the aerosol population (Beddows et al., 2009; Rivas et al., 2020). Moreover, PNSD measurements make possible to identify atmospheric aerosol sources (Brines et al., 2015; Charron et al., 2008; Costabile et al., 2009; Salimi et al., 2014), while the temporal evolution of the PNSD allows to observe atmospheric processes such as nucleation, coagulation, condensation and/or deposition (Tunved et al., 2004). Thus, PNSD is a key property to understand how aerosol particles evolve in the atmosphere to become CCN.

Secondly, aerosol chemical composition affects the CCN activity because it determines its hygroscopicity, which refers to the ability to take up water from the surrounding environment when exposed to higher relative humidity (RH) levels. Depending on the chemical composition, aerosol particles can absorb water efficiently and grow when RH increases, showing hygroscopic growth. For example, inorganic salts or some organic species are considered hygroscopic particles (Svenningsson et al., 2006), while elemental carbon (EC) or dust do not show a clear hygroscopic growth and are considered non-hygroscopic aerosol particles (Weingartner et al., 1997). The effect of chemical composition on CCN activity is usually treated through the hygroscopicity parameter κ (Petters and Kreidenweis, 2007), which parameterizes the aerosol hygroscopic behavior through a simple volume mixing rule of the different chemical species present in the aerosol population. In this way, an accurate characterization of κ allows to explain better N_{CCN} spatial and temporal variability (e.g., Cai et al., 2018, 2020; Hoyle et al., 2016; Mei et al., 2013). While aerosol hygroscopicity of inorganic species is well defined,

the water uptake capacity of organic aerosol (OA) is poorly understood since OA includes a large variety of compounds exhibiting a wide range of κ values (Hallquist et al., 2009; Jimenez et al., 2009; Zhang et al., 2007). Accurate characterization of OA hygroscopicity (κ_{OA}) is challenging but it may be crucial to quantify N_{CCN} at OA dominated sites (Cai et al., 2022; Deng et al., 2019; Gunthe et al., 2009; Liu and Wang, 2010; Thalman et al., 2017). Other factors such as mixing state and size-resolved chemical composition have recently been suggested of foremost importance for accurately define the overall κ of the aerosol population (Riemer et al., 2019). However, the amount of information about the aerosol population needed for an accurate quantification of the CCN budget depends strongly on the variety of aerosol sources and atmospheric processes involved.

In the last years, several ambient CCN studies have been performed to characterize the activation properties of aerosol particles in a wide variety of atmospheric conditions. Most CCN studies are carried out during specific measurement campaigns with special atmospheric conditions, such as fog events (Hammer et al., 2014; Motos et al., 2019), Saharan dust episodes (Weger et al., 2018), biomass burning events (Bougiatioti et al., 2016; Chen et al., 2019; Z. Wu et al., 2017) or urban polluted conditions (Duan et al., 2018). Among all atmospheric conditions, N_{CCN} observations during new particle formation (NPF) events (Dameto de España et al., 2017; Gordon et al., 2017; Kalkavouras et al., 2019; Kerminen et al., 2012; Leng et al., 2014; Rose et al., 2017) have gained significant relevance since aerosol number concentration is likely to be dominated by NPF events in remote sites (O'Dowd et al., 2002). According to Merikanto et al. (2009), 45% of global low-level cloud CCN originates from NPF, and 35% of the remaining CCN are formed in the free and upper troposphere. Gordon et al. (2017) pointed out that NPF produces around 50% of CCN at low supersaturations globally. However, the contribution of NPF to CCN concentration is highly dependent on the environment where it takes place, since NPF variability and intensity varies strongly from one

environment to another (Kerminen et al., 2018). At urban sites, NPF can enhance the CCN population between 20 and 40% at low or medium SS values (Dameto de España et al., 2017; Leng et al., 2014). However, at remote sites (e.g., mountain stations) NPF can be the major CCN source, increasing the CCN concentration up to 250% (Rose et al., 2017).

CCN activity shows a high spatial variability due to the strong influence of aerosol sources, which are site-dependent (Schmale et al., 2018). Overall sites, urban areas are the most important contributor to the aerosol number concentration, especially of ultrafine particles (UFP, particles with diameter < 100 nm) due to the anthropogenic activity (traffic, industry, biomass burning or domestic heating systems). Because of this, high CCN concentrations have been observed in urban areas (Burkart et al., 2011; Che et al., 2016; Ren et al., 2018; Zhang et al., 2017), even though the CCN activation efficiency is lower than in remote sites (Cheung et al., 2020; Cubison et al., 2008; Kim et al., 2014; Schmale et al., 2018) due to the less hygroscopic behavior of urban particles (Burgos et al., 2019; Titos, et al., 2014). In this sense, urban areas are very interesting sites to explore how activation properties of aerosol particles are influenced by a great variety of emission sources and complex atmospheric processes that take place (Wu and Boor, 2021) and assess the anthropogenic influence on the CCN activity. While the highest CCN concentrations are observed in urban environments, high-altitude remote sites (like mountain sites) are even more crucial for the investigation of CCN activity since they are located at the height where atmospheric conditions favor the formation of clouds. Mountain sites are often located in the free troposphere (Rose et al., 2017; Venzac et al., 2009), however, in some circumstances these sites can be influenced by polluted air injected from lower altitudes (Asmi et al., 2011; Ripoll et al., 2015). Therefore, to have a broad knowledge of the activation properties of aerosol as CCN, research is needed in both urban environments and at mountain sites that can be at times under the influence of anthropogenic emissions during specific circumstances.

To date, this kind of studies performing a joint analysis of CCN at interconnected sites and investigate how they are related are scarce (Zhang et al., 2017).

In addition to urban and mountain sites, further information of CCN concentration and activation properties are needed in a global scale. CCN measurements are relatively scarce and are routinely measured only at a handful of observatories worldwide, with most measurements being performed in campaign-based studies (Schmale et al., 2017). To overcome the limited number of direct CCN measurements, empirical models that use other more commonly measured aerosol properties (like optical properties or PNSD) as proxies of N_{CCN} (Jefferson, 2010; Shen et al., 2019) could contribute to improve our understanding of the spatial and temporal variability of CCN data and, hence, reduce indirect aerosol forcing uncertainty. Those measurements are carried out at a good number of sites, in contrast to CCN measurements, within well-stablished international measurement networks such as NFAN (NOAA Federated Aerosol Network) (Andrews et al., 2019) or ACTRIS (Aerosols, Clouds, Trace gases Research Infrastructure) (Laj et al., 2020). To evaluate the performance of existing methods and/or develop new CCN parameterizations valid at multiple environments, collocated measurements of CCN and aerosol properties at different sites with distinct aerosol properties and affected by different atmospheric conditions are necessary.

1.1 Objectives and outline

The research activities developed in this thesis have the main objective of advancing in the understanding of aerosol activation as CCN and disentangling the influence of different aerosol sources and atmospheric processes on the CCN budget at complex environments.

The thesis dissertation is organized in several chapters, as indicated in the following outline:

Chapter 2 is devoted to the basic concepts behind the aerosol science needed to follow this thesis. The main properties of aerosol particles influencing their activation as CCN are explained, also the sources and processes affecting ambient aerosol particles are described. The physical basis about how cloud formation process occur in the atmosphere is briefly explained. Finally, the κ-Köhler theory is exposed as the main theory that explains the activation of particles as cloud droplets.

Chapter 3 presents a detailed description of the study area and the experimental stations together with a short description of the main instrumentation employed in this thesis.

Chapter 4 deals with the methodological aspects of the thesis and presents how the different parameters that characterize the activation properties of aerosol particles have been obtained from the measurements described in Chapter 3. The statistical methods and data analysis tools used to obtain the results are also presented.

Chapter 5 focuses on the relationship between aerosol particles and their activation properties at two contrasting environments (Sierra Nevada mountains and Granada urban area). The main aim of this chapter is to explore the factors controlling the CCN budget at each site, as well as the interaction between aerosol emissions and transformation processes taking place at both locations.

Chapter 6 digs deeper in the aerosol sources and atmospheric processes affecting CCN concentrations and activation properties at the complex environment of Granada urban area. This chapter shows the results of the classification of the main aerosol categories/populations occurring in the urban environment based on a clustering model applied to the particle number size distribution. The CCN properties of each aerosol category are investigated revealing how specific aerosol sources or processes affect the aerosol activation properties.

Chapter 7 continues with the study of aerosol sources and their impact on CCN properties and their predictive capability focusing on the Sierra Nevada high-altitude remote site. In this case, more attention is paid to the chemical composition, in particular to the organic fraction. The main organic sources are identified applying Positive Matrix Factorization to the measured chemical composition obtained with an online mass spectrometer. This chapter shows how the hygroscopicity related to the organic particles affect CCN observations and explores the performance of different prediction methods to estimate the CCN concentration.

Finally, Chapter 8 presents a summary of the main conclusions of this thesis together with an outline of future research.

2 Fundamentals

2.1 Atmospheric aerosol: properties, processes and sources

The atmosphere is defined as the layer of gases that envelops the Earth. However, it is known that this gaseous layer is not only composed by a mixture of gases (such as N_2, O_2, CO_2, among other trace gases). A deepen definition of the terrestrial atmosphere must include other observed components like clouds and atmospheric aerosol particles. Clouds consist of water droplets or ice crystals suspended in the atmosphere, whereas the atmospheric aerosol is defined as the suspension of solid and/or liquid particles in the atmosphere, excluding cloud components (Horvath, 2000). Although atmospheric aerosol is a trace component, they play an important role in climate due to the aerosol radiative forcing effect through the direct and indirect effects (explained in Chapter 1). Also, aerosol particles have an important impact on human health since they can be breathed by human beings and enter in the respiratory and circulatory system (Cassee et al., 2019). Among these main effects, aerosol particles can have a negative effect on other issues like decreasing atmospheric visibility, altering ecosystems and affecting the cultural heritage preservation (Grantz et al., 2003; Patrón et al., 2017). The effect of aerosol particles on each of these topics (climate, human health or ecosystems) will depend on their physicochemical properties such as size, chemical composition, density or morphology. The differences on aerosol physicochemical properties reveal the wide variety of particles present in the atmosphere which are emitted by many types of

sources and transformed in the atmosphere by several processes. Thus, atmospheric aerosol has a high spatial and temporal variability and introduce significant uncertainty in climate models (Lohmann and Feichter, 2005). A comprehensive description of the main features of atmospheric aerosol particles is presented below.

The main properties that characterize the aerosol particles are the particles size and chemical composition. Aerosol particles size ranges from few nanometers (early formed molecular clusters) to tens of micrometers (dust or pollen particles) in diameter. To assure the size comparability between particles with different shapes, the equivalent particle diameter (D_p) is introduced. It is defined as the diameter of a sphere that has the same volume of the particle. According to the D_p value, it is possible to characterize aerosol particles in two main groups: fine mode ($D_p < 1$ μm) and coarse mode ($D_p > 1$ μm) particles. In the framework of this thesis, only the aerosol fine mode will be studied due to its relevant impact on the CCN budget since it is the main contributor to the aerosol particle number concentration. In turn, the aerosol size distribution of the fine mode can be separated in 3 modes, which are related to different sources, formation processes and chemical composition:

- *Nucleation mode*: this mode encompasses the smallest particles with sizes ranging from 2-3 nm to 25 nm. It is the main mode of the particle number size distribution, but its contribution to the mass is the lowest. Particles are formed by nucleation of precursors gases to freshly formed particles. These particles show the shortest lifetime in the atmosphere, around hours, due to growth to larger sizes.
- *Aitken mode*: it is the second largest contribution to the particle number concentration. The typical size range is between 25-100 nm and includes a mixture of particles formed by different mechanism, such as coagulation of nucleation mode particles or direct emission during combustion processes.

Primary traffic emissions usually are in this size range (Morawska et al., 2008).

- *Accumulation mode*: this mode includes particles between 100 nm and 1 μm. One of the most important formation mechanisms of these particles is the growth of Aitken mode particles by the condensation of saturated vapors over these preexisting particles in the atmosphere. Also, coagulation of preexisting particles is another formation process for accumulation mode particles. Thus, these particles are commonly considered as aged particles showing the longest lifetime in the atmosphere due to their low removal efficiency. This mode is of particular relevance because of its influence on the CCN concentration in the atmosphere (Schmale et al., 2018).

Ambient aerosol particles consist of multi-components particles formed by different chemical species. The chemical composition of aerosol particles can be classified in these categories: organic aerosol (OA), inorganic aerosol (IA), elemental carbon (EC), mineral dust, sea salt and trace metals. All these chemical species exist in a wide range of sizes (mainly OA and IA), depending on their formation processes or emission sources (Figure 2-1) (McMurry, 2000). The majority of OA, IA and EC is found in the fine mode, whereas sea salt and mineral dust are mainly observed in the coarse mode (Seinfeld and Pandis, 1998).

Depending on their origin, aerosol particles can be classified as primary when they are directly emitted to the atmosphere in the particulate phase (such as sea salt, mineral dust, or EC), or secondary when the aerosol particles are formed from precursor gases through different formation processes via gas-to-particle conversion (a wide variety of OA and IA are considered secondary aerosol). Regarding the type of emission source, aerosol particles can be classified as natural or anthropogenic, which are associated to human activities. Natural aerosol particles such as sea salt, pollen particles, mineral dust from deserts are considered examples of primary

natural particles, whereas OA from biogenic volatile organic compounds (VOCs) or sulphate formed from SO_2 emitted by volcanoes are secondary natural particles. Natural particles are mainly from primary origin (estimated flux to the atmosphere of primary and secondary natural aerosol are around 2880 $Tg \cdot y^{-1}$ and 240 $Tg \cdot y^{-1}$) and are confined to the coarse mode (Seinfeld and Pandis, 1998). Also, natural particles are the largest contribution to the global aerosol mass. Anthropogenic particles can have a primary origin, such as incomplete fuel combustion or biomass burning, or secondary origin due to emissions of precursor gases (SO_2, NO_x, VOCs) associated with domestic heating, industry, and traffic emissions. These anthropogenic gases can promote the formation of secondary aerosol particles through nucleation. Anthropogenic particles are mainly from secondary origin and constitute most of the fine mode. Moreover, it is the major contribution to the global particle number concentration (Wu and Boor, 2021).

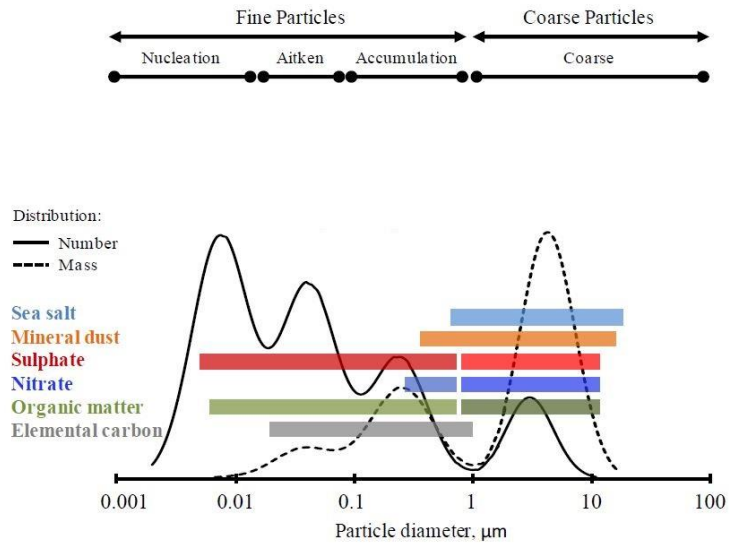

Figure 2-1. Aerosol size distribution (in number and mass) and the associated chemical species. The size range of each mode is specified in top of the figure. (Figure adapted from García et al. (2017)).

2.2 Cloud formation and thermodynamics

Together with aerosol particles, clouds are also the atmospheric constituents with the largest spatial and temporal variability in the atmosphere, contributing to its complexity. Clouds are constituted by a visible collection of water droplets suspended in the atmosphere and its formation is determined by ambient thermodynamic conditions. Considering a moist air parcel with a certain relative humidity (RH), the cloud formation process consists of the phase transition of the water vapor contained in the air parcel to form liquid water droplets, i.e., cloud droplets. A necessary condition (but not sufficient) for the cloud formation process is that the air parcel must be supersaturated, which means having a RH value higher than 100%. The RH value is just the percentage expression of the water vapor saturation ratio (S) which is defined as:

$$S = \frac{RH(\%)}{100} = \frac{P_{H_2O}}{P^0_{H_2O}(T)} \qquad \textbf{Eq. (2-1)}$$

where P_{H_2O} is the water vapor pressure in the air parcel and $P^0_{H_2O}$ is the saturation water vapor pressure. The dependence between $P^0_{H_2O}$ and T is established by the Clausius-Clapeyron equation, which involves that $P^0_{H_2O}(T)$ is a monotonically increasing function with T (Seinfeld and Pandis, 1998). In this sense, high values of RH in the atmosphere are usually reached due to the cooling of the air parcel. Among all the mechanisms by which an air parcel in the atmosphere can be cooled and reach supersaturated conditions, the two most important mechanisms are: adiabatic cooling and isobaric cooling. The following is a briefly explanation of each mechanism:

- *Adiabatic cooling*: in this mechanism the air parcel cooling is due to the ascension of the air parcel. When the air parcel ascends, then its pressure

decreases, and it expands its volume. If we assume that there is no heat exchange between the air parcel and the environment, consequently the air parcel temperature must decrease. Therefore, this mechanism is called adiabatic cooling. In this process we can define the *lifting condensation level* (LCL), which is the height at which the air parcel become saturated and is usually very close to the cloud base.

- *Isobaric cooling*: this cooling process of the air parcel occurs under a constant pressure, so the saturation conditions is achieved by decreasing the air temperature due to radiative losses or horizontal movement over a colder surface (land, water surface or another air mass). The temperature decrease involves a decrease in the saturation water vapor pressure and, therefore, RH increases. In this case, it is defined the temperature at which the air parcel becomes saturated, called as *dew point temperature*. For that reason, the dew point of a subsaturated air parcel is always lower than its actual temperature.

Once the air parcel becomes supersaturated ($S > 1$), the cloud formation might occur. In the framework of the thermodynamics, the phase transition of water from the gas phase (water vapor) to liquid phase (water droplets) can occur via two known processes: homogeneous nucleation or heterogeneous nucleation. The phase transition of water vapor to liquid phase is considered a homogeneous nucleation process when it takes place in the absence of any external material. In this case, the water vapor supersaturation should be extremely high to form water droplets and, therefore, does not occur in the atmosphere (Andreae and Rosenfeld, 2008). However, the water phase transition via heterogeneous nucleation consists of forming the liquid droplet from the water vapor in the presence of a solid surface, acting as a condensation nucleus. Therefore, if the supersaturated air parcel contains aerosol particles, which are ubiquitous in the atmosphere, these particles can act as cloud condensation nuclei. Cloud droplet formation is allowed through

heterogenous nucleation at low S values (few percent above RH=100%) and is the only pathway of cloud droplet formation in the atmosphere (Pruppacher and Klett, 2010). The ability of aerosol particles to act as CCN will be described in the next sub-section.

2.3 Activation of aerosol particles into droplets: κ-Köhler theory

The theoretical framework that describes mathematically if an aerosol particle can act as a CCN to form a droplet depending on the ambient *S* was stablished by the meteorologist Hilding Köhler. The classical Köhler theory describes the equilibrium saturation ratio (S_{eq}) over a droplet in terms of the droplet size and considering specific solution inside the droplet (Köhler, 1936). Note that droplets in the atmosphere are always considered as a solution (a solving solute in water) since there are no pure water droplets. In this sense, classic Köhler theory explains how water vapor pressure over a droplet is affected by considering an aqueous solution instead of pure water (solute effect or *Raoult effect*) and considering a curved surface instead of a flat surface (curvature effect or *Kelvin effect*). Both effects are briefly explained below:

- *Raoult effect*: it consists of the decrease of the saturation ratio when some solute particles are present in an aqueous solution. The water molecules concentration decreases due to the presence of solute particles in the surface of the solution and, therefore, the water vapor pressure over the solution is diminished (Raoult, 1887). This effect is quantified by the water activity (a_w) of a solution which is defined as the water vapor pressure of an aqueous solution (P_{sol}) divided by that of pure water (P_{H_2O}) at the same temperature:

$$a_w = \frac{P_{sol}}{P_{H_2O}} \qquad \textbf{Eq. (2-2)}$$

- *Kelvin effect*: this effect describes the increase of vapor pressure over a curved surface respect to a flat surface. The more curved is the surface, the higher increase of the vapor pressure at the surrounding of the surface is. The physical interpretation of the Kelvin effect is based on the fact that it is easier for molecules on the surface to escape to the gas phase if the surface is curved since there are fewer molecules adjacent for the considered molecule on the surface. Therefore, the vapor pressure over curved surface is higher than over a flat surface (S_{eq} for smaller droplets is always greater than for larger ones).

The Köhler equation accounts for both effects and establishes the mathematical relation between S_{eq} and the solution droplet diameter (D):

$$\ln S_{eq} = \frac{4M_w\sigma_w}{RT\rho_w D} - \frac{6n_s M_w}{\pi\rho_w D^3} \qquad \textbf{Eq. (2-3)}$$

where M_w, σ_w and ρ_w are the molecular weight, surface tension and density of pure water, respectively. The n_s is the number of solute moles, R is the universal gas constant and D is the droplet diameter. If we rewrite Eq. (2-3) grouping all the constants of each of the terms, we obtain the following simplified version of the Köhler equation:

$$\ln S_{eq} = \frac{A}{D} - \frac{B}{D^3} \qquad \textbf{Eq. (2-4)}$$

There are terms that determine S_{eq} and each term represents one of the two effects described before. The first term (A/D) represents the Kelvin effect which tend to increase S_{eq}, while the second term (B/D^3) represents the Raoult effect which decreases S_{eq}. Due to the dependence with D of each of the terms we can deduce that for large diameters the Kelvin effect dominates over the Raoult effect,

whereas for small diameters it is the Raoult effect which dominates over the Kelvin effect (Figure 2-2).

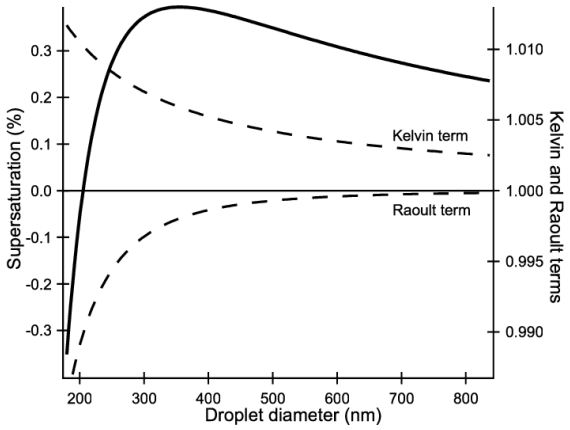

Figure 2-2. Example of a Köhler curve showing the separated contribution of Kelvin and Raoult effects on the equilibrium supersaturation. (Figure taken from Raatikainen and Laaksonen (2011)).

The Köhler curve, $S_{eq}(D)$, has always a maximum at a specific diameter value, called the critical droplet diameter (D_{crit}) whose value is determined by

$$D_{crit} = \left(\frac{3B}{A}\right)^{1/2} \qquad \textbf{Eq. (2-5)}$$

and the corresponding S_{eq} value at D_{crit} is called the critical supersaturation (S_{crit})

$$S_{crit} = \left(\frac{4A^3}{27B}\right)^{1/2} \qquad \textbf{Eq. (2-6)}$$

The S_{crit} value of an arbitrary particle will state if the particle can form a cloud droplet under a certain ambient S. The S_{eq} of the droplet will tend to equalize the ambient S to achieve an equilibrium state. If $S < S_{crit}$, there are only two possible equilibrium states in the Köhler curve and the one with lower D is the stable equilibrium state that the droplet will reach. Even though the aerosol particle can

grow to a certain size and form a droplet, if $D < D_{crit}$ it is not considered a cloud droplet. Thus, this particle is not considered a CCN at this S. However, if $S > S_{crit}$ the droplet keeps growing without limit since there is no size at which S_{eq} equals the ambient S (Figure 2-3). Therefore, the particle is considered activated as CCN at S and form a cloud droplet.

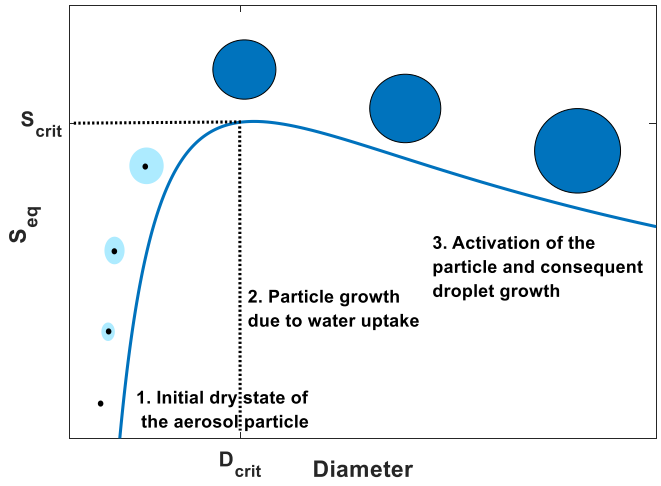

Figure 2-3. Köhler curve showing all stages of particle activation as CCN and the consequent growth as droplet.

Petters and Kreidenweis (2007) introduced a simplification of the classic Köhler theory through the hygroscopicity parameter (κ). This parameter depends on the chemical composition of the aerosol particles that exerts a great influence on the water activity of an aqueous solution:

$$\frac{1}{a_w} = 1 + \kappa \frac{V_s}{V_w} \qquad \textbf{Eq. (2-7)}$$

Where V_s is the volume of the dry aerosol particle and V_w is the volume of the water. If we consider a multi-component solution (i.e., *i* different solutes), which is a more realistic case in ambient aerosol particles, assuming that the solution is in equilibrium the Zdanovskii, Stokes and Robinson (ZSR) rule can be applied (Stokes

and Robinson, 1966). ZSR rule states that the total water volume in the multi-component solution is the sum of the water volume of each individual component. In this way, Eq. (2-7) is transformed into:

$$V_w = \sum_i V_{w_i} = \frac{a_w}{1 - a_w} \sum_i \kappa_i V_{s_i} \qquad \textbf{Eq. (2-8)}$$

where κ_i and V_{s_i} is the hygroscopicity parameter and volume for each solute component. Introducing the total volume of the solution ($V_T = V_w + V_s$) and the volume fraction of each component respect to the total aerosol particle ($\varepsilon_i = V_{s_i}/V_s$), the new expression for a_w is the following:

$$a_w = \frac{V_T - V_s}{V_T - V_s\,(1 - \kappa)} \qquad \textbf{Eq. (2-9)}$$

where κ for the multi-component aerosol particle is now expressed as a volume-weight average of the i components:

$$\kappa = \sum_i \kappa_i \varepsilon_i \qquad \textbf{Eq. (2-10)}$$

Therefore, the hygroscopicity of a multi-component arbitrary particle can be estimated by knowing its internal chemical composition and characterizing the hygroscopicity of each component. The hygroscopicity parameter takes values from 0, non-hygroscopic particles like black carbon particles, to 1.4, for most hygroscopic inorganic salts like sodium chloride (Petters and Kreidenweis, 2007).

Finally, if the new expression of the water activity is introduced in the Köhler equation and assuming that all volumes (droplet and aerosol particle) can be calculated as the sphere volume, this new expression is obtained:

$$S_{eq} = \frac{D^3 - {D_d}^3}{D^3 - {D_d}^3\,(1-\kappa)}\,\exp\left(\frac{4M_w\sigma_w}{RT\rho_w D}\right) \qquad \textbf{Eq. (2-11)}$$

where D_d is the dry diameter of the aerosol particle. Eq. (2-11) describes a curve analogous to that described by Eq. (2-3) and Eq. (2-4), with its corresponding S_{crit} and D_{crit}. Thus, Eq. (2-11) is the mathematical expression of the κ-Köhler theory, which is the main theory describing the ability of an individual aerosol particle to activate as CCN depending on its size and hygroscopicity, which in turn, is related to its chemical composition.

3 Experimental sites and instrumentation

3.1 Experimental sites

The Andalusian Global Observatory of the Atmosphere (AGORA, https://atmosphere.ugr.es/en/about/presentation/agora) provided the instrumentation and experimental observations presented in this thesis. This observatory is situated in southeast Spain, in Granada area, and it consists of two experimental stations representing different atmospheric conditions (urban and high-mountain remote areas). The observatory is managed by the Atmospheric Physics Group (GFAT) of the University of Granada. AGORA is an infrastructure developed for the multi-instrumental study of atmospheric processes, with special focus on (i) atmospheric aerosol and its role in climate and air quality, (ii) aerosol-cloud interaction processes and (iii) trace gases in the lower layers of the atmosphere. Focusing on aerosol-cloud interactions, AGORA represents a suitable infrastructure involving remote sensing and in-situ instrumentation and provides experimental observations at different altitudes from urban conditions, where aerosol particles are freshly emitted, to high-altitude remote sites, where aerosol can activate as cloud droplets.

Granada area climate is considered a Mediterranean-continental climate presenting large seasonal temperature differences (with hot summers and cold winters), with low humidity conditions and high diurnal temperature oscillation. Granada area is situated in a natural basin and is surrounded by mountains with

elevations between 1000 and 3394 m a.s.l. Due to its location, Granada area is affected by the mountain-valley wind regime between Sierra Nevada Mountain range and Granada plateau with up-valley winds during the day and down-valley winds during night. The two major external aerosol sources affecting Granada area are: i) long-range transport of anthropogenic aerosol particles from Europe and ii) natural dust from North Africa, which is located 200 km away from the studied area (Lyamani et al., 2005, 2006; Valenzuela et al., 2012). In addition, the Mediterranean basin is characterized by a complex meteorology that favors the aging of aerosol particles.

Concerning local aerosol sources, road traffic is considered the main local source including traffic exhaust and road re-suspension of material available on the ground (Lyamani et al., 2011; Titos et al., 2014b). Also, domestic heating and biomass burning represent additional local aerosol sources during winter in Granada metropolitan area (Titos et al., 2017). The city of Granada is a medium-size city (with 240.000 inhabitants and around 0.5 million when the whole metropolitan area is accounted) and is considered a non-industrialized area. Despite that, Granada is one of the Spanish cities that suffers pollution problems (Casquero-Vera et al., 2019) due to its orography that favors very weak wind speeds and episodes of high atmospheric stability leading to a large accumulation of particles at the surface. Thus, several heavy pollution episodes occur at Granada area, mainly in winter (Lyamani et al., 2012) and may cause environmental and health problems.

The experimental measurements used in this thesis has been performed in two sampling stations of AGORA. Both stations are separated by a distance of ~ 21 km and the difference in height is approximately 1820 m. A brief description of each station is presented below:

- *UGR station*: it is located at the Andalusian Institute for Earth System Research (IISTA-CEAMA) in the city of Granada (37.16º N, 3.61º W, 680

m a.s.l) and it can be classified as urban background station. The IISTA-CEAMA is situated in the southern part of city and has clear influence of traffic emissions due to its distance (around 500 m away) to the city beltway and one of the main (and busy) streets of the city center.

- *SNS station*: it is a high-altitude remote station located at the Albergue Universitario in the north slope of Sierra Nevada Mountain range (37.10º N, 3.39º W, 2500 m a.s.l). Sierra Nevada presents a wide climatic diversity, with big thermal oscillations due to the complex orography and altitudinal breadth. This site experiences relatively arid conditions and strong insolation due to its west-east orientation. As a high mountain station, SNS shows frequently free tropospheric conditions during nighttime, especially in winter, and the influence of long-range transported aerosol particles. During summer, SNS is influenced by transported particles from Granada area due to atmospheric boundary layer (ABL) growth and mountain-valley breeze phenomenon (De Arruda Moreira et al., 2019). In addition, the high occurrence frequency of NPF events at midday might affect the aerosol population during summer (Casquero-Vera et al., 2020).

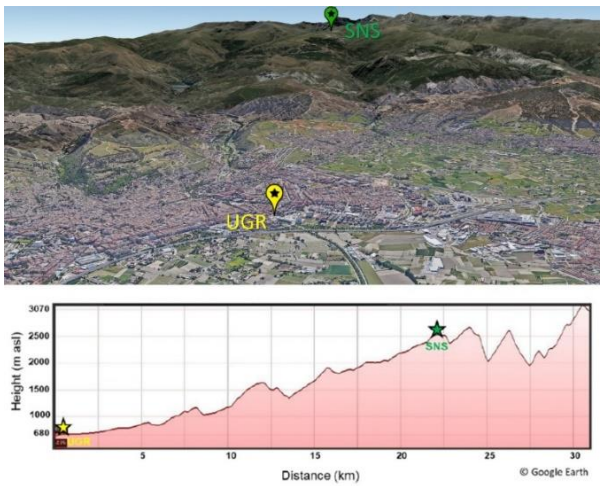

Figure 3-1. Map showing the location of UGR urban site and SNS high-altitude remote site (top panel). The topographic profile between both sites is included (bottom panel).

3.2 Instrumentation and experimental data

All experimental data used in this thesis were sampled at the mentioned stations at ambient conditions and without size cut. The air sampling for all instruments was obtained from the top of a stainless-steel tube, 20 cm diameter and 5 m length at UGR (Lyamani et al., 2008) and 10 cm diameter and 2.5 m length at SNS (Bedoya-Velásquez et al., 2018). Several stainless-steel pipes inside the main tube provided the corresponding air sample flow to the different instruments (Baron and Willeke, 2001). The instruments used in this thesis are described below.

3.2.1 Cloud Condensation Nuclei Counter: CCNc

A Continuous-Flow Stream wise Thermal-Gradient CCN Chamber (CFSTGC) commercialized by *Droplet Measurements Technologies*, DMT, was used for in-situ CCN concentration measurements. This CCN counter (CCNc) was designed by Roberts and Nenes (2005). It generates a constant supersaturation value (SS) along a cylindrical column of about 50 cm length to study the activation of aerosol particles as CCN. To do so, a vertical temperature gradient is established in the column and the inner walls of the column are wetted continuously. The temperature gradient along the axial axis of the column is obtained by three temperature controllers (TECs) situated at different heights of it. The constant SS stablished at the centerline of the column depends on the temperature gradient along the column, the total flow rate (sum of aerosol and sheath flows), and the pressure in the column. Therefore, setting up different temperature gradients allow to explore different SS levels The aerosol sample becomes progressively supersaturated with water vapor as it traverses down the column and those particles that activate as CCN at the specific SS will form water droplets which are counted and sized by an optical particle counter (OPC), equipped with a 660 nm laser, at the bottom of the column

(Figure 3-2). The measured droplet size range that contributes to the CCN concentration is between 0.75-10 µm.

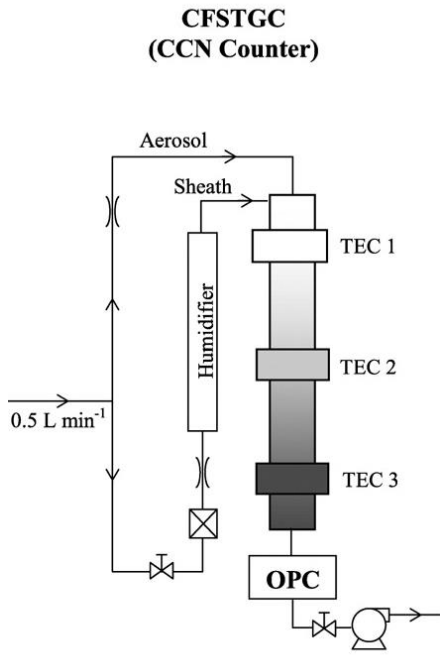

Figure 3-2. Schematic illustration with the main parts of the Cloud Condensation Nuclei counter. (Figure adapted from Lance et al., 2006).

The theoretical basis upon which the instrument creates the supersaturation centerline is the difference between heat and water vapor diffusion. It is known that water vapor diffuses more quickly than heat in air, because water molecular weight is lighter than O_2 and N_2 (main air components) contrasting with heat diffusion which is governed by air molecules collisions. There are two diffusive fluxes that are established from the inner walls of the column to the centerline: the heat flow and the water vapor flow. However, due to the down sampled air flow the same properties of the walls are reached at the centerline in another point of the axial axe (Figure 3-3). These axial distances are defined as x_T, for the heat flux, and x_C, for the water vapor flux. The faster the diffusion process in the radial direction, the

smaller the axial distance. Therefore, $x_C < x_T$ as mentioned above, water vapor diffuses faster than heat. At the wetted walls the water vapor is saturated so water vapor pressure at this point is $P_{H_2O}(R, z) = P^0_{H_2O}(R, z)$, where $P^0_{H_2O}$ denotes the saturation water vapor pressure.

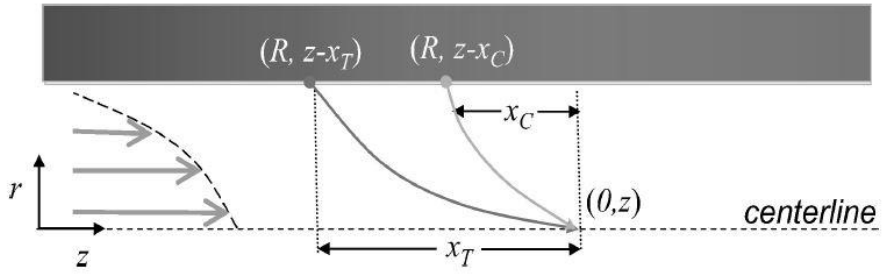

Figure 3-3. Illustration of the how a constant supersaturation is stablished along the centerline of the growth chamber of the CCNc. (Figure taken from Roberts and Nenes, 2005).

The vertical temperature gradient is linear along the column, being the warmest zone the bottom of the column (Figure 3-3). Moreover, the thermodynamics states that $P^0_{H_2O}$ increases with temperature. Computing the saturation ratio at any point of the centerline of the column, $S(0, z)$, as:

$$S(0, z) = \frac{P_{H_2O}(0, z)}{P^0_{H_2O}(T(0, z))} \cong \frac{P^0_{H_2O}(R, z - x_C)}{P^0_{H_2O}(R, z - x_T)} \qquad \textbf{Eq. (3-1)}$$

where it has been considered that the temperature and water vapor pressure at the point (0, z) are the same as the point $(R, z - x_T)$ and $(R, z - x_C)$, respectively. To achieve the last version of Eq. (3-1) we must consider that two points with the same temperature have the same saturated water vapor pressure and remember that water vapor pressure at the wet walls is in fact the saturated water vapor. Finally, we must realize that $S(0, z)$ is greater than 1 (supersaturated condition) because temperature at $(R, z - x_C)$ is higher than $(R, z - x_T)$ due to the vertical temperature gradient. So, this technique allows us to obtain a constant SS value at the centerline of the column.

In the framework of this thesis, both CCNc models (CCNc-100 and CCNc-200) were used to measuring polydisperse CCN concentrations at different SS values. Although the SS set value is fixed in the instrument configuration the actual SS measured value may change due to oscillations in the air sample temperature or pressure or in the signal of the temperature controllers which control the temperature gradient in the column. It is essential for the quality of the data that any CCN concentrations measured at an observed SS value which is more than 20 % (relative) of the nearest SS setpoint should be removed from the analysis (ACTRIS standardized protocol for CCN measurements). To this end, the CCN data have been filtered with the following procedure. In the first step, only data with observed SS above the 1 percentile and below the 99-percentile of the SS set point haven been considered. Then for each SS level we compute the mean value and the standard deviation (STD). Secondly, data above and below 1.5 times the STD are flagged as invalid and are not further used for the analysis presented here, which guarantees that the ACTRIS standard protocol (available in http://actris.nilu.no/Content/SOP) is followed.

Additionally, for an optimum performance of the CCNc the relationship between the SS value inside the columns and its corresponding temperature gradient along the column must be calibrated periodically, especially when the instrument is moved to another sampling site since the mentioned relationship is site-dependent (Rose et al., 2008). To perform the SS calibration, size-selected particles of ammonium sulfate are used to obtain the instrument temperature gradient associated with its corresponding critical supersaturation ratio (SS_{crit}). The monodisperse calibrating flow is generated by nebulization of an ammonium sulfate solution using an aerosol generator system (model TSI 3076). This aerosol flow is passed through a differential mobility analyzer (DMA) to select specific sizes. After this selection, the flow is split into a condensation particle counter (CPC) and CCNc. The temperature gradient that activates 50% of the particles will be linked to the corresponding SS_{crit}. Selecting different sizes for the calibrating particles permit to

obtain the linear relationship between SS and temperature gradient. The second main calibration of the CCNc is the flow rate calibration. Since the flow rate also affects the SS value inside the column, a flow rate calibration is mandatory. Therefore, the aerosol and sheath flows must be calibrated periodically using an external volumetric displacement flow meter. Both CCNc models used in this thesis were calibrated before and after the specific campaigns presented in Chapters from 5 to 7.

3.2.2 Scanning Mobility Particle Sizer: SMPS

The Scanning Mobility Particle Sizer (SMPS) spectrometer is a device used to provide real-time number size distributions of sub-micron aerosol particles. Aerosol particles are classified based on its electrical mobility, which is related to its size. For that purpose, this instrument consists of a DMA, which selects a specific particle size and creates a monodisperse aerosol flow, connected to a CPC, which can measure the number concentration of the corresponding aerosol flow. First, ambient aerosol particles are drawn from the atmosphere and charged through a bipolar charger or neutralizer, which consists either of a radioactive source or X-ray source. Then, the charged aerosol flow passes through the DMA, where aerosol particles are classified according to their electrical mobility. The DMA consists of a pair of concentric cylindrical electrodes and the voltage difference between both electrodes stablishes the fraction of particles that are allowed to pass through the DMA (Figure 3-4). Apart from the voltage, the selected electrical mobility also depends on the DMA's geometry, sheath flow and aerosol flow. Adjusting the voltage and varying it in a cyclical way, the interested electrical mobility values can be scanned continuously. The monodisperse aerosol flow exits the DMA and reaches the CPC, where particles are counted individually with a laser counter using a focusing nozzle. Therefore, the particle number concentration for each specific size is determined. Since the laser counter cannot detect optically particles below 100 nm, the CPC enhance particle size using a butanol condenser. Thus, the butanol vapor

condenses onto the aerosol particles forming droplets of 10 µm in diameter, which are detectable for the laser counter.

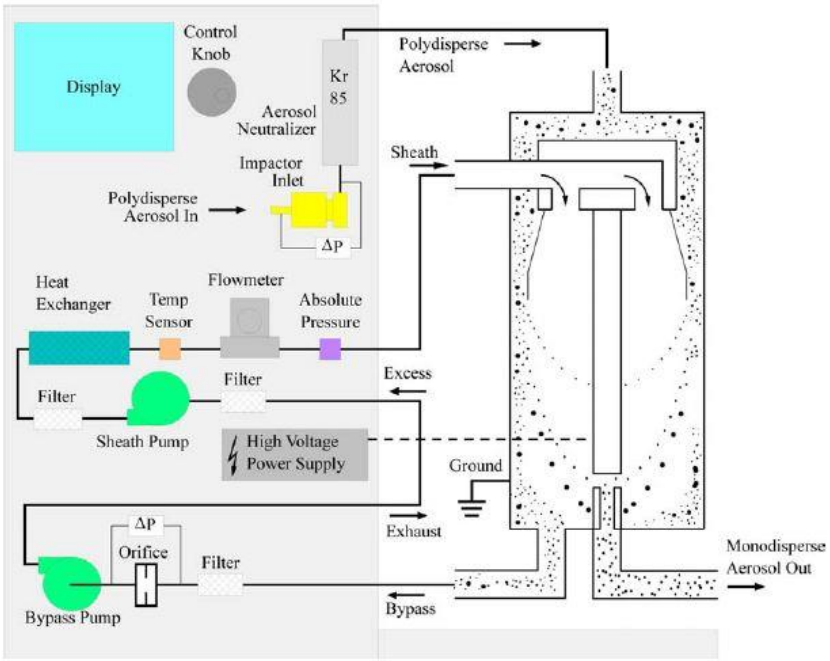

Figure 3-4. Schematic representation of the TSI 3936 Scanning Mobility Particle Sizer. (Figure adapted from TSI manual, 2010).

The diameter range of the aerosol size distribution measurements depends on the combination of the DMA and CPC models. The size selection range of particles is established by the DMA model while the minimum particle size detection, maximum concentration and concentration accuracy depend on the CPC model. Throughout the results of this thesis, the particle number size distribution was measured in the range of 10-500 nm and 4-500 nm with a time resolution of 5 minutes. To cover the first size range a SMPS equipped with a long-DMA (TSI model 3081) and a CPC (TSI models 3772 and 3750) was used, whereas to extend the size range below 10 nm another SMPS system equipped with a nano-DMA (TSI model 3085) and a CPC model 3775 (TSI) was used simultaneously.

SMPS data have been processed using the AIM software (version 10.2.0, TSI, Inc). This software applies two data corrections: i) internal diffusion losses, due to the particle's Brownian movement along the instrument tubing, and ii) multiple charge corrections since the electrical mobility is linked to the particle size and its corresponding charge. Thus, there is a probability that a particle is multiply-charged (Fuchs, 1963) and therefore its electrical mobility will not be proportional to its real size (Wiedensohler, 1988). The quality of the SMPS measurements were checked routinely for flow rates, relative humidity (RH) and 203 nm Poly Styrene Latex particles (PSL) calibration. To guarantee the quality of data, the SMPS systems were intercompared before and after each campaign to ensure comparability between measurements at the different stations. According to Wiedensohler et al. (2018), uncertainty in the measured particle size distribution is within 10% and 20% for the size range 20–200 nm and 200–800 nm, respectively. Also, the SMPS used in this thesis have participated in ACTRIS intercomparisons workshops, which guarantees the quality of SMPS data used in the results.

3.2.3 Time-of-Flight Aerosol Chemical Speciation Monitor: ToF-ACSM

The time-of-flight aerosol chemical speciation monitor, ToF-ACSM, (Fröhlich et al., 2013; Aerodyne Research Inc., Billerica, USA) is an instrument that provides chemically speciated mass concentrations (chemical species considered by the instrument are OA, SO_4^{-2}, NO_3^-, NH_4^+ and Chl^-) and aerosol mass spectra of non-refractory species. This instrument infers the chemical composition using mass spectrometry technique. This method consists of breaking up any compound (in this framework we are referring to aerosol particles) in its forming ions, also called mass fragments. Then the resulting ions are classified according to its mass-to-charge ratio (m/z) and permit to stablish a chemical speciation. This instrument is designed based on the quadrupole aerosol chemical speciation monitor (Q-ACSM, Ng et al., 2011), but with a different mass spectrometry technology that offers higher mass resolving

power, higher time resolution and lower detection limits. The mass spectrometer of the Q-ACSM consists of four rods which establish altering electric fields between them and can classify ions according to its m/z. However, ToF spectrometer identifies the m/z of an ion by measuring the time-of-flight (t) that an accelerated ion takes to cross a vacuum chamber (the so-called ToF-chamber). The variables t and m/z are related for fixed voltages and dimensions of the ToF-chamber as follows:

$$t = k \cdot \sqrt{\frac{m}{z}} \qquad \textbf{Eq. (3-2)}$$

where k is an empirical constant obtained by measuring the time-of-flight of ions with well-known m/z. The procedure to obtain the value of k is the mass calibration. Both ACSM models consist on a simpler device than the Aerosol Mass Spectrometer (AMS, Jayne et al., 2000) and are prepared for long term measurements due to its easier-to-use design. However, ACSM models do not provide size-resolved chemical information and have lower mass spectrometry resolution than the AMS.

The main parts of the ToF-ACSM are presented in Figure 3-5. In the framework of this thesis, the ToF-ACSM operated at a flow rate of 3 lpm and the air sample passed through a nafion dryer, maintaining the incoming relative humidity below 40%. The instrument contains a critical orifice of 100 µm in diameter to constrain the sample flow (under normal pressure conditions) and stablishes a flow rate of 1.8 cm^3/s. A PM_1 standard aerodynamic lens focus the sample flow into a narrow beam and transmits particles between 70 and 700 nm in vacuum aerodynamic diameter (Liu et al., 2007). Then non-refractory particles are flash-vaporized at 600 ºC with a tungsten vaporizer and ionized by electron impact at 70 eV. The instrument is equipped with a capture vaporizer that enhances vaporization and gives a collection efficiency of 1. The ions are introduced into the ToF spectrometer where they are orthogonally extracted and separated according to their m/z. The mass spectra are

obtained for m/z ions ranging from 12 to 200 Th. Finally, the mass loading of the chemical species *s* (γ_s, µg/m^3) is calculated from the measured signals of all mass fragment ($I_{s,j}$ in ions/s) associated to the chemical species *s* using the ionization efficiency (IE_s in ions/pg) as follows:

$$\gamma_s = \frac{1}{Q \cdot IE_s} \sum_j I_{s,j} \qquad \textbf{Eq. (3-3)}$$

where Q is the sample flow rate in cm^3/s. Since the calculation of IE_{NO_3} is the most accurate (Jimenez et al., 2003), all the IE_s are expresses in terms of IE_{NO_3} and the relative ionization efficiency are defined for each species (RIE_s). For organics and chloride, the typical RIE are 1.4 and 1.3, respectively, while for the other chemical species RIE should be calibrated.

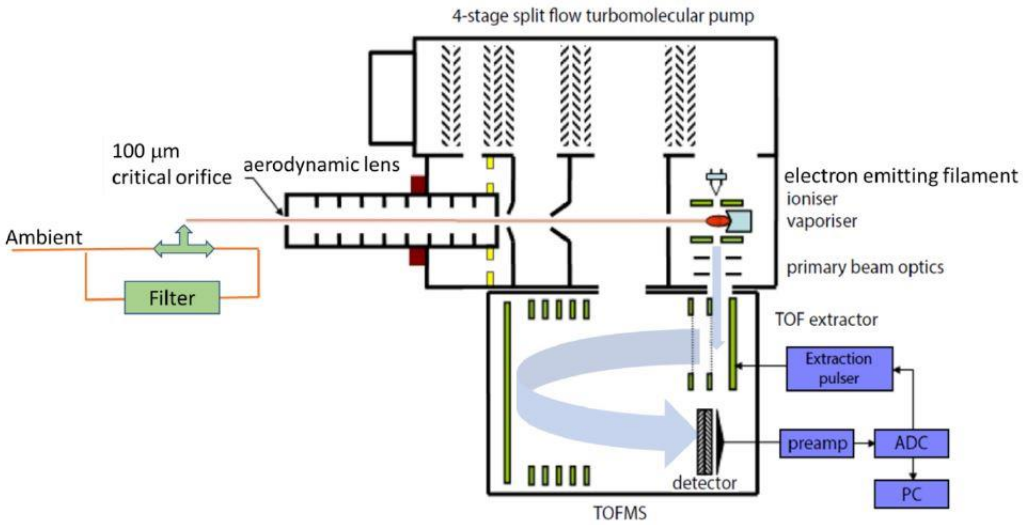

Figure 3-5. Schematic of the main parts of the ToF-ACSM. (Figure taken from Aerodyne TOF-ACSM manual, 2019).

The RIE values for ammonium and sulphate are obtained once the IE_{NO_3} is obtained empirically by comparing mass signal of the ToF-ACSM with its corresponding mass concentration measured with external particle counter. Calibration is performed using dry size-selected 300 nm particles of ammonium

nitrate and ammonium sulfate generated by an aerosol generator atomizer (model TSI 3076) and splitting the flow into the ToF-ACSM and a CPC (in this thesis the model TSI 3772 was used). For more details about the ToF-ACSM calibrations see Fröhlich et al. (2013).

In addition to the RIE calibration, the inlet flow must be calibrated respect to the pressure signal after the critical orifice. To do so, the sample flow rate is measured using an external volumeter displacement flow meter, while the pressure at the inlet is varied using a needle valve. This calibration was performed regularly and before and after intensive field campaigns due to the flow calibration dependence with ambient pressure. In addition to calibrations, ToF-ACSM data must be corrected for changes along the measurement period in the sample flow rate and N_2 signal (related to m/z 28), which is assumed to be constant in the atmosphere. The TOF-ACSM data used for this thesis were processed using the data analysis package "*Tofware*" (version 2.5.13, https://www.tofwerk.com/software/tofware/) running in the Igor Pro 7 environment (Wavemetrics Inc., Oregon, USA).

3.2.4 Additional instrumentation

Aerosol optical properties (aerosol light-scattering and absorption coefficients) were used in this thesis as ancillary measurements for a deepen characterization of aerosol properties. The scattering coefficient of aerosol particles and their spectral dependency can give us information about the amount and predominant size of ambient aerosol particles whereas the absorption coefficient is used to infer the equivalent black carbon (BC) mass concentration, which consists on the mass of BC determined by an optical method (Petzold et al., 2013). From now on BC mass concentration is always referring to equivalent BC mass concentration. Also, the spectral dependency of the absorption coefficient offers some information about the aerosol composition and origin.

The scattering (σ_{sp}) and backscatter (σ_{bsp}) coefficients were measured with an Integrating Nephelometer (model TSI 3563) at three different wavelengths: 450, 550 and 700 nm. This instrument draws air sample from the atmosphere with a flow rate of 15 lpm and the sample (aerosol particles and gases) is illuminated over the angular range from 7º to 170º with a quartz-halogen lamp. Using an opal glass diffuser, the light source can be treated as a Lambertian light source. Then the scattered light by the sample volume inside the main cavity of the instrument is conducted to three photomultipliers which record the scattered signal for each wavelength. It is important to consider that the scattering coefficients are underestimated respect to the real ones since the angular integration of the scattered light is not complete. Thus, Anderson and Ogren (1998) proposed a correction to account for the angular truncation and the deviations of the instrument light source respect to an ideal Lambertian source. From these measurements it is possible to infer intensive optical parameters (such as backscatter fraction or scattering Ångström exponent) that characterize the size of an aerosol population, which were used in the analysis presented in Chapter 5.

Related to aerosol absorption properties, a multiwavelength absorption photometer (the so-called aethalometer model AE 33, Magee Scientific) measured the absorption coefficient (σ_{ap}) at the following 7 wavelengths: 370, 470, 520, 590, 660, 880 and 950 nm. This instrument collects the aerosol particles in a filter drawing ambient air at a flow rate of 4 lpm. Then, it measures the attenuation coefficient for each wavelength through the deposited sample. The absorption coefficient is inferred from the attenuation coefficient considering the interaction of the laser beam with the filter, the scattering with the aerosol sample and the amount of aerosol deposited on the filter. In the framework of this thesis, the aethalometer data was used to infer the BC mass concentration at 880 nm. To do so, the absorption

coefficient must be divided by the mass absorption cross section (MAC) at the corresponding wavelength, which is 7.77 m^2/g for 880 nm (Drinovec et al., 2015).

The Multi-Angle Absorption Photometer (MAAP, Thermo Scientific model 5012) measured the absorption coefficient at 637 nm using filter-based technology as the aethalometer The MAAP draws ambient air with a flow rate of 16 lpm and aerosol particles are deposited on a filter. The 637 nm laser illuminates perpendicularly the sample and the measures the radiation that passes the filter and the back-scattered radiation at two specific angles 130º and 165º (Figure 3-6). Thus, the absorption coefficient at 637 nm is inferred from these measurements using a radiative transfer code which takes into account the scattering effects of the filter, aerosol scattering and multiple scattering involving aerosol sample and filter, being the most reliable filter-based measurement for the aerosol absorption coefficient (for more details of the method see Petzold and Schönlinner, 2004). MAAP data were used to infer the BC using the MAC at 637 nm (6.6 m^2/g, Müller et al., 2011) which was used in the analysis presented in Chapter 5 and 6.

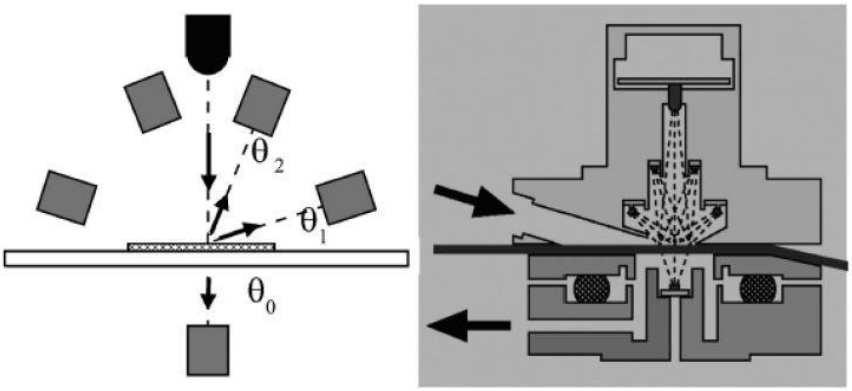

Figure 3-6. Schematic design of the MAAP. Left: location of detecting angles respect to the incident light beam. Right: Illustration of the MAAP optical sensor indicating the inlet and outlet flows. (Figure adapted from Petzold et al., 2005).

4 Methods and data treatment

This chapter explains in detail all methods and data analysis tools used in this thesis to achieve the results presented in the following chapters. The first and second sub-section describes how measurements were used to determine i) each activation parameter that describes the CCN activity of particles and ii) some intensive optical properties, respectively. In the following sub-sections, two methods commonly used in data analysis of complex datasets are explained: Positive Matrix Factorization (PMF) and K-means clustering. The first approach is a dimensionality reduction method which is a very useful tool when previous knowledge of the dataset is available, whereas K-means algorithm consists of an unsupervised machine learning method which can classify data without previous knowledge only based on statistical similarity.

4.1 CCN-derived activation properties of polydisperse particles

In the case of polydisperse measurements of the CCN concentration (N_{CCN}), an effective critical diameter (D_{crit}) for an aerosol population can be defined as the dry diameter above which all aerosol particles are activated. At a certain SS the effective D_{crit} can be derived from PNSD and $N_{CCN}(SS)$ measurements assuming a sharp activation cut-off as follows:

$$N_{CCN}(SS) = \int_{D_{crit}(SS)}^{D_{max}} \frac{dN}{dlogD_p} dlogD_p \qquad \textbf{Eq. (4-1)}$$

where D_p is the particle diameter and D_{max} is the upper limit of the PNSD. In this way, the PNSD is integrated from the D_{max} value to a certain diameter at which the integral value equals the simultaneously measured $N_{CCN}(SS)$. That diameter corresponds to $D_{crit}(SS)$. This method has been widely used in previous studies (e.g., Gong et al., 2020; Jurányi et al., 2011; Paramonov et al., 2015; Schmale et al., 2018) and assumes a perfectly internally mixed aerosol population. Thus, all particles with $D_p > D_{crit}(SS)$ will activate at SS, while particles with $D_p < D_{crit}(SS)$ will remain unactive. Despite the sharp cutoff assumption, it has been observed that this is a reasonable assumption for not freshly emitted particles (Rose et al., 2010; Wang et al., 2010).

The hygroscopicity parameter, as it is explained in Section 2.3, characterizes the hygroscopicity of a specific aerosol particle and is related to its chemical composition. However, an effective hygroscopicity parameter can be defined for the whole aerosol population from PNSD and polydisperse CCN measurements using κ-Köhler theory (e.g., Jurányi et al., 2011; Salma et al., 2021). This effective κ, also known as CCN-derived κ, quantifies the effective hygroscopicity of the activated particles in the CCNc and for that reason shows a dependence with SS. Thus, the effective κ gives information about the hygroscopicity in a certain size range depending on the SS value. In the case of low SS values, for example, κ might provide information about accumulation mode particles. For calculating it, this method uses the effective $D_{crit}(SS)$ as the dry diameter of the Köhler curve. Then, assuming a κ value the maximum of the Köhler curve is obtained (meaning the SS_{crit}). Therefore, the CCN-derived κ will be the κ value that presents a SS_{crit} equal to the SS used in the CCNc. This effective CCN-derived κ will be referred in this thesis as κ.

In the case when CCN measurements are not available, CCN concentrations can be estimated using different methods. In the framework of this thesis, two methods were used to perform CCN estimations presented in Chapters 5 and 7 and are explained in this section. The first method, which is the most accurate and widely used, performs the integration of the PNSD from the critical diameter to its upper limit (e.g., Bougiatioti et al., 2009, 2016; Ervens et al., 2010; Kulkarni et al., 2023; Siegel et al., 2022). The estimation of $D_{crit}(SS)$ is based on κ-Köhler theory from a known κ for the aerosol population (it consists of the inverse process of what it is mentioned in the last paragraph). Despite the simplicity of the method, two important inputs are required: PNSD measurements and knowledge about κ, which in turn requires more information about aerosol particles. For that reason, CCN parameterizations has been developed to estimate CCN from other aerosol parameters. The main parameterization of the $N_{CCN}(SS)$ is the power law derived by Twomey (1959):

$$N_{CCN}(SS) = C \cdot SS^{k} \qquad \textbf{Eq. (4-2)}$$

where C and k are empirical fit parameters. The C parameter can be interpreted as $N_{CCN}(1\%)$ and is related to the amount of aerosol particles in the atmosphere. The k exponent is a dimensionless parameter which gives information of the steepness of the CCN spectra. Thus, k indicates the nature of the aerosol population in terms of its activation properties. Depending on the specific site characteristics, k values range from 0.3 to 1.2 (Hegg et al., 1991). The fit parameters of Eq. (4-2) can be related to other aerosol properties and therefore, a parameterization of $N_{CCN}(SS)$ in terms of other aerosol properties can be useful. Jefferson (2010) established for the first time a parameterization of C and k in terms of intensive optical properties by using linear relation equations. In that study, the backscatter fraction (BSF, ratio between the backscatter and total scattering coefficients) was used to parameterize

C but normalized by the total scattering coefficient to eliminate the dependence of C with the aerosol loading. On the other hand, k was parameterized by the single scattering albedo (SSA, ratio between $\sigma_{sp}/(\sigma_{ap} + \sigma_{sp})$). The SSA provides information about the predominance of scattering or absorbing particles, which in turn is related to the composition of aerosol particles.

In addition to the parameterization using aerosol optical properties, in this thesis another approach is proposed using aerosol parameters controlling the activation properties as CCN. Thus, C was correlated with aerosol number concentration above 80 nm (N_{80}, effective CCN sizes) and k was correlated with D_{geo}, which is directly related to the PNSD of the aerosol population. In this way the $N_{CCN}(SS)$ parameterization is based on particles size which is the main factor controlling CCN activation (Crosbie et al., 2015).

The methodology followed in this thesis to calculate C and k from either the optical or the physical properties consists of first fitting Twomey's law, Eq. (4-2), to each hourly CCNc cycle across all SS to determine the values of C and k. Figure S0-1 shows an example of the CCN spectra at both measurement stations, UGR and SNS, during a SS cycle and the inferred fit parameters according to Twomey's law. This process is repeated for each SS cycle. Then, the inferred values of C and k parameters are related to the corresponding aerosol parameter using linear least squares fit. This allows us to express C and k as linear functions of the corresponding aerosol parameter in the following manner: C = f(Y) and k = g(Z), where f and g are linear equations in terms of aerosol parameters Y and Z, respectively. To build the model, the dataset has been split randomly in two subsets: the first one is used to build the model and the second one to check its performance.

4.2 Estimation of aerosol hygroscopicity from bulk chemical composition measurements

One of the most commonly used approaches to estimate the overall hygroscopicity of the aerosol population from chemical composition measurements (κ_{chem}) is based on the Zdanovskii-Stokes-Robinson (ZSR) approach, as explained in Section 2.3. Using the chemical speciation of non-refractory aerosol particles from ToF-ACSM measurements and the BC mass concentration, the PM_1 bulk chemical composition can be obtained. Therefore, the summation in Eq. (2-10) considers three main terms: OA, IA and BC. Thus, κ_{chem} can be estimated as follows:

$$\kappa_{chem} = \kappa_{OA}\varepsilon_{OA} + \kappa_{IA}\varepsilon_{IA} + \kappa_{BC}\varepsilon_{BC} \quad \textbf{Eq. (4-3)}$$

where $\kappa_{OA}(\varepsilon_{OA})$, $\kappa_{IA}(\varepsilon_{IA})$, and $\kappa_{BC}(\varepsilon_{BC})$, are the hygroscopicity parameters (volume fractions) of organic particles, inorganic particles, and black carbon, respectively. This approximation provides a successful explanation of observations as shown in previous studies (e.g., Bougiatioti et al., 2009, 2016; Rose et al., 2010; Wang et al., 2010). The contribution of IA to κ_{chem} considers some inorganic salts (ammonium nitrate, ammonium sulfate, ammonium bisulfate and sulfuric acid) present in the atmosphere. The volume fractions of the mentioned inorganic salts are obtained by the simplified ion pairing scheme presented by Gysel et al. (2007) using the inorganic species measured by the ToF-ACSM (SO_4^{-2}, NO_3^- and NH_4^+ ions). The Chl^- species was neglected in the κ_{chem} calculation in the framework of this thesis due to their low contribution at SNS (as is showed in Chapter 7), which is very close to the detection limit of the instrument. The density and hygroscopicity parameter for each inorganic salt were taken from previous studies (Kuang et al., 2020b; Wu et al., 2016) and are summarized in Table 4-1. Therefore, the inorganic contribution to κ_{chem} is assumed as a well-defined term in Eq. (4-3). In this thesis, it is assumed that BC particles are completely hydrophobic (κ_{BC}=0) for calculating κ_{chem}, which

is a reasonable assumption as suggested in previous studies (e.g., Deng et al., 2019; Kuang et al., 2020a; Schmale et al., 2018).

Table 4-1. Densities (ρ) and hygroscopicity parameters (κ) used in this study for inorganic species and BC. These values are taken from Wu et al. (2016). The density and hygroscopicity for sulfuric acid are taken from Gysel et al. (2007) and Petters and Kreidenweis (2007), respectively.

Species	NH_4NO_3	$(NH_4)_2SO_4$	$(NH_4)HSO_4$	H_2SO_4	BC
$\rho(g/cm^3)$	1.72	1.77	1.78	1.83	1.70
κ	0.58	0.56	0.48	0.9	0

Unlike inorganic species that exhibit a well characterized hygroscopic behavior, the water uptake capacity of OA species is poorly understood because of the presence of diverse organic species (e.g., Casans et al., 2023; Hallquist et al., 2009; Kanakidou et al., 2005; Rastak et al., 2017), being the definition of κ_{OA} extremely challenging (Kuang et al., 2020a). For that reason, different OA hygroscopicity schemes will be presented in Chapter 7 to estimate κ_{OA} and, in turn, calculate κ_{chem}. As explained in Section 4.1, once the overall aerosol hygroscopicity is calculated, CCN concentrations can be predicted using κ-Köhler theory and PNSD measurements.

4.3 Calculation of intensive aerosol optical properties

Some intensive aerosol optical properties, which provide overall information related to aerosol size and composition, have been inferred from the aerosol optical measurements (σ_{sp}, σ_{bsp} and σ_{ap}) as ancillary aerosol information in the analysis presented in this thesis. Firstly, the BSF was calculated at 450 nm in this thesis as follows:

$$\mathrm{BSF}(450\ \mathrm{nm}) = \frac{\sigma_{bsp}(450\ \mathrm{nm})}{\sigma_{sp}(450\ \mathrm{nm})} \qquad \textbf{Eq. (4-4)}$$

This intensive property acts as a proxy of the predominant particles size in the aerosol population (i.e., higher values of BSF are related to a predominance of smaller particles). Another intensive optical property acting as proxy for the particle size is the scattering Ångström exponent (SAE), which characterizes the wavelength dependence of σ_{sp}. It was calculated according to the following equation for λ_1=550 nm and λ_2=700 nm:

$$SAE_{550-700} = \frac{\log \sigma_{sp}(\lambda_1) - \log \sigma_{sp}(\lambda_1)}{\log \lambda_2 - \log \lambda_1} \quad \textbf{Eq. (4-5)}$$

SAE takes values around 2 when the scattering process is dominated by fine particles, while it is close to 0 when the scattering process is dominated by coarse particles (Seinfeld and Pandis, 1998). BSF and SAE are sensitive to different parts of the aerosol size distribution (Collaud Coen et al., 2007); BSF is more sensitive to particles in the lower part of the accumulation mode while SAE responds to the upper part of the accumulation mode and the coarse mode. Finally, the SSA, which provides information about the predominance of scattering or absorbing particles and can be related to the composition of the particles, was calculated in this thesis at the same wavelength as the σ_{ap} obtained by the MAAP (637 nm). In this sense, σ_{sp} at 637 nm is needed to obtain the SSA and can be calculate using the $SAE_{550-700}$ and $\sigma_{sp}(700\ \text{nm})$ according to Ångström's law as follows:

$$\sigma_{sp}(637\ \text{nm}) = \sigma_{sp}(700\ \text{nm}) \left(\frac{637\ \text{nm}}{700\ \text{nm}}\right)^{-SAE_{550-700}} \quad \textbf{Eq. (4-6)}$$

4.4 Source apportionment: Positive Matrix Factorization (PMF)

Source apportionment studies are widely used in atmospheric science to understand the formation processes and origin of aerosol particles, which can be directly emitted

or formed form gas-phase reactions and quantify its relevance in the atmosphere. In aerosol source apportionment analysis managing mass spectrometry datasets, the experimental data presents high-dimensionality and complexity because mass spectra can be measured with high time (order of seconds to minutes) and mass resolution (hundreds of m/z ions). For that reason, statistical algorithms are needed to ease the interpretation of complex dataset.

The positive matrix factorization (PMF) method (Paatero and Tapper, 1994) is a multivariate factor analysis technique to solve the decomposition of observations matrix (**X**, which will be mass spectral data), where the columns are the variables (m/z ions) and the rows are the observations (instrument timestamps), into two matrices: the factors or sources profiles matrix (**F**) and the contributions matrix (**G**):

$$x_{ij} = \sum_{i,j}^{p} g_{ik} \cdot f_{kj} + e_{ij} \qquad \textbf{Eq. (4-7)}$$

where e_{ij} represent the elements of the residual matrix (**E**), counting for unexplained information of **X** in the p factors solution. In that way, all observations are expressed as a linear combination of the obtained factors, whose contributions vary along the time series. All elements of **G** and **F** matrix are constrained to be positive since the PMF solution must have a physical interpretation. It is because a source cannot have a negative contribution and any mass profile only should have positive values of the m/z. The number of PMF factors, p, is a pre-set parameter that must be stablished. Once the number of factors of the PMF solution is fixed, the algorithm solves Eq. (4-7) iteratively minimizing the **Q** function, which is defined as:

$$Q = \sum_{i,j} \left(\frac{e_{ij}}{\sigma_{ij}} \right)^2 \qquad \textbf{Eq. (4-8)}$$

where σ_{ij} are the measurement uncertainties for the input points. The **Q** function can be considered as the uncertainty-weighted residual of the model. The multilinear engine (ME-2; Paatero, 1999) allows to solve the mathematical problem of calculating the factors by an iteration process from assumed initial values. To achieve environmental meaningful solutions, the ME-2 methodology allows to stablish a priori mass profiles of known sources, the so-called anchor profiles, based on previous scientific knowledge at the experimental site (Canonaco et al., 2013). The strength of this a priori constraint is set by the a-value approach (Brown et al., 2012; Paatero and Hopke, 2009). The a-value establishes how much deviation from the anchor profile the model allows to the solution factor. Thus, a fully constraint factor presents an a-value=0, whereas for unconstraint factors the a-value is not set. The a-value approach is very useful to constrain factors accounting for sources with low contributions to the total signal and might not be identified due to the rotational ambiguity of PMF solutions (Paatero and Hopke, 2009). The rotational ambiguity is an intrinsic property of PMF solutions because different combinations of **G** and **F** can have the same **Q** value. In the framework of this thesis, the ME-2 engine initialization a-value approach and the PMF solution analysis was done using the SoFi v.8 toolkit (Source Finder, Canonaco et al., 2013) for Igor Pro environment.

The majority of PMF analysis using mass spectrometry data are limited to the organic aerosol (OA) mass fraction measured by AMS or ACSM due to its relevance in the atmosphere and its complexity (Jimenez et al., 2009). Thus, understanding the variety of OA sources and formation mechanism can clarify the behavior of ambient aerosol particles and its activation properties as CCN. This methodology will be used in the results presented in Chapter 7.

4.5 Clustering for data classification: K-means clustering

The clustering technique is commonly used in data science to explore unknown structure of data and divide it into different groups with similar properties and therefore reduce data complexity (Ball and Hall, 1965; MacQueen, 1967). The used of multi-dimensional dataset in the context of atmospheric sciences has led to the widespread use of clustering methods (Wilks, 2019). Among all clustering methods, the K-means clustering is the most popular and simplest unsupervised machine learning method that solves clustering problems. K-means separates data into k groups (C_k clusters), minimizing a criterion known as the inertia or within-cluster-sum-of squares:

$$\min_{\{C_k\}} \sum_{i=1}^{k} \sum_{x_j \in C_i} \left\| x_j - \mu_i \right\|^2 \qquad \textbf{Eq. (4-9)}$$

where the inertia, $\left\| x_j - \mu_i \right\|^2$, is the square Euclidean distance between the data point x_j and cluster centroid μ_i, which is defined as the location of the center of the cluster. The total inertia for each cluster is computed as the sum of distances between all data points associated to cluster C_i respect to its corresponding centroid μ_i. Therefore, each data point is allocated to the cluster that presents the minimum distance between this data point and the cluster centroid. The K-means optimization problem is solved using the Lloyd's algorithm (Lloyd, 1982), which is based in two iterating steps: i) assignment of each data point to the closest centroid and ii) update the new centroid positions (Figure 4-1). In this way, reassigning the data to the new closest centroid and updating the centroid position in an iterative process permits to reach the convergence and the K-means problem is solved.

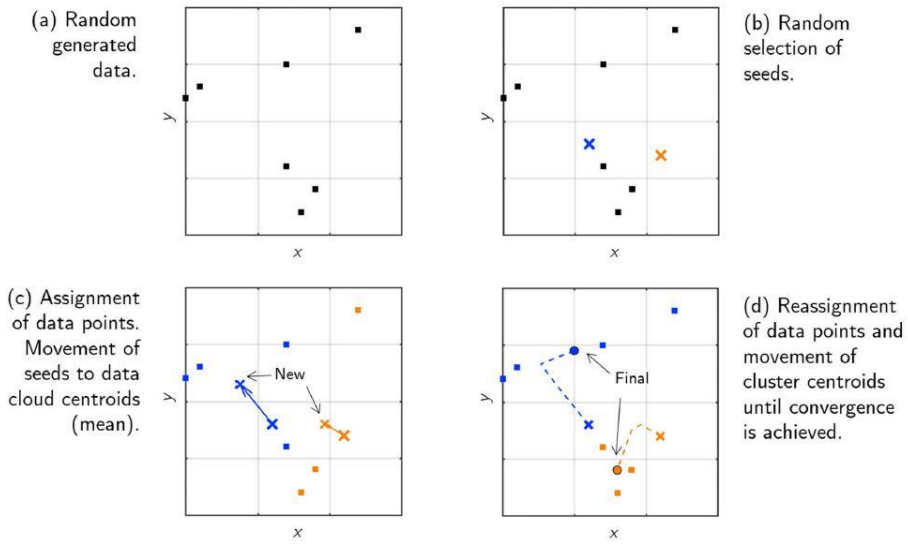

Figure 4-1. Visualization of the different steps of Lloyd's algorithm to perform the K-means clustering. The sample are represented by squares and the centroids by crosses. The final centroids (when convergence is achieved) are represented by dots. (Figure taken from Heikkinen (2020) thesis).

Since the K-means algorithm is an iterative process, the final clustering classification may show some dependence on the initial values of the centroid positions, selection of the seeds. To avoid the initial condition effect on the K-means clustering solution, the clustering should be repeated several times using different seeds (new initial centroid positions). The K-means clustering method requires a-priori specification of the number of clusters to consider in Eq. (4-9) and the solution will depend on it. Thus, the validation of the results obtained by clustering algorithms as well as the optimum number of clusters is a fundamental part of the clustering process. There are several approaches to determine the optimum number of clusters for a dataset and are based on cluster validity indices that quantify the compactness and separation of the clusters, such as Dunn index, Davies-Bouldin or Calinski-Harabasz index (Arbelaitz et al., 2013). The optimal number of clusters can be assumed as the value that optimizes the validity index. In the framework of this thesis, the Davies-Bouldin (DB) index was used to estimate the optimum number of clusters. The DB criterion is based on a ratio of within-cluster and inter-cluster

distances with the optimal clustering solution having the smallest DB index value (Davies and Bouldin, 1979).

The clustering methodology has been used in many previous studies to classify PNSD data being a reliable and powerful tool to identify aerosol population categories for multiple sites (e.g., Atwood et al., 2019; Beddows et al., 2009; Brines et al., 2014; Lee et al., 2021). In particular, the K-means clustering algorithm was proved to be one of the best techniques for analyzing PNSD datasets with characterization and source apportionment purposes (Gong et al., 2022; Salimi et al., 2014; Varanda Rizzo et al., 2018). In Chapter 6, a PNSD classification will be performed using *K*-means methodology to identify the main aerosol populations.

5 Activation properties of aerosol particles as cloud condensation nuclei at urban and high-altitude remote sites in southern Europe

This chapter is adapted from "***Activation properties of aerosol particles as cloud condensation nuclei at urban and high-altitude remote sites in southern Europe***" by F. Rejano, G. Titos, J.A. Casquero-Vera, H. Lyamani, E. Andrews, P. Sheridan, A. Cazorla, S. Castillo, L. Alados-Arboledas and F.J. Olmo. Published in *Science of The Total Environment*, Volume 762, 143100, 2021.

In this chapter, the CCN activation properties are characterized at UGR (urban) and SNS (high-altitude remote) stations for specific campaigns. The measurement campaign at UGR was from October 2018 to May 2019, while at SNS station the measurement campaign covers the summer season (from June to August of 2019). First, a general characterization of CCN concentrations and activation properties together with other aerosol properties at both environments is provided. Then, the diurnal variability of CCN properties at both sites are analyzed to identify the sources and processes affecting CCN properties at these two different environments. Due to the high frequency of NPF events previously observed at SNS station and the expected large contribution of this process to CCN concentrations (Casquero-Vera et al., 2020), we then analyze the contribution of NPF to CCN concentrations.

Finally, we explore two empirical models for predicting CCN concentrations from other aerosol measurements.

5.1 Characterization of aerosol and CCN properties

The main aerosol properties observed at UGR (urban site) and SNS (high-altitude site) stations are summarized in Table 5-1 and Figure 5-1. The statistics shown in Table 5-1 are based on all data available at each site while, in Figure 5-1, data are split into seasons. The mean and median values of aerosol concentration at UGR over the whole study period was around $1.2 \cdot 10^4$ cm^{-3} and 9400 cm^{-3}, respectively, which are typical values for polluted urban environments (Che et al., 2016). N_{CN} at UGR was significantly higher in winter than in spring and summer, likely due to additional anthropogenic aerosol sources such as domestic heating and predominance of weak winds and lower atmospheric boundary layer heights (Lyamani et al., 2012).

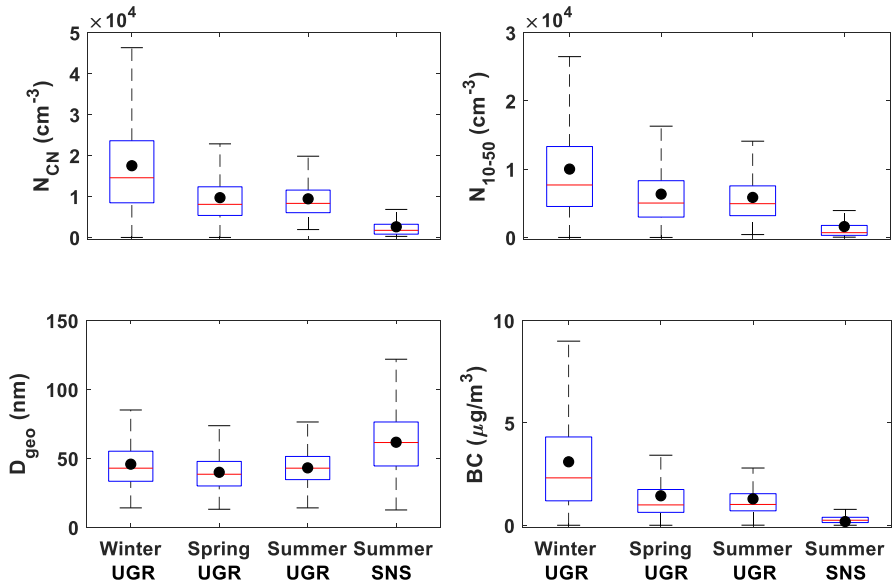

Figure 5-1 Seasonal variation of total aerosol concentration (N_{CN}), aerosol number concentration between 10-50 nm ($N_{10\text{-}50}$), geometric diameter (D_{geo}) and BC mass concentration at UGR and summer data at SNS. Mean values (black dots), median values (red lines), 25th-75th percentiles (blue boxes) and maximum-minimum values (whiskers) are presented.

As expected, during the summer, SNS exhibits a much lower particle concentration than UGR (mean value of 2600 cm^{-3} at SNS compared with a mean value of 9400 cm^{-3} at UGR). The aerosol concentration at SNS is higher compared to other European mountain stations like Schneefernerhaus station at Zugspitze (2650 m a.s.l. in German Alps) with a median value of 1000 cm^{-3} in the diameter range from 10 to 600 nm for the period 2004–2007 (Birmili et al., 2009), or Jungfraujoch (3580 m a.s.l. in central Swiss Alps) with annual median CN concentrations of 320 cm^{-3} in the diameter range from 16 to 570 nm (around 600 cm^{-3} during summer) (Jurányi et al., 2011). However, at a lower-altitude mountain site (Puy de Dôme, France, 1465 m a.s.l), particle concentration ranged from 3200 to 4000 cm^{-3} during summer in the diameter range from 10 to 500 nm (Venzac et al., 2009). The observed particle concentration at mountain sites is highly influenced by the altitude of the sampling site and the season. Our analysis at SNS only covers the summer season, which is the period when the aerosol concentration achieves its maximum due to the high NPF event frequency and the transport of pollutants from Granada city to Sierra Nevada station because of mixing layer growth and mountain-valley breeze transport (Casquero-Vera et al., 2020). The concentration of particles in the diameter range of 10–50 nm ($N_{10–50}$, nucleation and fresh Aitken mode particles), which are difficult to activate at low SS, represent more than 50% of total aerosol concentration at both sites during both experimental campaigns (Table 5-1).

There are also differences in the calculated intensive optical properties at the two sites, indicating the presence of different aerosol types at both sites (Table 5-1). The aerosol population is dominated by scattering particles at SNS, with SSA value close to 1, while at UGR the mean SSA of 0.7 reveals the strong contribution of absorbing particles. High SAE values at UGR indicate a large predominance of small particles in the urban area while the relatively low SAE values observed at SNS indicate an increased contribution of large particles to the total aerosol population over this remote station. This difference in SAE values between stations

is partly due to the different measurement period at both sites (winter-spring at UGR and summer at SNS). The relatively low summer SAE values at SNS are associated with the increased frequency of Saharan dust intrusions over the study (Valenzuela et al., 2012). BSF values at UGR (mean value of 0.16) are slightly higher than at SNS (0.14), also indicating the presence of larger particles at SNS that backscatter radiation less effectively than small particles. Using the geometric diameter, the diameter below which half of the total aerosol concentration is found (D_{geo}), as a proxy for aerosol size distribution, Figure 5-1 suggests that SNS is characterized during summer by the presence of larger particles (mean D_{geo} of 62 nm) than those present at UGR during (mean D_{geo} remains below 50 nm in all seasons). D_{geo} at SNS also exhibits high variability which suggests changes in aerosol sources and strength. This is consistent with the SAE values in Table 5-1 and can be explained by the higher influence of small freshly emitted particles at UGR compared to SNS and the seasonal impact of dust at SNS.

The BC concentrations observed at the two sites are very different, with BC at SNS station approximately an order of magnitude lower than at the urban UGR station (Table 5-1and Figure 5-1). BC is considered a good tracer of road traffic emissions (Lyamani et al., 2011; Reche et al., 2011). The high BC mass concentrations at UGR are mainly linked to the significant impact of local anthropogenic emissions, primarily from road traffic (Lyamani et al., 2011). BC mass concentrations at UGR are in the range of those observed at other European urban sites (Reche et al., 2011), showing higher BC concentrations and variability during winter compared to spring and summer. In contrast, the low BC concentration at SNS reflects the low influence of anthropogenic emissions at this remote site. SNS station exhibits slightly higher BC concentrations than other European mountain stations probably due to the larger influence of anthropogenic pollutants transported from Granada city to SNS station. The BC values at SNS are slightly lower than those obtained at La Parva (2800 m a.s.l) in the Andes Mountain range

during the summer of 2015 where BC mass concentration reached values between 0.3 and 0.5 μg/m3 (Gramsch et al., 2020). Even higher BC concentrations have been observed at similar high-altitude stations in the Himalayan Mountain range, such as Astore (2600 m a.s.l) and Skardu (2680 m a.s.l) stations where BC concentrations were around 1.5 μg/m3 during August of 2017 and 2.0 μg/m3 during September of 2017, respectively (Zeb et al., 2020). The high BC concentrations reported in the Himalayan study are due to the higher influence of anthropogenic activities compared to those affecting SNS. The study of Ripoll et al. (2015) carried out at Montsec (1570 m a.s.l.) in the pre-Pyrenees in eastern Spain showed that the mean BC value was 0.2 μg/m3 during summer 2011, which is more similar to the BC concentration measured at SNS.

Table 5-1. Mean values (± STD), median values (μ_{50}) and percentile 25th (μ_{25}) and 75th (μ_{75}) of the total aerosol concentration (N_{CN}), aerosol concentration between 10-50 nm ($N_{10\text{-}50}$), D_{geo}, BSF, SSA, SAE and BC mass concentration along the whole measurement period of each instrument. For UGR values in parentheses refer to coincident measurements with the CCNC (from Oct 2018 to May 2019).

Site	UGR				SNS			
Variable	Mean ± std	μ_{50}	μ_{25}	μ_{75}	Mean ± std	μ_{50}	μ_{25}	μ_{75}
$N_{CN}(\cdot 10^3 cm^{-3})$	12±9	9.4	6.1	15	2.6±2.7	1.7	0.8	3.2
	(13.5±10)	(10)	(6.3)	(17.5)				
$N_{10-50}(\cdot 10^3 cm^{-3})$	7±6	5.4	3.1	8.9	1.6±2.2	0.7	0.3	0.18
	(8.1±7)	(6.2)	(3.6)	(10)				
D_{geo} (nm)	43±14	41	32	51	62±23	61	45	0.76
	(43±15)	(40)	(32)	(51)				
BSF(450 nm)	0.16±0.06	0.15	0.13	0.16	0.14±0.07	0.13	0.12	0.15
SSA(637 nm)	0.70±0.10	0.72	0.62	0.79	0.92±0.04	0.93	0.90	0.95
$SAE_{550-700}$	2.1±0.8	2.2	1.8	2.4	1.5±0.6	1.6	1.0	1.9
BC($\mu g/m^3$)	2.0±2.0	1.3	0.7	2.5	0.2±0.1	0.2	0.1	0.3
	(2.3±2.4)	(1.4)	(0.8)	(2.9)				

The CCN-related parameters at the two sites also exhibit significant differences. Figure 5-2 shows the results for both stations in terms of CCN concentration (N_{CCN}), activation fraction (AF), critical diameter (D_{crit}) and hygroscopicity parameter (κ). CCN concentration was much higher at UGR than at SNS. Mean values of N_{CCN} at SS=0.5% for SNS and UGR were 820 ± 600 cm^{-3} and 2500 ± 2000 cm^{-3}, respectively. UGR exhibited a higher variability in N_{CCN} (wider interquartile range) than at SNS due to the large variability of the source emissions (mainly of anthropogenic origin) affecting UGR (Figure 5-2). CN and CCN concentrations at UGR show their maximum values during winter (mean winter values of N_{CN} ~$2 \cdot 10^4$ cm^{-3} and N_{CCN} ~ 5000 cm^{-3}) compared to spring (mean spring values of N_{CN} ~ 10^4 cm^{-3} and N_{CCN} ~ 1600 cm^{-3}) due to additional emission sources (as domestic heating) and formation of thermal winter inversions that contribute to high aerosol concentrations close to the surface during winter (Lyamani et al., 2012). During wintertime, N_{CCN} concentrations at UGR are higher than those observed in Paris (2248 cm^{-3} at SS = 0.5%; Jurányi et al. 2013) and similar to those values observed in big cities such as Beijing during fresh pollution conditions (4982 cm^{-3} at SS=0.46%; Gunthe et al., 2011) or Seoul (5323 cm^{-3} at SS=0.6%; Kim et al., 2014). CCN concentrations at SNS are also higher than those observed at a comparable mountain site like Jungfraujoch (313 cm^{-3} at SS=0.47%; Jurányi et al., 2011).

The mean critical diameters, D_{crit} (SS=0.5%), obtained at UGR and SNS for the whole period were 91 and 66 nm, respectively. At a constant SS, a smaller D_{crit} is expected for more hygroscopic particles. Therefore, the larger D_{geo} and smaller D_{crit} (SS=0.5%) observed at SNS compared to UGR suggest that the aerosol particles at SNS are more hygroscopic and thus can be activated more easily than those at UGR. Also, the activation fraction (AF) at a specified SS relates the particles that have been activated to the total amount of particles. Low values of AF at SS=0.5% (Figure

5-2) were observed at UGR, with an interquartile range of 0.13 to 0.28 and a median value of 0.20. Higher values were obtained at SNS, with an interquartile range of 0.29 to 0.62 and a median value of 0.47. The high D_{crit} and the high fraction of non-hygroscopic particles (low value of SSA) at UGR may explain the low AF values observed at this site.

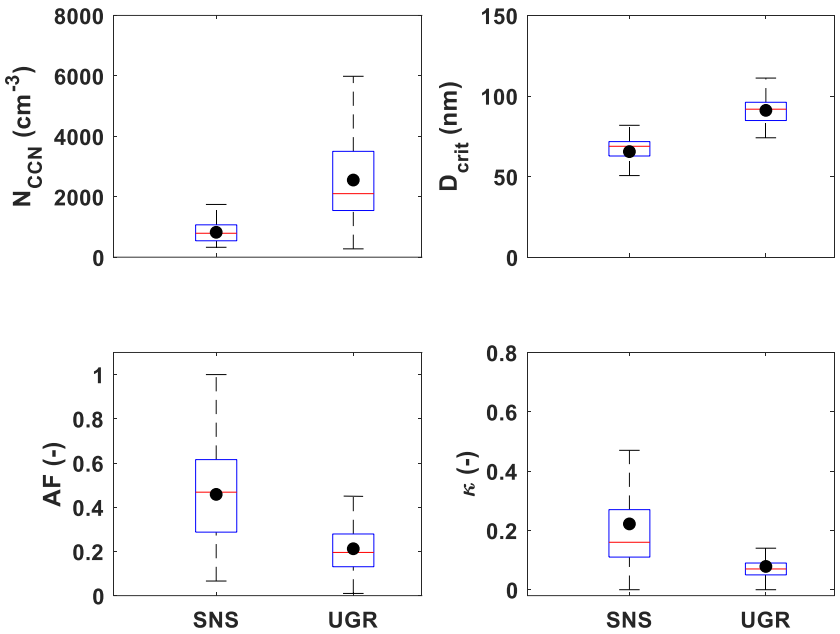

Figure 5-2. Mean values (black dots), median values (red lines), 25th-75th percentiles (blue boxes) and maximum-minimum values (whiskers) of CCN concentration (N_{CCN}), Activation fraction (AF), D_{crit} and κ at UGR and SNS for all data. All measurements and inferred parameters are obtained at SS=0.5%.

At UGR, characterized by low AF (values extending below 0.1), the BC concentrations were high (maximum values were close to 9 μg/m^3), whereas at SNS the opposite relationship occurs (i.e., low BC concentrations and higher AF were observed). This is consistent with fresh emitted BC being associated with small and non-hygroscopic particles. In addition, the AF shows much more variability (wider interquartile range) at SNS, despite the narrow interquartile range of N_{CCN}. This

might be due to the significant changes in aerosol size distribution during the study period at SNS, as evidenced by D_{geo} variability (Figure 5-1). Casquero-Vera et al. (2020) found that NPF events are very frequent at SNS during summertime, which enhances the total number concentration of particles and shifts the size distribution towards smaller sizes. This phenomenon together with the aerosol transport from Granada city to SNS can contribute to the large variability observed in AF at SNS.

Inferring the hygroscopicity parameter κ from CCN and size distribution measurements (see Section 4.1) allows us to quantify the overall hygroscopicity of activated particles, which provides qualitative information on the bulk aerosol composition. The estimated mean value of κ at SS=0.5% was 0.08±0.03 at UGR (ranging from 0.05 to 0.09), and 0.22±0.09 at SNS (ranging from 0.11 to 0.27). This result is consistent with the D_{crit} behavior described previously which suggested lower hygroscopicity at the urban site compared to the high-alpine site. The higher variability of κ observed at SNS compared to UGR (see Figure 5-2) may be explained by the higher variability in aerosol properties at SNS which is affected by (i) airmasses from different origins, (ii) NPF events that significantly affect the size distribution and (iii) the influence of atmospheric boundary layer (ABL) dynamics that transport pollutants from the Granada area to Sierra Nevada. In contrast, aerosol particles at UGR are strongly dominated by local sources, especially road traffic, leading to an overall non-hygroscopic aerosol. Relatively lower mean values of κ are observed at UGR in winter season (κ=0.06±0.01) compared to spring (κ=0.09±0.02) (not shown here). Previous studies at UGR have shown the low hygroscopicity of aerosol particles at this site due to the predominance of absorbing particles composed of species such as BC and organic matter, especially during winter (Burgos et al., 2019; Titos et al., 2014b). The mean κ parameter at SNS is higher than at UGR but it is below 0.3, which is the typical value associated with continental background aerosol (Andreae and Rosenfeld, 2008), suggesting there is an impact of anthropogenic aerosol at SNS as well.

Table S0-1 shows a comparison of N_{CCN}, AF, D_{crit} and κ values from the literature and those obtained in this study for SNS and UGR. Compared with the studies listed in Table S0-1, among the urban sites, UGR is characterized by the lowest κ parameter and one of the highest D_{crit} values, demonstrating the hydrophobic nature of aerosol particles at UGR during winter and spring seasons, and consequently low activation capacity. Results obtained at SNS are consistent with those values reported at Jungfraujoch (3580 m a.s.l.) and Puy De Dôme (1465 m a.s.l.) during summer (Table S0-1), with very similar AF, D_{crit} and hygroscopicity parameter values.

5.2 Diurnal evolution patterns

In the previous section, overall differences in activation properties in relation to other aerosol properties between the two sites were discussed. Here we evaluate the impact of temporal patterns, specifically the diurnal cycle of CCN. Analyzing the diurnal evolution of the activation properties of aerosol particles can be useful for understanding the sources and transformation processes at the urban and high-mountain sites. Figure 5-3 shows the diurnal evolution of aerosol size distribution, N_{CCN}, N_{CN}, BC, AF, SSA, D_{crit} and D_{geo} at both stations. Note that the scales in Figure 5-3 are different for UGR and SNS to allow better visualization of the diurnal patterns and N_{CCN} and N_{CN} are both referred to the left Y axis in Figure 5-3c and Figure 5-3d for a better comparison. BC has been used here as tracer of road traffic emissions and SSA as an estimation of the relative contribution of absorbing particles (mainly BC) to the total aerosol load.

The mean diurnal evolution of the aerosol size distribution at both sites is shown in Figure 5-3a and Figure 5-3b. The aerosol concentration at UGR is dominated by particles below 100 nm during the whole day. Between 06:00 and 09:00 UTC and 18:00 and 21:00 UTC, during the traffic rush hours, the particles

concentration increased noticeably in all sizes, but especially in the diameter range from 10 to 50 nm. At SNS, we can observe a completely different behavior of the aerosol size distribution. Before 12:00 UTC, at SNS particles are mainly confined in the size range 20–200 nm and are characterized by low number concentration. At around 12:00 UTC a clear mode of particles between 10 and 50 nm appears. From 12:00 UTC and onwards, this mode grows to larger sizes and then decreases in intensity throughout the rest of the day. This pattern suggests that NPF events occurring at midday influence the aerosol size distribution at SNS.

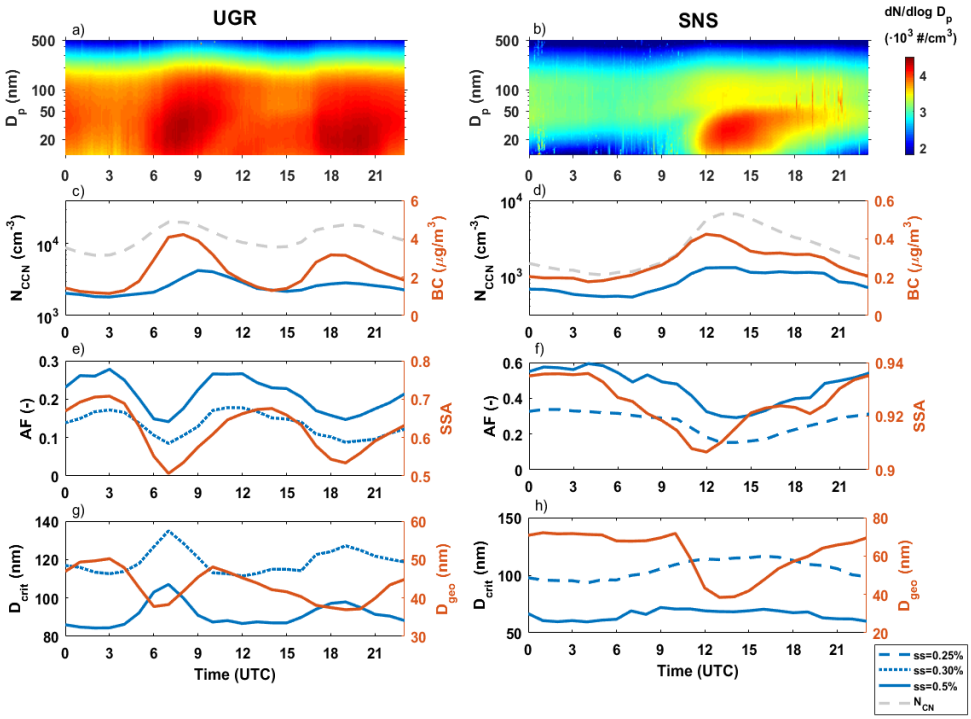

Figure 5-3 Diurnal patterns of aerosol size distribution, N_{CCN}, N_{CN}, AF, SSA at 637 nm, D_{crit} and D_{geo} obtained at UGR station (left panels) and SNS station (right panels). N_{CCN} and N_{CN} are both referred to the Y axis on the left in panels c) and d).

As can be seen in Figure 5-3c, the BC diurnal pattern is characterized by two maxima at UGR during traffic rush hours while, at SNS, BC is characterized by a maximum at midday associated with the upslope transport of pollutants from Granada area to SNS (Figure 5-3d). At both sites, N_{CN} and N_{CCN} exhibit similar

patterns to BC. At UGR, the diurnal evolution of N_{CN} shows two maxima during the day coinciding with traffic rush hours. The peak values were (2.0±1.3) $\cdot 10^4$ and (1.8±0.9) $\cdot 10^4$ cm^{-3} at 7:00 and 19:00 UTC. N_{CCN} also exhibits two maxima with peaks values of 4200±3000 and 2800±2000 cm^{-3} but at different time: 9:00 and 19:00 UTC. The delay observed between the morning peaks of N_{CCN} and N_{CN} might be caused by the fact that particles emitted by road traffic with diameter below the D_{crit} are able to grow to larger diameters above D_{crit} in the following hours (particles reach around 90 nm at 10:00 UTC), and act as CCN. Also, oxidation of emitted particles can affect the aerosol hygroscopicity leading to higher N_{CCN}. This is supported by the observed increase in κ (Figure 5-4) in coincidence with N_{CCN} after traffic rush hours. The combination of both processes could explain the delay observed between the morning peaks of N_{CCN} and N_{CN}. The lack of such a time delay between the evening peaks of N_{CCN} and N_{CN} may be due to differences in the observed aerosol properties for the morning and evening periods.

Because of the diurnal evolution of N_{CN} and N_{CCN}, AF at UGR shows two minima during the day at 7:00 and 19:00 UTC. SSA diurnal evolution also shows two minima that coincide with the AF minima, denoting an increase in the contribution of absorbing particles (mostly hydrophobic particles) that are not activated. It is interesting to note that the AF diurnal range (difference between the maximum and minimum values) increases with SS. This behavior is likely due to the fact that outside of traffic rush hours, higher SS values result in higher CCN concentration; however, during traffic rush hours the same SS increase in the instrument rarely increases CCN concentration due to the high concentration of UFP and BC particles, which are extremely difficult to activate even at high SS. D_{geo} values at UGR also exhibit a diurnal pattern with two minima at traffic rush hours, with values below 40 nm. In urban environments, road traffic emissions are the main source of UFP. These two D_{geo} minima, then, are likely attributed to newly formed particles due to emission of precursor gases by road traffic. Conversely, the D_{crit}

diurnal pattern shows two maxima for all SS values that coincide with the D_{geo} minima during traffic rush hours. The D_{crit} peaks during traffic rush hours are related to the emission of aerosol particles with a more hydrophobic chemical composition (such as BC). Even if the diameter of these recently emitted particles is above the D_{crit}, these particles are unable to activate due to their chemical composition and hygroscopicity properties causing an increase in the D_{crit}.

At SNS, the diurnal behavior is completely different (Figure 5-3). N_{CN} and N_{CCN} at SS=0.5% exhibit a maximum between 13:00 and 14:00 UTC with mean values around 6500±4000 cm^{-3} and 1300±800 cm^{-3}, respectively. The BC diurnal pattern, used as a proxy of anthropogenic pollution at SNS, has its maximum earlier, at 12:00 UTC. This increase in BC at midday is associated with the diurnal evolution of the ABL and upslope transport of pollutants from the valley to the high mountain station. As Moreira et al. (2020) showed using microwave radiometer and ceilometer measurements, the ABL height in Granada starts increasing in the morning and achieves its maximum at midday, reaching the SNS station height at midday during the summer. In addition to the increase in height of the ABL over Granada, the westerly winds that predominate during the day at SNS favor the transport of pollutants from the valley to the mountain (Casquero-Vera et al., 2020). N_{CN}, N_{CCN} and BC start increasing at around 8:00 UTC, but as mentioned before, the maximum is achieved later for N_{CN} and N_{CCN} than for BC. This timing difference between BC and N_{CN} suggests an additional source of N_{CN} other than transport from Granada to Sierra Nevada. Unlike at UGR, at SNS the AF and SSA do not follow the same diurnal pattern. The SSA minimum occurs earlier (at 12:00 UTC) than the AF minimum (14:00 UTC). Therefore, the increase in the relative contribution of absorbing particles might not be the main factor controlling N_{CCN} and AF at SNS. The D_{geo} diurnal pattern shows a sharp decrease at midday (between 12:00 and 14:00 UTC) which is associated with the high frequency of NPF events that occur at midday during summer (Casquero-Vera et al., 2020). Although the transport of anthropogenic particles from

Granada area also may affect D_{geo}, the sharp D_{geo} decrease observed and the shorter duration of this decrease (as compared with the BC increase) suggests that NPF events might be the main source of particles at SNS at midday.

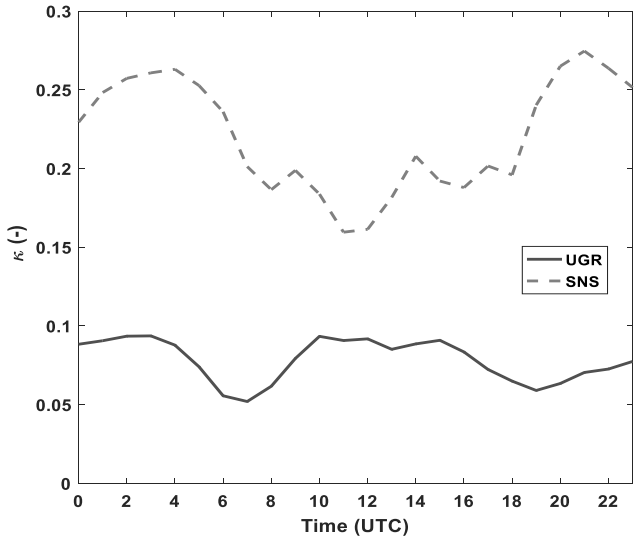

Figure 5-4. Diurnal pattern of hygroscopicity parameter (κ) at UGR and SNS at SS=0.5%.

D_{crit} does not show a clear diurnal pattern at SNS, except at SS =0.25%, the lowest SS studied. At this SS, there is a wide increase from 08:00 UTC and onwards, with a maximum around 14:00 UTC. This increase in D_{crit} may be associated with the lower hygroscopicity of the predominant particles at this time of the day, which are a combination of particles transported upslope from the Granada urban area and newly formed particles after growth (Casquero-Vera et al., 2020). The different behavior of D_{crit} with different SS values is interesting. At higher SS, D_{crit} is roughly constant throughout the day, in contrast to the behavior of D_{crit} at lower SS. At lower SS, there are particles which are less hygroscopic that do not activate while those particles are able to activate at higher SS. At midday, the transport of particles could lead to overall lower aerosol hygroscopicity as shown in Figure 5-4. Also note the increase in BC mass concentration and decrease in SSA at midday.

Figure 5-4 shows the diurnal cycle of the hygroscopicity parameter κ. The hygroscopicity parameter is a proxy for the size and chemical composition of the whole population of activated particles. At UGR, κ shows two diurnal minima associated with road traffic emissions (Figure 5-4). During traffic rush hours, κ decreases due to the increase of non-hygroscopic particles and UFP concentration (mainly nucleation and fresh Aitken mode particles). There is a decreasing trend of κ as SS increases (not shown). This is because the less hygroscopic particles are activated when SS increases; κ approaches 0.05 during traffic rush hours. At SNS, during the first and last hours of the day, κ has values around 0.25. At 10:00 UTC, κ starts to decrease coincident with the increase observed in BC concentration and the decrease in D_{geo}. κ achieves its minimum at 12:00 UTC with a value of 0.16 (Figure 5-4). This is consistent with changes in aerosol chemical composition and size due to NPF and the transport of particles from Granada city to Sierra Nevada leading to a reduction of κ value.

These results suggest that the two main aerosol sources influencing activation properties of aerosol particles at SNS during summer are newly formed particles due to nucleation events and the transport of pollutants from Granada. As these two processes seem to occur simultaneously around midday, our observations reflect the joint effect of both processes. To understand the behavior of activation properties during NPF events, in the following section we analyze the contribution of NPF to CCN in Sierra Nevada.

5.3 Contribution of NPF to CCN in Sierra Nevada

To perform this analysis, we classified by visual interpretation the number aerosol size distributions measured at SNS as NPF events, non-events, undefined and bad-data days following the procedure proposed by Dal Maso et al. (2005). During the

measurement campaign at SNS 67 NPF events, 16 undefined events and 13 non-events days were observed. However, not all NPF events showed the typical "banana shape" associated with particle growth. Following Rose et al. (2017) criteria, only those NPF events referred as type I, i.e. with clear particle growth from smallest sizes, were selected to investigate the contribution of NPF events on CCN concentrations. Type II events are more irregular and may be interrupted in certain size ranges (Rose et al., 2017), and in bump type events the growth of newly formed particles is not observed (Hirsikko et al., 2007; Yli-Juuti et al., 2009). Therefore, we focused our analysis on type I events and selected the 15 clearest NPF events. Mean diurnal evolution of the aerosol size distribution is shown in Figure S0-2 for event and non-event days. During event days we can observe a clear growth of particles from the lowest diameter (10 nm), which appear around 12:00 UTC, to larger diameters (around 70 nm) during the rest of the day until 21:00 UTC. During non-event days the aerosol size distribution is characterized by particles in the range 20–200 nm and after 12:00 UTC the particle concentration increases in the diameter range between 20 and 80 nm which is related to the vertical transport of particles from the urban area.

Figure 5-5 shows the comparison of the diurnal evolution of N_{CCN}, N_{CN}, AF, D_{crit} and D_{geo} at SNS during NPF event (solid line) and non-event (dash line) days. There is a clear difference in all variables investigated between event and non-event days. This difference is large during the daytime hours while during the evening there is no difference between NPF and non-event days. As expected, N_{10-20} and N_{20-50} are the variables most affected by NPF events. Changes in their diurnal patterns are noticeable starting at 10:00 UTC, when the nucleation process tends to initiate. N_{10-20} and N_{20-50} maximum concentrations during NPF events are approximately 8 times higher than the corresponding values during non-event days. N_{10-20} reaches its maximum at around 12:00 UTC while N_{20-50} reaches it 2 h later, due to particle growth. N_{50-100} is also affected by NPF - it does not show a sharp increase as is seen

for $N_{10\text{-}20}$ and $N_{20\text{-}50}$; rather it shows a constant gradual increase during the morning and afternoon until $N_{50\text{-}100}$ reaches its maximum value at 15:00 UTC. $N_{50\text{-}100}$ is the size range least affected by NPF, exhibiting the lowest difference between event and non-event days of all particle size ranges. However, this is the size range that is expected to have the most influence on the CCN concentration and activation properties at low SS. As we can see in Figure 5-5b and Figure 5-5d, $N_{50\text{-}100}$ and N_{CCN} at SS=0.25% follow similar trends with maxima at 15:00 UTC.

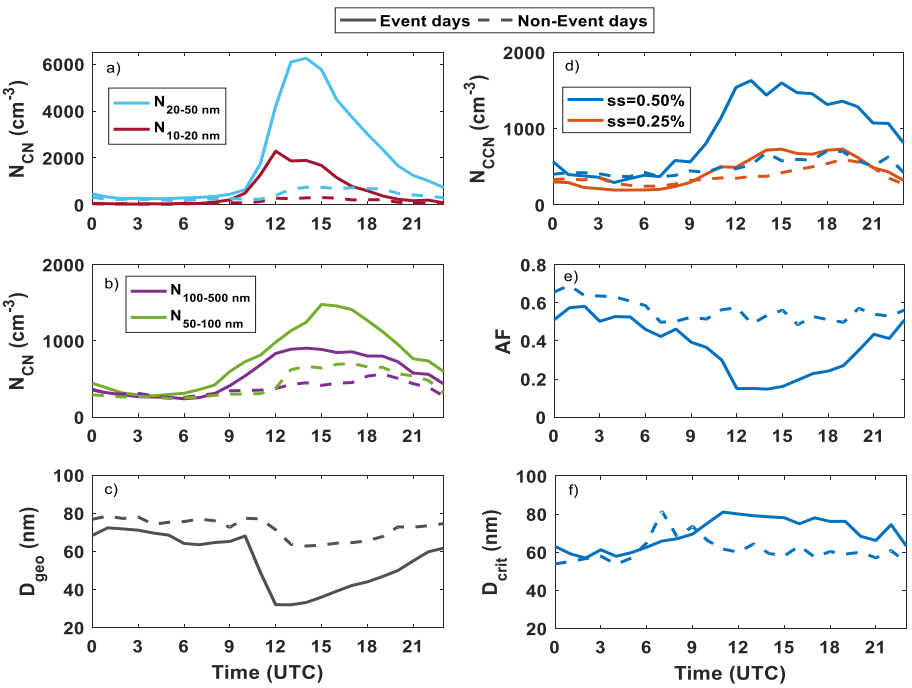

Figure 5-5. Diurnal patterns of (a) and (b) N_{CN} for different diameters ranges, (c) geometric diameter (D_{geo}), (d) N_{CCN} at different SS, (e) activation fraction (AF) and (f) critical diameter (D_{crit}) at 0.50%. Solid lines represent the average diurnal pattern for days classified as NPF event days and dash lines for non-event days at SNS station.

NPF clearly contributes to the increase in N_{CCN} starting at 10:00 UTC, although its contribution is controlled by the SS. It is interesting to note that the difference between N_{CCN} at SS=0.25% and SS=0.50% is larger during NPF event days. For example, the highest value of the ratio between N_{CCN} during event and non-event days is 1.9 at SS=0.25% (14:00 UTC) and 3.1 at SS=0.5% (13:00 UTC). This

suggests that the contribution of NPF can be an important source of CCN in Sierra Nevada especially at high SS. NPF events also affect the values of D_{crit}, D_{geo} and AF. These parameters show smoother diurnal patterns during nonevent days than during event days (Figure 5-5). D_{crit} seems to be less influenced by NPF events but showing a slight increase starting at 10:00 UTC during NPF event days (around 80 nm) compared to nonevent days (around 60 nm). The diurnal pattern of D_{geo} and AF are very similar, with a marked decrease during NPF event days from 10:00 UTC and onwards, reaching their minimum at 12:00 UTC. This evolution is explained by the behavior of N_{10-20} and N_{20-50}. As the concentration of newly formed particles increases suddenly due to nucleation, D_{geo} exhibits a sharp decrease reaching its minimum value (32 nm) at 12:00 UTC. AF has a minimum at the same time (AF=0.15 at 12:00 UTC) due to the high concentration of very small particles that do not activate. After reaching the minimum, AF and D_{geo} start to increase their values due to particle growth during the second half of the day. During non-event days, N_{10-20} and N_{20-50} (typically related to anthropogenic sources), show a smooth increase starting at 12:00 UTC (Figure 5-5a). This and the subsequent decrease observed in AF and D_{geo} are associated with local and transported pollution from the Granada urban area (Figure 5-5c and Figure 5-5e).

To estimate the contribution of NPF to CCN, isolated from other sources like transport of pollutants from Granada, we use the methodology proposed by Rose et al. (2017). This method quantifies the contribution of NPF to CCN by calculating the CCN enhancement (ΔN_{CCN}) from the comparison of N_{CCN} prior to the nucleation event and the maximum during the event. As proposed by Rose et al. (2017), ΔN_{CCN} during non-event days accounts for all CCN sources except NPF events, while ΔN_{CCN} during event days accounts for both contributions. Subtracting one from the other, we can infer the contribution of NPF to CCN alone (ΔCCN_{NPF}). This method assumes that the preexisting particle concentration in the CCN size range at the measurement site is similar during event and non-event days (Rose et al., 2017).

That appears to be the case at SNS based on Figure 5-5a and Figure 5-5b where the solid and dashed lines tend to overlap in the time period prior to the start of nucleation at 10:00 UTC.

Table 5-2. Relative contribution of NPF to CCN activity at different locations (ΔCCN_{NPF}). In Rose et al. (2017) study CCN concentrations were not directly measured, it is marked with an asterisk. Information specifying if an individual event from long-term dataset with the maximum contribution is considered is also specified in the table with an asterisk.

Site Location	Type	SS(%)	ΔCCN_{NPF} (%)	Reference
Shanghai, China	urban	0.20	17	Leng et al. (2014)
		0.60	88	
Vienna, Austria	urban	0.50	38	Dameto de España et al. (2017)
		0.50	143*	
Finokalia, Greece	remote/marine	0.35	88*	Kalkavouras et al. (2019)
		0.52	94*	
Melpitz, Germany	remote	0.40	66	Wu et al. (2015)
		0.60	69	
Chacaltaya, Bolivia	mountain	-	100-250	Rose et al. (2017)*
Sierra Nevada, Granada	mountain	0.25	115	This study
		0.50	175	

The contribution of NPF to CCN in Sierra Nevada, according to Rose et al. (2017) methodology, was 115% and 175% at SS=0.25% and SS=0.5%, respectively. This suggests that NPF plays an important role in the CCN budget at SNS, and, indeed, might be the major CCN source at higher SS. Table 5-2 summarizes the relative contribution of NPF to CCN at different sites compared to Sierra Nevada. For the comparison, it is important to bear in mind that there are several indirect approaches to estimate NPF contribution to N_{CCN} without actual in situ measurements of CCN (e.g., estimating D_{crit} from chemical composition data or just assuming a D_{crit} above which all particles activate). A lower relative contribution of NPF to CCN concentrations was observed at remote environments like Finokalia in Crete (Kalkavouras et al., 2019) and Melpitz in Germany (Wu et al., 2015). Our estimations at SNS are similar to results reported by Rose et al. (2017) for

Chacaltaya Mountain in Bolivia (5240 m a.s.l) where the NPF contribution to CCN ranges from 100% to 250% assuming a D_{crit} of 100 or 50 nm, respectively. In more polluted urban environments like Shanghai and Vienna, the NPF relative contribution to CCN is lower due to the impact of anthropogenic emissions. Dameto de España et al. (2017) pointed out that NPF could also be a measurable, but not very frequent source of CCN in urban environments.

5.4 Predictions of N_{CCN} from ancillary measurements

In this section, we present the results of estimating CCN concentrations from aerosol properties that are more frequently measured than CCN concentrations at most atmospheric observatories (Pandolfi et al., 2018; Schmale et al., 2018). The results of applying Twomey's law following the methodology presented in Section 4.1 are shown in Table 5-3. This table shows linear fit parameters (slope of the fit and, in parentheses, the R^2 coefficient) of Twomey's law C and k parameters and aerosol optical and size distribution parameters. The results are compared with those from other sites around the world (Jefferson, 2010). The R^2 coefficients obtained for UGR and SNS are similar to those reported by Jefferson (2010) at different sites (rural, urban and marine), although in general the correlations are relatively low, especially the correlation between k and SSA. The normalized parameter C/σ_{sp}, which is related to inverse aerosol scattering efficiency, increases with BSF (meaning higher contribution of fine particles) and the slopes have positive values. Jefferson (2010) suggests that higher values of the slope of C/σ_{sp} vs BSF can be related to higher contribution of particles with low scattering efficiency (i.e., organic matter, carbonaceous aerosol particles), while lower values of the slope are associated with a predominance of particles with higher scattering efficiency such as inorganic particles. Alternatively, using N_{80} to parameterize C, instead of BSF, results in

significantly better R^2 values. Note that C is related to the CCN concentration at SS=1%, therefore, C will increase when N_{80} does. At SNS, the calculated slope is higher than at UGR, which means that changes in N_{80} will have a bigger effect on the N_{CCN} estimations.

Table 5-3. Coefficients of linear fits between aerosol parameters and Twomey's law parameters. Each value represents the slope of the fit (the R^2 value is given in parentheses).

Site location	C/σ_{sp} vs BSF	C vs N_{80}	k vs SSA	k vs D_{geo}
Oklahoma, USA	1610 (0.50)	-	-3.78 (0.38)	-
Black Forest, Germany	1430 (0.64)	-	-3.07 (0.20)	-
Graciosa, Portugal	937 (0.33)	-	-2.24 (0.23)	-
Hefei, China	1450 (0.22)	-	-1.73 (0.07)	-
Granada, Spain	1358 (0.40)	0.99 (0.83)	-0.33 (0.03)	0.005 (0.05)
Sierra Nevada, Spain	2183 (0.49)	1.03 (0.77)	-3.52 (0.09)	0.006 (0.12)

Parameterizing k is more challenging, because it is difficult to relate it to other physical or optical properties of the particles. This is reflected in the table showing that the R^2 values are lower for all sites for this parameterization, with no correlation ($R^2 < 0.15$) at both Granada and Sierra Nevada. Fitting k vs SSA yields negative slopes because, as absorbing particle concentration increases, changes in N_{CCN} with SS are lower, principally at low SS. It is caused by absorbing particles like BC that remain non-activated at all SS values. Remote sites with low concentration of BC particles and relatively high SSA, such as Oklahoma, Black Forest or SNS, show the highest absolute values of the slope. Conversely, sites influenced by pollution, with lower SSA, are associated with lower absolute values of the slope (i.e., Hefei and UGR). Using the alternative approach proposed in this study to parameterize k based on size distribution measurements (D_{geo}) does not result in better correlations than those observed with the Jefferson (2010) approach. Despite Jefferson (2010)

limiting the study to SAE > 1 and PM_1 particles, fit parameters at UGR and SNS are within the range of values reported in Jefferson (2010) as can be seen in Table 5-3.

To evaluate the ability of the two empirical models to estimate CCN concentrations at UGR and SNS, we determined the empirical coefficients using 50% of data and used the remaining data for evaluation. To diminish any possible seasonal pattern that might appear in building the model, especially in UGR, we split the data randomly in two subsets, one set is used to build the model and the other one to test it. Figure 5-6 shows the validation of the empirical model proposed by Jefferson (2010) applied to the UGR and SNS datasets. The model provides satisfactory results for UGR. The averaged ratios of predictions vs measurements are: 1.24 at SS=0.3% and 1.14 at SS=0.9%. At UGR the slopes are close to 1 and the R^2 values are close to 0.8 indicating that the model can explain the measurements. The dispersion of data remains roughly constant as SS increases. The model does not show a clear bias due to different values of SSA because data are distributed uniformly according to their SSA value (Figure 5-6). At SNS, the model does not provide satisfactory results. Mean values of predictions versus measurement ratios show that this method overestimates the CCN measurements (1.45 for SS=0.25% and 1.54 for SS=0.7%). The slope and R^2 coefficients are very low in this case and there is wide dispersion of the data because the model is unable to estimate N_{CCN} at SNS when there is a high value of the SSA (Figure 5-6). Additionally, neither the slope nor the R^2 values improve significantly for higher SS values. Since there is no correlation between the k parameter and SSA, the model is not able to reproduce the observed changes in the SSA.

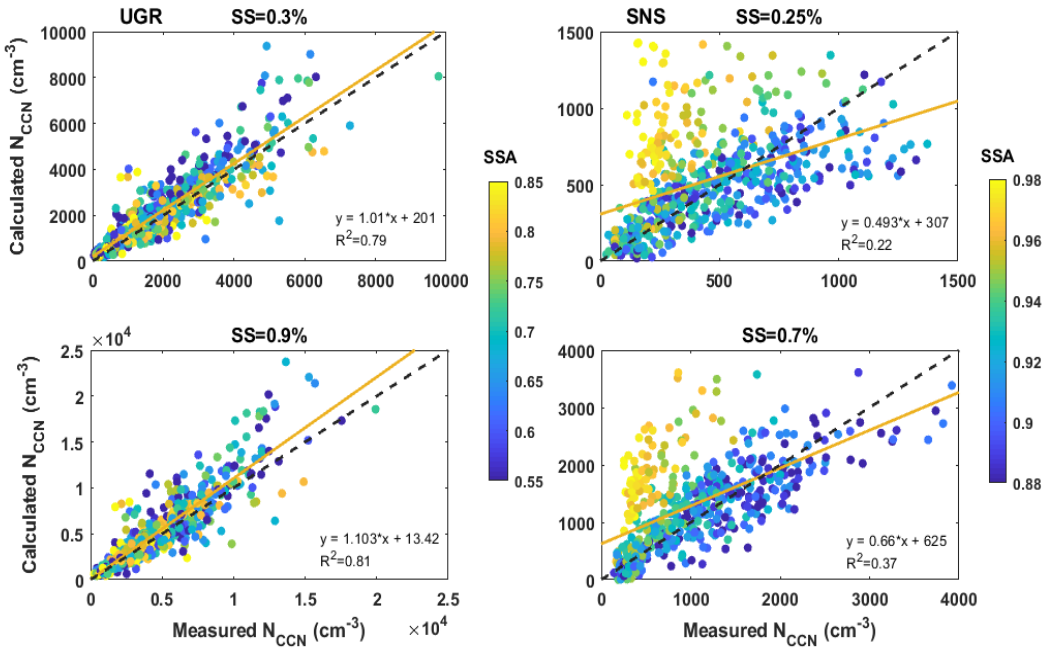

Figure 5-6. Correlations between calculated vs measured N_{CCN} for UGR (left panels) and SNS (right panels) at two supersaturations, color-coded as a function of single scattering albedo (SSA) at 637 nm. Least squares fit and 1:1 line are shown on each graph.

The alternative empirical model based on N_{80} and D_{geo} provides better results at the two stations, except at low SS value at SNS (Figure 5-7). At UGR, this model also provides satisfactory results with values of the slope relatively close to 1 and R^2 close to 0.8. The averaged ratio of predictions and measurements (1.23 at SS=0.3% and 1.27 at SS=0.9%) were similar using this model and the Jefferson (2010) model. At UGR, high CCN concentrations are directly related to large values of the D_{geo}. Also, this model based on N_{80} and D_{geo} is better at reproducing the observations at SNS. In this case, the ratio of predictions vs measurements was 1.24 and 1.29 for SS=0.25% and 0.7%, respectively. The slope and R^2 values show a large improvement at high SS (0.99 and 0.81, respectively) compared to low SS (0.54 and 0.38, respectively). As mentioned in Section 5.2, SNS is highly influenced by NPF events and vertical transport of particles from UGR occurring at midday. These two phenomena could contribute significantly to N_{80}, but at SS=0.25% barely

contribute to N_{CCN}. However, at SS=0.7% these two phenomena contribute to N_{CCN}, and the model reproduces measurements much better than at lower SS (Figure 5-7). As can be seen in Figure 5-7 for SNS, low values of D_{geo} (bluish colors) deviate from the 1:1 line and are more disperse.

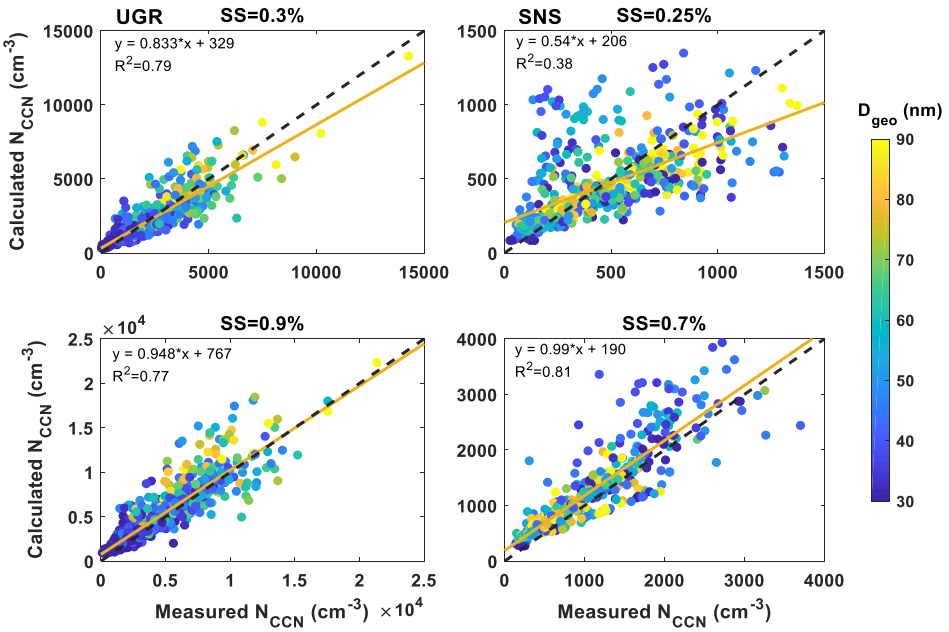

Figure 5-7. Correlations between calculated and measured CCN at UGR (left panels) and SNS (right panels), color-coded as a function of D_{geo}. Least squares fit and 1:1 line are shown on each graph.

Using empirical models, which parameterize Twomey's power law parameters in terms of aerosol properties to predict N_{CCN} remains a difficult challenge. The two empirical models used here are not able to reproduce the measurements in all cases at the two sampling stations; however, it appears that the empirical model based on physical aerosol properties provides a better approach for predicting CCN. The empirical model based on aerosol optical properties provided satisfactory results at UGR but showed low correlations at the mountain station (SNS) between calculated and measured N_{CCN} (R^2<0.4).

5.5 Conclusions

This chapter analyzes the first CCN in-situ measurements performed in the Iberian Peninsula. Measurements were carried out at two different sampling stations: an urban background station (UGR, 680 m a.s.l.) located in the city of Granada and an alpine station (SNS, 2500 m a.s.l.) that is influenced by emissions from the urban area. Measurements of CCN concentration, aerosol light scattering, backscattering and absorption coefficients and black carbon mass concentrations were obtained for the period from October 2018 to end of May 2019 at UGR and from June to end of August 2019 at SNS. Also, measurements of aerosol size distribution in the diameter range 10–500 nm were measured for the period from October 2018 to end of August 2019 at UGR and from June to end of August 2019 at SNS.

At UGR, the N_{CCN} mean value at SS=0.5% was 2500±200 cm^{-3} and the mean value of N_{CN} in the diameter range of 10–500 nm was around $(1.3\pm0.9)\cdot10^4$ cm^{-3} with D_{geo}=45 nm, consistent with typical values of urban environments. Because the D_{crit} at all SS values remained above D_{geo} and was associated with high concentration of BC particles, which are highly non-hygroscopic particles, UGR exhibited extremely low AF (AF is around 0.21±0.11 at SS=0.5%) similar to other urban environments. CCN-derived κ values averaged during the whole UGR campaign ranged from 0.05 to 0.01 at SS = 0.50%. The low κ value is associated with the high contribution of BC particles with low hygroscopicity (κ close to 0), showing the lowest κ values during winter (from December to February) when the BC concentration peaks. The diurnal evolution of aerosol particles at UGR is driven by local emissions, mainly road traffic. During traffic rush hours, N_{CN} achieved its maximum values ($1.99\cdot10^4$ cm^{-3} at 7:00 UTC and $1.83\cdot10^4$ cm^{-3} at 19:00 UTC). According to our results, CCN activity at UGR is clearly controlled by local emissions. Due to anthropogenic sources N_{CCN} can double its background value during the day (around 2000 cm^{-3} at SS = 0.5%), achieving a maximum value of

4200 ± 3000 cm^{-3} at SS = 0.5% at 9:00 UTC. BC mass concentration showed two distinct maxima in coincidence with traffic rush hours. A decrease in AF and κ was observed during traffic rush hours, demonstrating the lower hygroscopicity and activation capacity of fresh traffic emissions.

At SNS, the mean value of N_{CCN} at SS=0.5% was 820±600 cm^{-3} and N_{CN} was around 3000±2800 cm^{-3} with D_{geo}=62 nm. SNS exhibits higher AF values (AF is around 0.5 at SS=0.5%) than are found for UGR, and a more hygroscopic aerosol (the κ parameter is typically in the range from 0.1 to 0.3 at SS = 0.50%). The diurnal evolution of BC mass concentrations at SNS exhibited a maximum around 12:00 UTC, associated with transport of pollutants from the urban area to Sierra Nevada due to the increase in the height of the ABL and upslope transport of pollutants. AF, κ and D_{geo} show a clear minimum around 14:00 UTC. At the same time, N_{CCN} at SS=0.5% and N_{CN} exhibited their maximum values: 1300±800 cm^{-3} and 6600±4000 cm^{-3}. The observed diurnal cycles at SNS are attributed to the joint effect of ABL vertical transport of particles from Granada urban area to SNS and NPF during nucleation events in SNS. Clear differences were observed between non-event and NPF event days. The contribution of NPF to N_{CCN} at SNS was estimated to be 175% at SS=0.5%, suggesting NPF could be the major CCN source at this site.

Different approaches were tested to estimate N_{CCN} from ancillary measurements at both sites. The high diversity in aerosol sources and processes affecting both environments could not be captured in one simple model. At UGR, characterized by high aerosol concentrations with high contribution of absorbing and non-hygroscopic aerosol particles such as BC, both models provided satisfactory results. In contrast, at SNS, which is characterized by low aerosol concentrations with low contribution of absorbing particles and large impact of NPF events, the new scheme proposed here based on N_{80} and D_{geo} provided better results, especially at high SS values. At low SS both models were unable to satisfactorily

simulate the observations, probably due to the fact that the models are not able to reproduce the changes in aerosol properties during NPF events.

In summary, in this chapter it is demonstrated that CCN activity is driven by primary sources, mostly anthropogenic emissions, at an urban site while NPF events have a high impact on CCN concentration during summertime at a high mountain site. Moreover, this study highlights the need to consider these two mechanisms to develop a better CCN parameterization. These findings point out the need to develop experimental campaigns to assess specific questions such as the role that the origin of NPF events (biogenic or anthropogenic, local or regional) may play in CCN concentrations, as well as long-term studies aiming to characterize CCN activation properties throughout the year, especially at SNS. Furthermore, additional measurements such as aerosol chemical composition and estimations of the overall aerosol hygroscopicity (performed in Chapter 7) will allow a better understanding of the joined effects of ABL injections and NPF events and may help in identifying limitations of the simple models used in this chapter.

6 Impact of urban aerosol particles on the cloud condensation activity using a clustering model

This chapter is adapted from "***Impact of urban aerosols on the cloud condensation activity using a clustering model***" by F. Rejano, J.A. Casquero-Vera, H. Lyamani, E. Andrews, A. Casans, D. Pérez-Ramírez, L. Alados-Arboledas, G. Titos and F.J. Olmo-Reyes. Published in *Science of The Total Environment*, Volume 858, 159657, 2023.

As discussed in the previous chapter, urban aerosol particles do not only affect the CCN activity at those urban areas where they are emitted or formed. Urban aerosol particles can be transported to other remote sites influencing the CCN activity. Thus, its impact to global CCN budget is difficult to constraint since urban aerosol particles, which represent the major contribution to the total particle number concentration, are affected by a wide variety of anthropogenic sources and complex atmospheric processes. The objective of this chapter is to estimate the isolated influence on the CCN activity of the main aerosol population types at an urban environment. To this end, a clustering model using PNSD measurements in a wide size range (4–500 nm) is performed to identify the main urban aerosol types at UGR station. Concurrent CCN concentrations are used to determine the influence of each urban aerosol population on the CCN activity.

6.1 Aerosol classification by cluster analysis

In this section, the classification of the PNSD dataset based on the cluster analysis and the corresponding identification of the sources and processes related to each cluster is presented. Then, the resulting clusters are grouped into main aerosol population types according to some explanatory parameters.

The PNSD across 137 size bins (spanning the size range from 4 nm up to 500 nm) with 5-minute time resolution was selected as input matrix for the K-means clustering analysis. All PNSD used are normalized by the maximum of the PNSD because the shape of the aerosol size distribution is related to specific aerosol sources or origin, whereas the absolute values of PNSD might be also influenced by temporal variability along the measurement period. The selection of the optimum number of clusters was obtained using the DB criteria. The choice of using DB criteria is based on: i) Arbelaitz et al. (2013) analysis, which performed an extensive comparative study of the performance of 30 clustering validation indices and identified the DB index as one of the best performing indices, and ii) the computation of the DB index requires less computational time than other validation indices. In this sense, the DB index was calculated for the cluster solution ranging from 3 to 15 clusters and to avoid the initial condition effect on the K-means clustering solution, the clustering was repeated 10 times using new initial centroid positions each time.

Figure 6-1 shows the DB index values for each clustering solution. Two clear minima are observed for the solutions of 5 and 10 clusters, indicating that these two configurations are the best solutions offering well-defined and separated clusters. The clustering solution with ten clusters shows a lower DB value than the five clusters solution (DB index values are 1.403 and 1.411, respectively). Despite the small difference, we selected the 10-cluster solution to reduce the possibility that any cluster included PNSDs from various sources/processes. Afterwards, based on

the scientific context of the site, these 10 clusters will be grouped into five main aerosol categories to study their activation capacity as CCN.

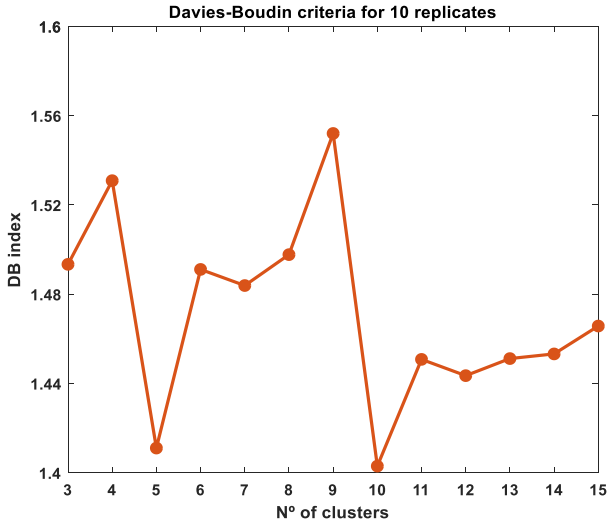

Figure 6-1. Mean Davies-Bouldin (DB) index values for each number of cluster solutions. Each data point is the averaged value for the 10 different replicates of the initial position of centroids.

According to the final 10-cluster solution, Figure 6-2 shows the mean normalized PNSD associated with each cluster resulting from the k-means clustering analysis. According to their frequency of occurrence (diurnal and monthly, Figure S0-3) and their relationship with other atmospheric constituents such as BC and ozone and having analyzed the clustering solution within the scientific context of previous aerosol studies performed in this site (del Águila et al., 2018; Casquero-Vera et al., 2021; Titos et al., 2014b, 2017), we regrouped the 10 clusters into 5 aerosol categories. The reduction of the cluster solution to a more generic classification based on existing knowledge of PNSDs observed has been widely used in the bibliography (Agudelo-Castañeda et al., 2019; Brines et al., 2014, 2015; Dall'Osto et al., 2011; Salimi et al., 2014).

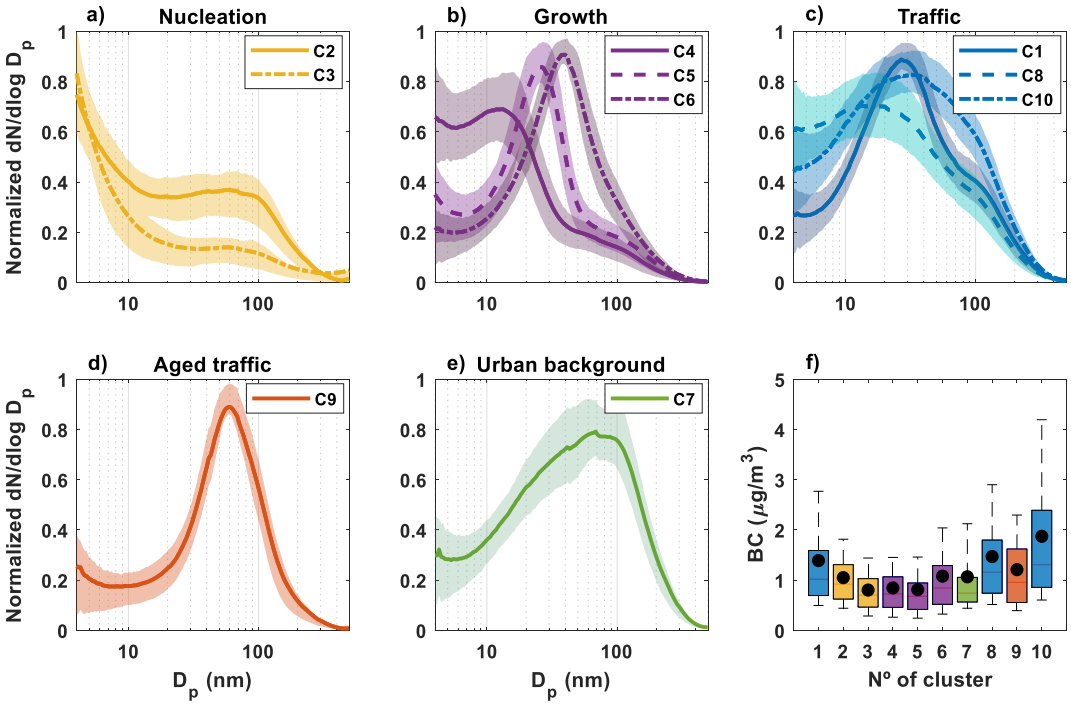

Figure 6-2. Mean normalized PNSD for each cluster. The shaded area represents the interquartile distance (percentile 25th–75th). The 10 clusters are colored according to the aerosol population classification. The right bottom subplot shows the equivalent black carbon (BC) concentration boxplot for each cluster. The black dots represent the mean value.

Table 6-1 summarizes the main characteristics of each of the five categories (also for the whole measurement period) including their frequency of occurrence, the diameter where the maximum of the PNSD is found, the total particle number concentration, BC and ozone concentrations. To ensure that differences between mean values of those variables associated to each category (particle concentration, ozone and BC concentrations) are statistically significant, we have performed an analysis of variance test (Kruskal and Wallis test, which is a non-parametric version of one-way ANOVA; Kruskal and Wallis, 1952) for those variables, in order to check if the means values of each category are significatively different. The result of Kruskal and Wallis test showed p-values $<10^{-4}$, therefore the differences between the tested groups are statistically significant.

Table 6-1. Mean aerosol properties (±STD) for each category and for the whole measurement period.

Aerosol category	N_{tot} ($\cdot 10^4$ cm^{-3})	Maximum of the PNSD (nm)	BC (µg/m^3)	O_3 (µg/m^3)	Frequency of occurrence (%)
Nucleation	1.5±1.2	4	0.9±0.6	65±26	22
Growth	1.4±1.0	23	0.9±0.7	68±25	28
Traffic	1.2±0.7	27	1.6±1.3	61±23	32
Aged traffic	1.1±0.7	60	1.2±0.9	48±22	8
Urban background	0.7±0.4	70	1.1±0.9	59±25	10
Whole period	1.2±0.9	26	1.2±1.0	63±26	100

Below, we describe the five main categories and the clusters included in each one:

- *Nucleation*: This category includes clusters 2 and 3 (Figure 6-2a), both characterized by significant contribution of nucleation mode (<25 nm) particles and similar PNSD shape, exhibiting the PNSD maximum at 4 nm. These clusters occur more frequently during the period from June–August (Figure S0-3a and f) and predominantly at midday. The PNSDs of clusters 2 and 3, together with their frequent occurrence during summer, suggest that these clusters can be associated with freshly nucleated particles during new particle formation (NPF) events that have been previously observed mainly during warm periods at this site (Casquero-Vera et al., 2021). This category represents the 22% of the dataset and show high N_{tot} (cluster 3 has N_{tot} ~$2\cdot10^4$ cm^{-3} and cluster 2 ~10^4 cm^{-3}), higher O_3 concentration and lower BC concentration respect to the averaged value for the whole period (Table 6-1). The high N_{tot} is mainly driven by the nucleation mode that constitutes 67% of the total particle concentration of this category as it is observed during NPF events in previous studies (Casquero-Vera et al., 2020).

- *Growth*: This category includes clusters 4, 5 and 6 that are characterized by PNSD with maxima at 12, 26 and 40 nm, respectively. Each of these clusters represent a different stage of particles growing from smaller sizes. These clusters show a clear relationship with the nucleation clusters as they have low BC and high O_3 concentrations (Table 6-1) as well. This category represents the 28% of the dataset, similar to the nucleation category. These clusters occur more frequently during warm months when NPF events are more frequent, in coincidence with occurrence of the nucleation clusters (Figure S0-3b, g and i). Cluster 4 occurs more frequently between 11:00–13:00 UTC, 2 h later than the nucleation clusters, representing the first stage of growth after NPF events. Freshly nucleated particles grow from ~4 nm (clusters 2–3) to ~12 nm (cluster 4) over approximately a two-hour period. This growth corresponds to a growth rate of ~4 $nm \cdot h^{-1}$ which is in the range of growth rates previously observed in the study area (Casquero-Vera et al., 2020). Cluster 5 represents the second stage of particle growth with the PNSD maximum situated at larger sizes and lower total particle number concentration than cluster 4 (N_{tot} ~$1.2 \cdot 10^4$ cm^{-3}), while cluster 6 represents the last stage of the particle growth with the PNSD maximum at 40 nm and shows the lowest total particle number concentration of the growth category (N_{tot} ~10^4 cm^{-3}). This cluster has its highest frequency of occurrence around 20:00 UTC, especially in summer (Figure S0-3i). At this time of the day, traffic emissions might also influence the observed PNSDs as confirmed by the slightly higher BC concentration observed for this cluster (Figure 6-2f). This explanation of particle growth from the nucleation mode to larger sizes is consistent with previous studies in Granada urban area during NPF events where particle growth rates between 4 and 7 nm ($GR_{4–7}$) and 7 and 25 nm (GR_{7-25}) were 3.6±0.8 nm h^{-1} and 4.5±1.0 nm h^{-1}, respectively (Casquero-Vera et al., 2020).

- *Traffic*: This category comprises the PNSDs associated with clusters 1, 8 and 10, and represents 32% of the data. These clusters show wider size distributions covering the diameter range from nucleation to accumulation mode particles (Figure 6-2c). Their PNSDs have maximums located at 28, 17 and 37 nm, respectively. The total particle number concentration of these clusters is very similar, with mean N_{tot} around $1.2 \cdot 10^4$ cm^{-3} (Table 6-1). However, the key to associate this category with traffic emissions are the statistically significant higher concentration of BC (Figure 6-2f) and the marked diurnal frequency of occurrence with two peaks (Figure S0-3c, h and j) in coincidence with the diurnal cycle of BC (Figure S0-4, 7:00–8:00 UTC morning peak and 19:00–20:00 UTC evening peak). Cluster 10 has its maximum occurrence during the morning traffic peak (around 7:00 UTC) while cluster 8 has its maximum during evening peak (around 19:00 UTC). Differences between these two clusters are the larger BC of cluster 10 (1.87 $\mu g/m^3$, being the cluster with the highest mean BC concentration) and the difference in the nucleation mode sizes with higher contribution in cluster 8. Also, previous studies in this site pointed out that traffic is one of the most important sources of sub-micron particles and the observed diurnal pattern agree with our results (del Águila et al., 2018; Casquero-Vera et al., 2021).
- *Aged traffic*: This category only includes cluster 9 and represents only the 8% of the dataset. The PNSD maximum occurs at 60 nm (Figure 6-2d) and N_{tot} is around $1.1 \cdot 10^4$ cm^{-3}. This cluster shows, after traffic category, the highest BC concentrations, the lowest ozone concentration and occurs mainly between 9:00–10:00 UTC (Figure S0-3d), 2 h after the traffic morning peak (Figure S0-4). This cluster is slightly delayed from morning traffic rush hours and with larger particles than fresh traffic particles was identified in other urban site and also was referred as aged traffic (Agudelo-Castañeda et al., 2019). It is known that volatile gaseous compounds emitted

by traffic can undergo photochemical processes to produce less volatile species, which can promote secondary aerosol formation via condensation (Gentner et al., 2012; Robinson et al., 2007; Rönkkö et al., 2017). This complex chemical process involves some oxidation reactions that might require O_3 to occur (Kroll and Seinfeld, 2008), which is consistent to the fact that this cluster has the lowest O_3 concentration of all clusters (Table 6-1). Therefore, we suggest this ageing pathway as a plausible process affecting these particles.

- *Urban background*: This category is composed of cluster 7 with a frequency of occurrence of 10% over the study period. Mean PNSD of this category shows a maximum at 70 nm (Figure 6-2e) and the N_{tot} is around $0.7 \cdot 10^4$ cm^{-3}, which are the largest diameter and the lowest concentration of all categories (Table 6-1). The low values of BC (mean of 1.1 $\mu g/m^3$) suggest low influence of traffic emissions. Also, cluster 7 occurs normally during night-time when anthropogenic emissions are considerably reduced in the study area (Figure S0-3e). This fact explains the low N_{tot} of this cluster and, together with the maximum of the PNSD located at 70 nm, suggest that this cluster is associated with urban background aerosol. In this sense, similar characteristics of urban background aerosol has been reported previously by Brines et al. (2015) in three different urban sites (Madrid, Barcelona, and Brisbane) with maximum of the PNSD located between 60 and 70 nm. This category was observed at this site during different measurements periods (del Águila et al., 2018). Furthermore, the associated BC concentrations support our observations.

Once we have identified the main aerosol categories in the diameter range between 4 and 500 nm at this site (see the corresponding PNSD for each category in Figure 6-3), we observe that traffic and growth categories are the most important categories in terms of its observation frequency (32% and 28%, respectively) (Table

6-1). Also, we point out that during the analyzed period the PNSD is mainly controlled by traffic emissions and NPF events, including freshly nucleated particles and first stage growth particles, representing the 82% of dataset.

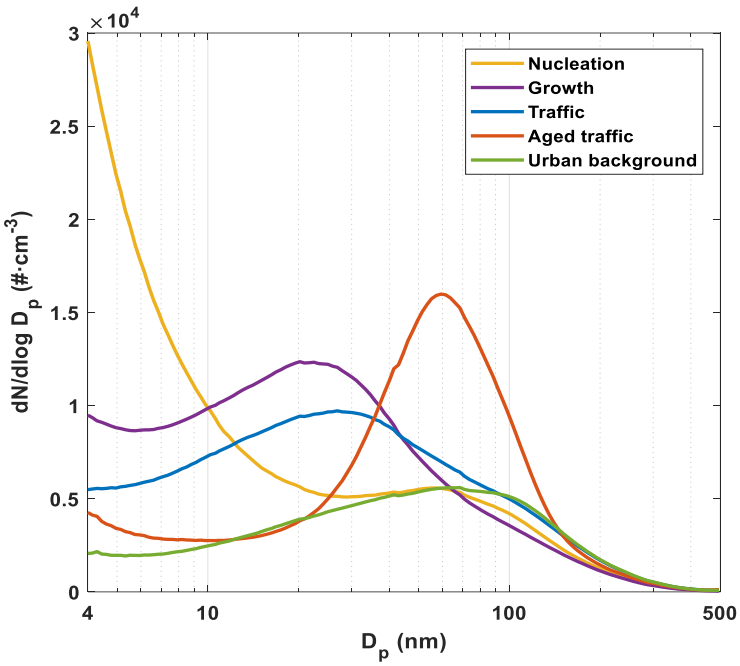

Figure 6-3. Mean PNSD of each aerosol population type.

The five main aerosol categories that we have identified are consistent with previous studies dealing with identification of submicron aerosol sources (del Águila et al., 2018; Casquero-Vera et al., 2021; Casquero-Vera et al., 2020). Despite previous studies in this site observed other aerosol sources such as domestic heating or biomass burning (Casquero-Vera et al., 2021; Titos et al., 2017), we could not identify these aerosol sources since the measurement period lasted until November, when those sources are not activated yet. We realized that traffic influence on the PNSD is not limited to fresh emissions since an indirect influence has been observed due to the ageing of these particles. However, it shows a limited influence in the aerosol population (just an 8% of frequency of occurrence). The retrieved aerosol categories reflect the impact of the multiple urban aerosol sources on the PNSD,

which in turn would lead to differences in the chemical composition. These differences could result in differences in the aerosol activation properties as CCN, and therefore, different effects on cloud formation and climate.

6.2 CCN properties associated with each aerosol category

Based on the previous aerosol classification by cluster analysis, in this section we investigate their relationships with coincident polydisperse CCN measurements at three supersaturation values (SS=0.25, 0.50 and 0.75%). The following activation parameters are investigated for the different aerosol categories: CCN concentration, activation fraction, critical diameter and hygroscopicity parameter. Table 6-2 shows the mean and standard deviation of the activation parameters for the three SS associated with each aerosol category. Also, Figure 6-4 presents the box-whisker plot for these parameters (N_{CCN}, AF, D_{crit} and κ) for the three SS values. A general comparison of each activation parameter and its differences between the main aerosol categories is discussed below. As in the previous section, to check if the differences between the mean values for the different aerosol categories are statically significant, we have performed the Kruskal and Wallis test for all activation parameters associated to each aerosol category. Results of the test showed p-values $<10^{-4}$, which mean that the observed differences are statistically significant.

6.2.1 Influence on N_{CCN}

The mean CCN concentration in this study ranges from 1000 to 2000 cm^{-3} at SS=0.25% and from 1900 to 4600 cm^{-3} at SS = 0.75%. The aged category clearly shows the highest values for all SS values, while the other categories present more similar values, being growth category the one with the lowest N_{CCN} values. All aerosol categories, except aged traffic, exhibit similar mean N_{CCN} values, around 1200 cm^{-3}, due to their similar

PNSD shape in the accumulation size range (between 100 and 500 nm, see Figure 6-3). The urban background category presents a bit higher concentration than nucleation, growth, and traffic (Table 6-2). According to N_{CCN} variability represented by the box and whisker size, aged traffic category shows much more variability than the other categories (Figure 6-4). As the SS value increases all CCN concentrations become higher since smaller particles can activate as CCN. However, not all aerosol categories do so in the same way. The nucleation, growth, traffic, and urban background categories increase their concentrations by approximately 600 cm^{-3} when SS increases from 0.25% to 0.50%; whereas for the same SS change the aged traffic category increases its concentration by 1600 cm^{-3} (Table 6-2).

In Figure 6-5, we show the probability density function (PDF) of N_{CCN} data at the three selected SS. All CCN PDFs have a unimodal distribution for all SS values, except for the growth category which has two modes. In addition, there is a little second mode at larger N_{CCN} concentration in the aged traffic category. The traffic and urban background categories have the narrowest distributions at all SS indicating that N_{CCN} is constrained to a limited range of values in this aerosol category (Figure 6-5). Figure 6-5 also shows that although the traffic category encompasses different traffic clusters, which have different PNSD as mentioned in the previous section, the narrow CCN PDF suggests that all traffic clusters have a similar contribution to the CCN concentration at all SS values.

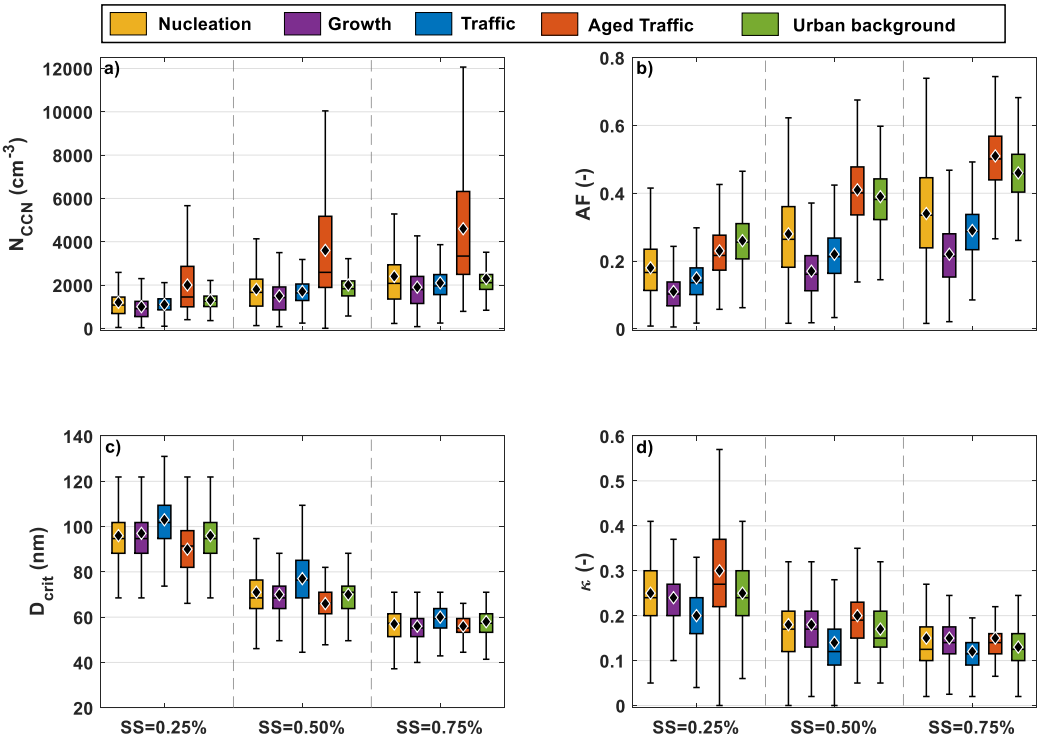

Figure 6-4. Box-Whisker representation for CCN concentration, activation fraction (AF), critical diameter (D_{crit}), and kappa parameter (κ) at SS=0.25, 0.50 and 0.75 % for the different aerosol population categories. The black diamonds represent the mean values for each parameter.

The CCN PDF of the nucleation and growth aerosol categories have a similar shape with a wide distribution that includes low values of N_{CCN}. Therefore, the contribution of these aerosol categories to the CCN concentration was variable during the measurement period in contrast to the contribution of the urban background and traffic aerosol categories which was more constant. The CCN PDFs for the nucleation and growth clusters is wider because their hourly frequency distributions vary by month, due to the temporal variation of the aerosol properties and atmospheric conditions. Both the growth and nucleation categories have a ceiling value of N_{CCN} of around 1000 cm^{-3} at SS=0.25%. Assuming that most freshly nucleated particles are not able to activate, the CCN PDF mode of the nucleation

category could be associated with the background aerosol particles. However, since the nucleation and growth categories exhibit similar CCN PDFs at all SS (Figure 6-5), we assume that the growth category is associated with the same origin as the nucleation category.

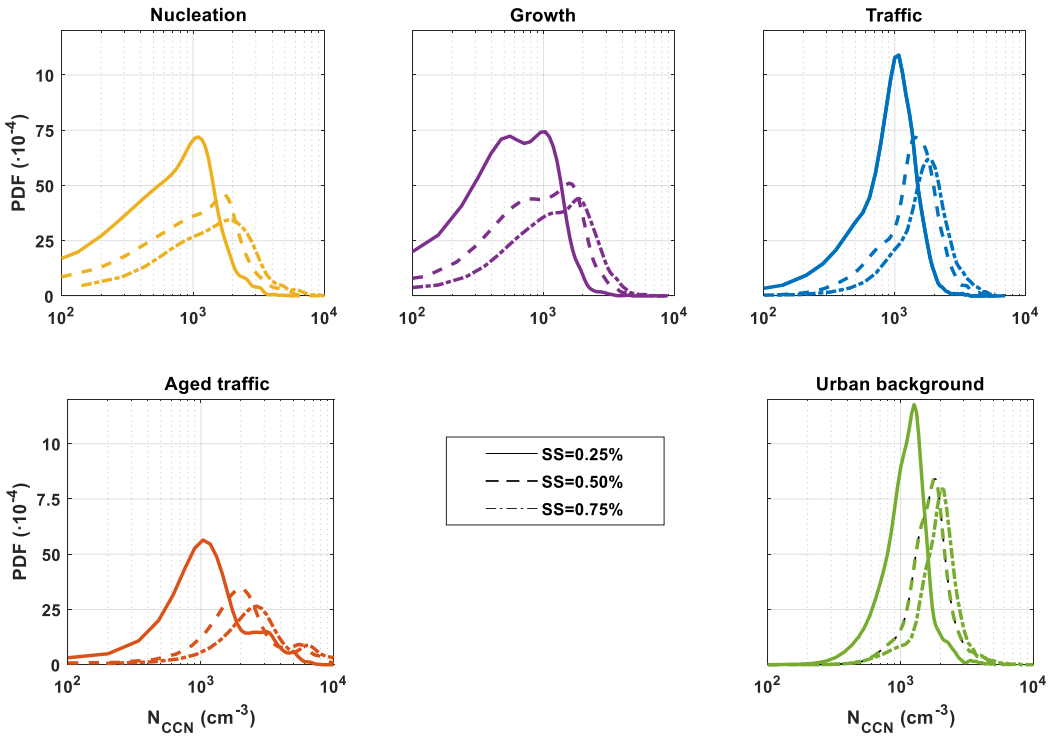

Figure 6-5. Probability density function (PDF) of the CCN concentration at different SS values associated to each aerosol population type.

Lastly, the aged traffic category represents an intermediate situation in terms of the CCN PDF width with respect to the abovementioned cases. Its distribution neither is constrained to a limited range of N_{CCN} (as is the case of the traffic and urban background categories) nor exhibits a clear skewness to low values of N_{CCN} (i.e., nucleation and growth categories). The aged traffic CCN PDF has a primary mode at 1038 cm^{-3} (SS = 0.25 %) and shows some skewness to higher values of N_{CCN} (e.g., the secondary mode at 3131 cm^{-3}, SS=0.25%). Thus, the second mode of the

PDF associated with higher N_{CCN} reveals some specific conditions in which the ageing of traffic emissions could be more efficient at this urban site.

6.2.2 Influence on D_{crit}

The mean D_{crit} values range from 70 nm to 130 nm at SS=0.25%, from 45 to 100 nm at SS = 0.50% and from 30 to 75 nm at SS = 0.75%. The D_{crit} values and variability decrease with supersaturation for all aerosol categories (Figure 6-4c). The D_{crit} for the nucleation category ranges from 96 nm at 0.25% to 57 nm at 0.75%. D_{crit} for the growth category shows very similar values as nucleation category (from 97 nm at 0.25% to 56 nm at 0.75%). Also, the change of this value when increasing the SS values is similar (Table 6-2) and this fact is related to the similar PNSD shape in the range defined by the D_{crit} for both aerosol categories (between 60 and 100 nm, see Figure 6-3). For the traffic category, D_{crit} values ranges from 103 nm to 60 nm from the lowest to the highest SS, being the largest values of all categories (Table 6-2). This fact is consistent with the known non-hygroscopic behavior of traffic particles and explains why the traffic N_{CCN} is lower than the nucleation/growth values even though traffic PNSD presents higher concentration above 80 nm. On the other hand, aged traffic values range from 90 nm at SS=0.25% to 56 nm at SS=0.75%. These D_{crit} values coincide with the particle diameter range where aged traffic PNSD shows its maximum (Figure 6-3). The urban background category presents D_{crit} values ranging from 96±10 nm at SS=0.25% to 58±6 nm at SS=0.75% and shows a similar behavior with SS as the rest of aerosol categories (Figure 6-4c). Therefore, there are not remarkable differences in D_{crit} among aerosol categories. This is explained by the similarities in the PNSD in the diameter range between 60 and 500 nm among all aerosol categories, except for the aged traffic category. The D_{crit} values are similar to other urban sites (influenced by traffic activity, nucleation or aged pollution) reporting D_{crit} values ranging from 50 nm at high SS to 100 nm at low SS (Gunthe et al., 2011; Jurányi et al., 2013; Salma et al., 2021).

6.2.3 Influence on Activation Fraction

The activation parameter that better describes the activation capacity of each aerosol category type is the AF because it provides information about the relative contribution of the whole PNSD to the CCN concentration. Based on the PNSD showed in Figure 6-3 and the mentioned D_{crit} values, AF mean values remain below 0.5 for all aerosol categories at all SS, except for the aged traffic category at SS=0.75% (Table 6-2). From the lowest to the highest SS, mean AF values range from 0.11 up to 0.51. In Figure 6-4b we can observe that the dispersion of AF values (the width of the boxplot) is approximately constant along the different aerosol categories because the variability in N_{CCN} is compensated by the variability in N_{tot}. AF values for growth and traffic categories are the lowest and do not exceed 0.30 even at high SS. In fact, AF values for the traffic category agree with those reported at traffic influenced sites during traffic rush (e.g., Burkart et al., 2011; Cubison et al., 2008). These low AF values are related to the high concentration of particles below 20 nm and the low concentration above 70 nm. Note that nucleation category presents higher AF values than growth and traffic categories which can be explained by the noticeable particle concentration above 70 nm observed in nucleation category (Figure 6-3). On the contrary, the aged traffic and urban background categories have the highest AF values. Also, the increase in AF when increasing SS value is more noticeable in the aged traffic and urban background categories than on the other categories. The diurnal timing of the aged traffic category coincides with the hours mentioned in Chapter 5 (UGR dataset from October 2018 to May 2019) when the maximum value of AF during the day were observed. Also, the AF values for the urban background category are high compared to the other categories since the urban background category PNSD is strongly influenced by accumulation particles.

At SS=0.25% we observe that AF is between 0.15, while at SS=0.50% the AF is 0.25 which is just a quarter of the total particle number concentration that activates as CCN. Those values are typical for urban environments at low and medium SS

values (Salma et al., 2021). However, the aged traffic and urban background categories achieve AF values around 0.4 at SS = 0.50%, similar to the AF mean values for different regional and remote sites analyzed in Paramonov et al. (2015). Moreover, the AF values of the aged traffic and urban background categories are consistent with the AF values identified during the CalWater-2015 field campaign, with AF ranging from 0.2 to 0.6 for SS from 0.2% to 0.7% (Atwood et al., 2019). In the cited study one cluster was identified as a mixed cluster of freshly emitted particles or new particle formation event, whose AF values for the SS values between 0.2% and 0.5% were in the range of 0.15–0.20.

6.2.4 Influence on the hygroscopicity parameter

The hygroscopicity parameter shows a wide range of values for the different aerosol categories. In Figure 6-4d we can observe a decrease of κ value and its range of variability for all aerosol categories when the SS increases (as occurs with D_{crit}). The mean κ parameter values mainly remain below 0.4 and above 0.1 for all SS and shows similar mean values along the aerosol categories (Table 6-2). In the case of the nucleation and growth category, κ shows an identical behavior and ranges from 0.25 at SS=0.25% to 0.15 at SS=0.75%. Traffic category presents the lowest κ which is expected due to the hydrophobic chemical composition associated to fresh traffic emissions. On the other hand, aged traffic and urban background categories have the highest κ values across all aerosol categories at low SS, whereas at high SS all categories present very similar values.

We must consider that the effective hygroscopicity parameter provides indirect information about the hygroscopicity of particles around the D_{crit}. Therefore, depending on the SS value at which the D_{crit} was obtained, the particle hygroscopicity is associated with different particle size ranges. According to the D_{crit} values obtained at the different SS values (around 100 nm at SS=0.25% and 55 nm at SS=0.75%), κ values could be associated with accumulation mode at SS=0.25%

and aged Aitken mode particles at SS=0.50 and 0.75%. Thus, our results suggest that smaller particles (related to Aitken mode particles) are less hygroscopic than larger ones (related to accumulation mode particles). In the case of accumulation mode particles all aerosol categories exhibit similar κ values (ranging from 0.2 to 0.30), which is consistent with the results of Cai et al. (2018) for the Guangzhou region in China. They observed that κ for particles around 100 nm has values between 0.2 and 0.3 using different methodologies, including assessing hygroscopic growth with a humidity tandem differential mobility analyzer (HTDMA), applying a chemical composition approach using an AMS and using a CCNc at SS= 0.20%. In this study, the two aerosol particles categories which are related to aged particles have the highest κ values.

Also, we can observe in Figure 6-4d that the hygroscopicity parameter present a similar behavior as N_{CCN} for all the aerosol categories. Note that the variability (width of the box) of N_{CCN} and κ are similar for each aerosol type, except for the aged traffic category which presents the highest variability in κ and N_{CCN}. Thus, this variability suggests that different ageing processes may lead to higher or lower values of the hygroscopicity parameter (up to a maximum value of 0.45), with CCN concentrations of up to 4000 cm^{-3} at SS=0.25%. The κ parameter for aged traffic category exhibits the highest values of all aerosol populations, confirming our hypothesis that aged traffic particles undergo ageing processes like oxidation due to photochemical reactions. Many studies have investigated the influence that the oxidation level of organic particles has on the increase of κ parameter at urban environments (e.g., Kuang et al., 2020; Wu et al., 2016).

Table 6-2. Overview of activation properties at different supersaturation (mean value ± standard deviation) for each aerosol population and for the whole measurement period. The median value for each variable is also included between parentheses.

		Aerosol category					
SS (%)	**Parameter**	**Nucleation**	**Growth**	**Traffic**	**Aged Traffic**	**Urban background**	**Whole period**
0.25	**N_{CCN} ($\cdot 10^3$ cm^{-3})**	1.2±0.7 (1.1)	1.0±0.6 (0.9)	1.1±0.5 (1.1)	2.0±1.5 (1.5)	1.3±0.5 (1.3)	1.2±0.5 (1.1)
	AF (-)	0.18±0.09 (0.17)	0.11±0.06 (0.10)	0.15±0.06 (0.14)	0.23±0.09 (0.22)	0.26±0.08 (0.26)	0.16±0.09 (0.15)
	D_{crit} (nm)	96±13 (95)	97±13 (95)	103±15 (102)	90±11 (91)	96±10 (95)	98±14 (98)
	κ (-)	0.25±0.10 (0.24)	0.24±0.10 (0.24)	0.20±0.09 (0.20)	0.30±0.11 (0.27)	0.25±0.10 (0.24)	0.24±0.10 (0.22)
0.50	**N_{CCN} ($\cdot 10^3$ cm^{-3})**	1.8±1.2 (1.7)	1.5±0.9 (1.4)	1.7±0.7 (1.6)	3.6±2.5 (2.6)	2.0±0.7 (1.8)	1.9±1.3 (1.7)
	AF (-)	0.28±0.13 (0.26)	0.17±0.08 (0.16)	0.22±0.08 (0.21)	0.41±0.11 (0.40)	0.39±0.09 (0.38)	0.25±0.13 (0.23)
	D_{crit} (nm)	71±13 (69)	70±11 (69)	77±14 (76)	66±14 (66)	70±9 (71)	72±13 (71)
	κ (-)	0.18±0.09 (0.17)	0.18±0.09 (0.17)	0.14±0.08 (0.12)	0.20±0.09 (0.19)	0.17±0.06 (0.15)	0.17±0.09 (0.15)
0.75	**N_{CCN} ($\cdot 10^3$ cm^{-3})**	2.4±1.5 (2.1)	1.9±1.0 (1.8)	2.1±1.0 (2.0)	4.6±3.0 (3.3)	2.3±1.0 (2.1)	2.4±1.6 (2.0)
	AF (-)	0.34±0.14 (0.34)	0.22±0.09 (0.21)	0.29±0.08 (0.29)	0.51±0.10 (0.50)	0.46±0.08 (0.46)	0.32±0.14 (0.31)
	D_{crit} (nm)	57±8 (57)	56±7 (55)	60±9 (59)	56±6 (55)	58±6 (57)	57±8 (57)
	κ (-)	0.15±0.09 (0.13)	0.15±0.07 (0.14)	0.12±0.06 (0.12)	0.15±0.07 (0.14)	0.13±0.05 (0.13)	0.14±0.07 (0.13)

6.3 Summary and conclusions

In this chapter, the PNSD in the size range between 4 and 500 nm and CCN concentrations at various supersaturations (SS) were measured at an urban background site in southern Europe. An unsupervised model based on a K-means algorithm was used to group data according to their PNSD with the aim of identifying urban aerosol sources and processes. The classification resulted in 10 clusters which explain the aerosol population variability during the studied period. According to additional analysis, the different clusters were associated with different aerosol categories: three clusters account for traffic emissions, two clusters for freshly nucleated particles, three for growth particles after NPF events, one for aged traffic emissions and one for urban background particles. The unsupervised classification showed that traffic emissions and NPF events, including freshly nucleated particles and first stage growth particles, are the most frequent aerosol category in this urban environment during the analyzed period, representing around the 80 % of the whole dataset. Moreover, in this study we suggest an important process to consider at urban environments, which is the ageing undergone by aerosol particles from traffic emissions. This aerosol category is observed over a very limited period (only represents the 8% of the dataset) but such ageing can have important implications for the transformations that aerosol particles undergo in an urban environment and determine their ability to act as CCN.

Once the different aerosol categories were identified, we characterized their activation properties to evaluate their influence on the CCN budget. Results showed that aged traffic particles have the largest influence on the CCN concentration for all SS values, whereas the other four aerosol types had a more limited influence on CCN concentration because of their different properties and origin. The nucleation and growth categories had similar contribution to CCN (albeit lower than the aged traffic category), indicating that a further growth/processing is required to observe a relevant

effect of NPF events on CCN concentrations since growth category barely increases the nucleation contribution. The AF, which accounts for the activation efficiency of each aerosol population, showed the highest values for the urban background and aged traffic categories and the lowest for growth and traffic categories, demonstrating the key role of particle size in the activation of particles as CCN. The differences in AF values among aerosol types increased at higher SS values, revealing the differences that exist among the PNSDs. Thus, our results allow to constrain the AF values for all aerosol categories between 0.22 (for growth category) and 0.51 (aged traffic category) at SS = 0.75 %. In this sense, we estimate CCN-active size range for each urban aerosol categories: D_{crit} ranges along aerosol categories 90–100 nm at SS=0.25%, 65–80 nm at 0.50% and 56–60 at SS=0.75%. Related to the hygroscopicity of particles, all aerosol categories show κ values around 0.15–0.30. The traffic category had the lowest κ value as is expected due to the hydrophobic behavior of BC particles dominating these traffic emissions. However, these findings indicated that these particles become more hygroscopic after ageing. The κ for the aged traffic category suggested that these particles had different chemical composition than fresh traffic particles, as well as different size. In this study the activation parameters for the main aerosol categories in an urban were constrained, which could be extended to other urban sites around the world, which help to reduce the uncertainty associated to the CCN concentrations in a regional scale.

To conclude, this chapter highlights the indirect effect of traffic emissions on the CCN concentration. Traffic emissions in urban environment are known to have an important impact on the aerosol population due to their high number concentration, but the direct influence of traffic emissions on the CCN budget is limited. However, when these particles undergo ageing, they could have a significant impact on the CCN concentration (even at low SS values) and may be an important CCN source in urban environments, especially at sites close to high-altitude areas where aerosol is efficiently transported to higher atmospheric layers.

In this sense, aged traffic particles could be transported to other environments where clouds form, triggering a plausible indirect effect of traffic emission on aerosol-cloud interactions which may not have been previously considered.

7 Influence of organic hygroscopicity on CCN under different atmospheric conditions using bulk chemical composition measurements

As demonstrated in Chapter 5, accurate CCN predictions at SNS site are not possible using simple empirical models due to the complex phenomenology observed at this site, which is influenced by anthropogenic particles from the urban area and high frequency of NPF events. Thus, this chapter presents a summer field campaign at SNS with the novelty of measuring the bulk aerosol chemical composition to estimate κ_{chem} and perform CCN predictions based on κ-Köhler theory. To understand aerosol chemical variability and changes in its hygroscopicity occurring at an OA-dominated site, OA sources are identified by using PMF method. In this sense, different OA hygroscopicity schemes are assumed to estimate the overall aerosol κ and assess how organic hygroscopicity influence CCN predictions under different atmospheric conditions.

7.1 BioCloud field campaign overview

In this section we present an overview of the PM_1 chemical composition including OA sources identification using PMF method, and the corresponding analysis related to CCN activation properties during the measurement period from 8 June to 13 July in the framework of BioCloud field campaign. The main objective of the campaign was to evaluate the impact of biogenic and anthropogenic emissions on the CCN budget at a high altitude mountain site, where changes in the CCN concentration may affect the cloud formation processes.

7.1.1 Sub-micron aerosol chemical composition

The average PM_1 concentration along the campaign was 3.85±2.88 μg/m^3, with 10-min concentrations ranging from 0.15 to 15.3 μg/m^3. Figure 7-1a shows the mean PM_1 concentration and relative contribution of the considered species (OA, SO_4^{-2}, NO_3^-, NH_4^+, Chl^-, BC) to the total PM_1. On average, the most abundant aerosol component is OA (2.68 μg/m3), followed by SO_4^{-2} (0.46 μg/m3) and BC (0.33 μg/m3), with relative contributions of 70%, 12% and 9%, respectively. Inorganic components represent 20% of the total PM_1 concentration on average, evidencing the large contribution of organics at this high-altitude remote site during summertime. Similar OA dominance is observed in remote sites worldwide in summertime (Heikkinen et al., 2020; Jimenez et al., 2009; Zhang et al., 2007). The most abundant inorganic component is SO_4^{-2} due to the higher SO_2 oxidation rates under high insolation conditions that favor the formation of this compound (Pey et al., 2009; Titos et al., 2014b). NO_3^- and NH_4^+ species show similar low mass concentrations (0.15 μg/m3) probably due to the summer high temperatures that favor the instability of ammonium nitrate. Chl^- shows a negligible concentration, near to the detection limit of the instrument. The mean BC mass concentration (0.33 μg/m3) is in the range of those previously observed at the studied site (as presented in Chapter 5) and at other high-

altitude remote sites during summer, ranging across all sites between 0.2 and 0.5 µg/m^3 (Gramsch et al., 2020; Ripoll et al., 2015; Zeb et al., 2020).

To gain insight into the local and regional aerosol sources and the underlying atmospheric aerosol processes that control aerosol evolution, diurnal variations of the mass concentration of the measured aerosol species were investigated (Figure 7-1b). Mass concentration of inorganic species show an increase throughout the day starting at 8:00 UTC (local time –2 h). NO_3^- and NH_4^+ species show a similar diurnal pattern and mass concentrations along the day, while SO_4^{-2} show higher mass concentration but a very similar diurnal pattern. OA increases sharply at 8:00 UTC, reaching the maximum between 12:00-16:00 UTC. The BC mass concentration increases more gradually, starting at 3:00 UTC reaching the maximum at 11:00 UTC. According to the diurnal patterns, inorganic species and BC are more likely transported from Granada urban area due to upslope mountain breeze and increase of the ABL height during daytime. OA shows a higher increase in concentration at midday hours compared with the rest of components which might be due to the influence of additional sources of OA in the vicinity of the measurement site.

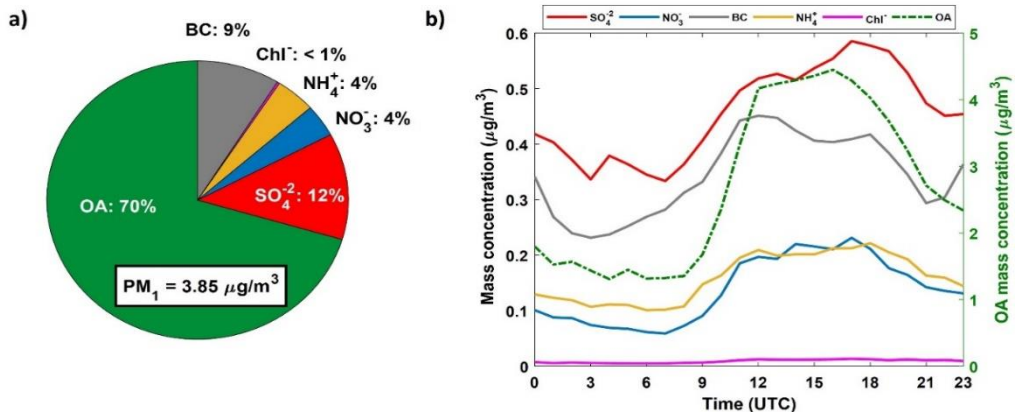

Figure 7-1. a) Pie chart of PM$_1$ mass concentration (OA, SO_4^{-2}, NO_3^-, NH_4^+, Chl^- and BC) averaged along BioCloud campaign, and b) its corresponding mean diurnal pattern evolution.

To further explore the phenomenology of OA, the OA mass concentration was separated into different OA factors by using PMF technique. According to the

Q/Q_{exp} values and the physical interpretation of the PMF solution, the most reliable solution was the 3 factors solution with the following OA sources: hydrocarbon-like OA (HOA), less-oxidized oxygenated OA (LO-OOA) and more-oxidized oxygenated OA (MO-OOA). Once the three OA sources were identified, a new constraint PMF solution was obtained to improve the source apportionment. In this sense, we constrained the HOA factor to Crippa et al. (2013) anchor profile, which is considered the standard mass profile for HOA, with an a-value=0.1. Nevertheless, we don't apply any constraints to LO-OOA and MO-OOA factors to adapt better to the site-specific aerosol characteristics.

The mass spectra profiles and the time-series for each OA factor are presented in Figure 7-2. As mentioned above, the first factor was constrained to standard HOA profile and, therefore, the obtained mass spectrum has high contribution of $C_xH_y^+$ fragments (m/z 41, 43, 55, 57, 69, 71; Figure 7-2a1), also known as aliphatic hydrocarbons. These ions are commonly related to primary emissions of diesel exhaust (Canagaratna et al., 2010; Crippa et al., 2013). The other two factors accounted practically for all OA at SNS (around 95%) and were resolved freely by the model. Both factors (LO-OOA and MO-OOA) are fairly oxidized with high contribution of m/z 28 and 44 (Figure 7-2b1 and Figure 7-2c1). OA at this site is mostly composed of oxygenated OA, which agrees with previous observations at mountain sites during summertime conditions when SOA formation through photochemical oxidation is more efficient (Ripoll et al., 2015). The abundance of m/z 43 ($C_2H_3O^+$) and 44 (CO_2^+) ions indicates the aerosol oxidation degree (Canagaratna et al., 2015) and allows to differentiate the OOA into less oxidized OOA, LO-OOA, and more oxidized OOA, MO-OOA, in terms of the fraction of m/z 43 and 44 respect to the whole mass spectra (f_{43} and f_{44}, respectively) (Ng et al., 2010). The ratio of f_{43} over f_{44} is a good estimation of the oxidation degree and aerosol ageing (Fröhlich et al., 2015; Ng et al., 2010), being higher for LO-OOA

and lower for MO-OOA. We obtained a value of 0.33 for the LO-OOA factor and 0.11 for MO-OOA factor.

The average contribution of HOA factor along the campaign was 5% of total OA and 3.5% of the total PM_1 with sporadic peaks throughout the field campaign (Figure 7-2a2), probably related to occasional local emissions (Jaén et al., under review). Its low contribution highlights the absence of important POA local sources close to the measurement site. The average contribution of LO-OOA and MO-OOA to total OA concentration during the campaign were 36% and 59%, respectively. Differences in the OA sources along the campaign were observed, with the first half of the campaign (before 26 of June) characterized by higher contribution of MO-OOA (mean values for this period were 2.0±1.4 and 0.7±0.8 $\mu g/m^3$ for MO-OOA and LO-OOA respectively), while LO-OOA becomes more relevant during the second half of the campaign (mean values for this period were 1.1±0.9 and 1.2±1.6 $\mu g/m^3$ for MO-OOA and LO-OOA respectively) (Figure 7-2). These differences can be associated to different meteorological conditions between both periods, being the second half of the campaign characterized by higher temperatures, higher pressure and lower relative humidity (Figure S0-5), which might be caused by more efficient mountain-valley breeze during the second half of the campaign. To check the effective transport of aerosol due to mountain-valley breeze regime, BC concentration can be used as a tracer of transported aerosol particles from lower altitudes, due to the absence of local BC sources at SNS. During the second half of the campaign, BC concentration shows a more pronounced diurnal pattern reaching higher concentrations during midday hours compared with the first half of the campaign (Figure S0-6a). Furthermore, evaluation of the ABL height (ABLH) retrieved from ceilometer measurements at UGR during the second half of the campaign reveals the high influence of vertical transport at SNS associated with the ABLH cycle along the day (Figure S0-6b), while the first period is characterized by more stagnant conditions showing less variability along the day. This atmospheric

variability led to differences in the OA origin during both periods. Higher LO-OOA concentration is associated with more efficient transport to SNS due to vertical transport of particles and gaseous precursors from lower altitudes by orographic buoyant upward flows. The higher abundance of MO-OOA in the first half of the campaign might be associated with less efficient transport and predominance of stagnant conditions favoring the presence of more aged particles.

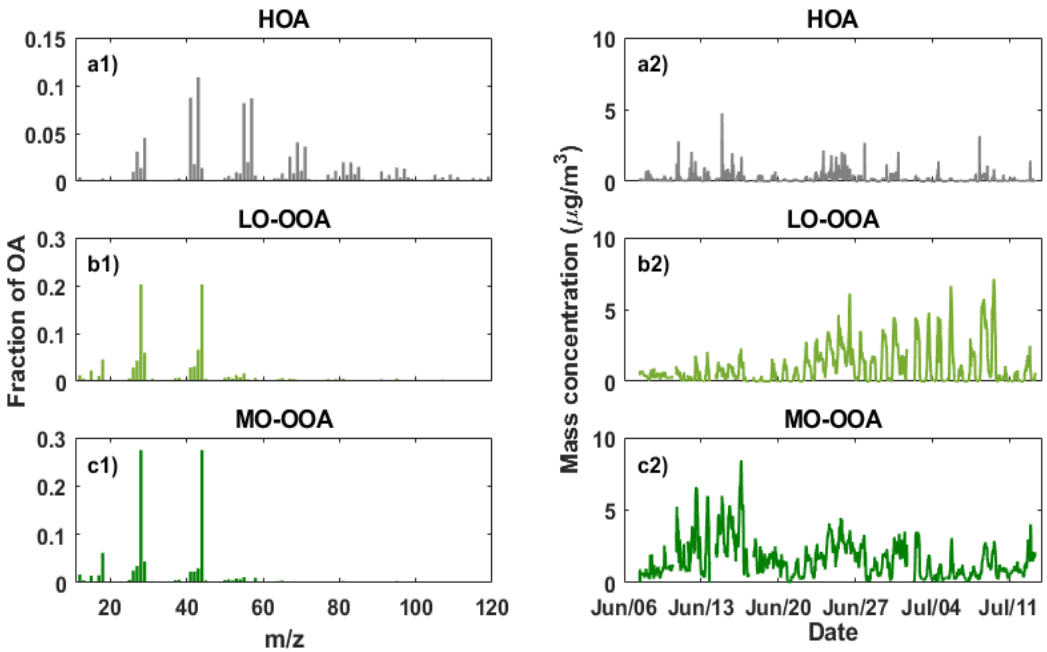

Figure 7-2. Mass spectra of the three OA factors (left panels) and its time series evolution (right panels) during BioCloud field campaign.

7.1.2 CCN activation properties

Aerosol chemical composition plays an important role in defining aerosol hygroscopicity and CCN activation properties (Liu et al., 2018; Svenningsson et al., 2006). In this sub-section we link some aerosol physical properties which are directly related to the CCN activity, such as total particle concentration (N_{tot}), nucleation mode particle concentration (N_{nucl}), Aitken mode particle concentration (N_{Ait}), accumulation mode particle concentration (N_{acc}), and some activation

parameters (N_{CCN}, D_{crit}, CCN-derived κ represented in this chapter by κ_{CCN}, to distinguish from the chemical-derived κ) at different SS values with the sub-micron chemical composition described before. A statistical overview of these parameters (mean, median, standard deviation, percentiles 25th and 75th) are shown in Table S0-2. The mean N_{CCN} values ranged from 320±280 cm^{-3} at SS=0.2% to 800±700 cm^{-3} at SS=0.6%. The mean D_{crit} value at SS=0.2% (111±21 nm) evidence that particle activation is limited to accumulation mode particles. At higher SS some Aitken mode particles start to contribute to N_{CCN}, since mean D_{crit} values decrease with SS (72±18 nm at 0.4% and 58±16 nm at 0.6%). On the other hand, κ_{CCN} values are mainly constraint to the range between 0.1 - 0.25 (which is the interquartile range for all SS, see Table S0-2), showing little dependence on SS with median values of 0.18, 0.15 and 0.13 at SS=0.2%, 0.4% and 0.6%, respectively. Overall, the obtained aerosol activation properties agree with previous observations of these parameters at SNS presented in Chapter 5 and with those reported at other mountain sites during summer (Asmi et al., 2012; Georgakaki et al., 2021; Jurányi et al., 2011).

To evaluate the influence of chemical species on the activation properties, Figure 7-3 shows the mean diurnal patterns of OA factors, IA, BC, total particle number concentration and particle concentration for each aerosol mode (N_{nuc}, N_{Ait} and N_{acc}), along with κ_{CCN} and CCN number concentrations. All variables show a clear diurnal pattern, but with some differences among them. Regarding the different aerosol modes, N_{nucl} showed a clear and sharp peak around midday hours (maximum at 14:00 UTC) due to NPF events (Figure 7-3a). N_{acc} presented a flatter pattern, being this mode associated with the vertical transport due to mountain-valley breeze regime and ABL height increase along the day. N_{CCN} at all SS values follows a similar diurnal evolution (Figure 7-3b) than N_{acc} with maximum CCN concentrations at midday hours and minimum concentrations during nighttime.

The overall hygroscopicity of the activated particles (κ_{CCN}) shows the inverse diurnal pattern than the N_{CCN}, with a decrease during morning and midday hours in coincidence with the N_{CCN} increase. This decrease of κ_{CCN} is accompanied by an increase in the OA contribution to PM_1 (Figure 7-3d), however κ_{CCN} start to decrease around 3:00 UTC, 3 hours before OA/PM_1 ratio start to increase. Between 3:00 and 6:00 UTC, the decrease in κ_{CCN} and OA/PM_1 ratio can be associated to the observed increase of BC during those hours leading to lower κ_{CCN} values. The OA/PM_1 ratio maximum (values higher than 0.75) is observed between 12:00-15:00 UTC due to the higher relative increase of LO-OOA and MO-OOA respect to IA and BC during those hours (Figure 7-3c) in coincidence with κ_{CCN} minimum between 13:00-14:00 UTC for all SS. Figure 7-3c reveals that all species are affected by vertical upslope transport during morning and midday hours, however, LO-OOA might be also affected during midday hours by SOA formation linked to photochemical oxidation induced by high concentration of O_3 and NO_x (Figure S0-7a) together with high temperatures (Figure S0-7b) during midday hours (Minguillón et al., 2016; Via et al., 2021). During nighttime at SNS, we observe the highest values of κ_{CCN} due to the largest contribution of inorganics to PM_1 during those hours. At all SS investigated, κ_{CCN} values are very similar during nighttime (around 0.32), while κ_{CCN} differences between SS values are enhanced during midday hours (Figure 7-3d) since aerosol population becomes more dominated by OA (mainly LO-OOA) and, therefore, higher SS permits to activate less hygroscopic particles. Note that the diurnal pattern of κ_{CCN} at all SS is practically constrained between 0.15 to 0.3, which is in the typical range for hygroscopic organic species (Kuang et al., 2020a), in agreement with the predominance of MO-OOA in our PM_1 measurements. These observations point out that OA dominates PM_1 mass concentration along the day (specially OOA, with higher/lower contribution of MO-OOA/LO-OOA) at this site and its oxygenation degree might control the overall aerosol hygroscopicity at SNS.

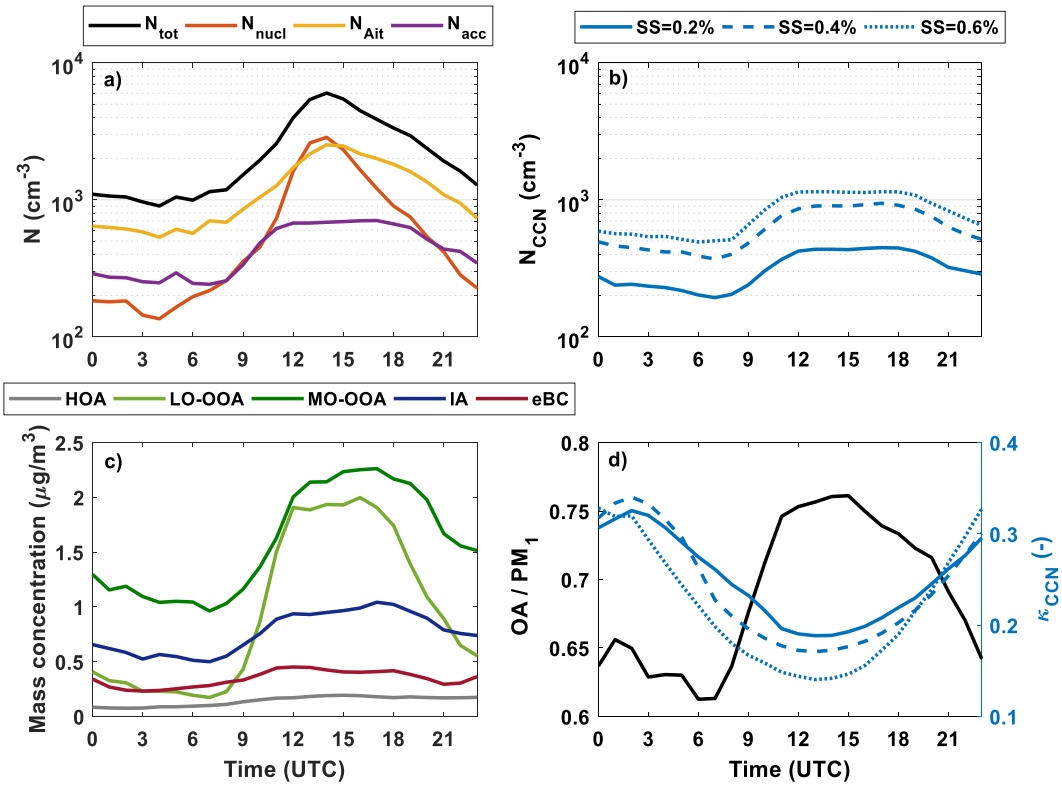

Figure 7-3. Mean diurnal pattern of a) total particle number concentration and each aerosol mode concentration (N_{tot}, N_{nucl}, N_{Ait}, N_{acc}); b) CCN concentrations (N_{CCN}), c) OA factors and IA species mass concentration and d) OA and PM_1 ratio and CCN-derived κ.

7.2 Predicting CCN concentration: role of organic aerosol

In this section we apply different approaches to estimate CCN concentrations and evaluate the impact of OA sources in the overall performance of the closure exercise depending on the underlying assumptions. We use the total aerosol hygroscopicity calculated from PM_1 chemical composition measurements (κ_{chem}) using different organic hygroscopicity schemes for CCN calculation and discuss the degree of agreement of the different CCN closures under different atmospheric conditions. Then, another approach to estimate κ_{OA} in terms of f_{44} parameter is presented to link the hygroscopicity changes with the aerosol oxidation degree. Furthermore, the different atmospheric conditions at SNS along the day (free tropospheric conditions

during nighttime or ABL influence condition during morning and midday) will allows us to evaluate how well CCN estimations based on different OA schemes can explain CCN measurements under different scenarios.

7.2.1 Calculation of CCN using different OA hygroscopicity approaches

To calculate the overall κ_{chem} in order to predict N_{CCN} using κ-Köhler theory, it is necessary to estimate κ_{OA} by assuming some OA schemes as it is mentioned in Section 4.2. Thus, we assumed that OA hygroscopicity can be expressed as follows:

$$\kappa_{OA} = \kappa_{HOA}\varepsilon_{HOA} + \kappa_{MO-OOA}\varepsilon_{MO-OOA} + \kappa_{LO-OOA}\varepsilon_{LO-OOA} \quad \textbf{Eq. (7-1)}$$

According to the OA source apportionment at SNS, we assumed different κ values for the obtained OA factors (HOA, LO-OOA and MO-OOA) to compute the overall κ_{chem} in three different ways:

- Scheme 1: we assume that $\kappa_{HOA} = \kappa_{LO-OOA} = \kappa_{MO-OOA} = 0.1$, which is the typical value observed in a wide variety of environments (Gunthe et al., 2009; Jurányi et al., 2011; Rose et al., 2010; Schmale et al., 2018).
- Scheme 2: we assume that HOA are hydrophobic particles, $\kappa_{HOA} = 0$ (Cappa et al., 2011; Jimenez et al., 2009; Kanakidou et al., 2005; Thalman et al., 2017), and LO-OOA and MO-OOA components have a constant κ value of 0.1.
- Scheme 3: since the level of oxidation of OA affects its hygroscopicity, we assume specific hygroscopicity values for LO-OOA and MO-OOA (κ_{LO-OOA}=0.08 and κ_{MO-OOA}=0.16) as reported by Cerully et al. (2015). HOA is again assumed to be non-hygroscopic (κ_{HOA}=0).

Table 7-1 summarizes the densities and hygroscopicity values of HOA, LO-OOA and MO-OOA used for calculating the κ_{chem} value for the different OA

schemes. The volume fractions of the OA components were obtained assuming the density of OOA as 1.4 g/cm^{-3} and for HOA the typical primary OA (POA) density of 1 g/cm^{-3} (Kuang et al., 2020b; Wu et al., 2016).

Table 7-1. Assumed densities and hygroscopicity values for each OA factor in the different OA schemes.

OA factor	Parameter			
	ρ (g/cm^{-3})	κ (-)		
		Scheme 1	**Scheme 2**	**Scheme 3**
HOA	1	0.1	0	0
LO-OOA	1.4	0.1	0.1	0.08
MO-OOA	1.4	0.1	0.1	0.16

Figure 7-4 shows the violin plots of the retrieved κ values under each OA scheme, κ_{chem}, and the calculated κ values from the CCNc measurements, κ_{CCN}, at different SS. The κ_{chem} values show lower variability (ranging from 0.1 to 0.35) compared to the κ_{CCN} (from 0.06 to 0.7). The probability density function (PDF) of κ_{chem} for schemes 1 and 2 are very similar, with maximum around 0.14. The main difference in the data distribution between both schemes is observed at low hygroscopicity values when HOA contribution is higher, i.e., during sporadic HOA peak events. The OA scheme 3 shows a clear different data distribution compared to schemes 1 and 2 due to a different assumption that establishes a time dependent κ_{OA} in terms of the relative contribution of LO-OOA and MO-OOA factors. The κ_{chem} of scheme 3 shows in general higher values (mean and median values are 0.20) since we assumed a higher hygroscopicity for the MO-OOA factor, which is the main factor controlling OA at SNS. Also, we can observe that data is more homogenously distributed around the mean value for scheme 3 while schemes 1 and 2, the PDFs are skewed towards lower values (Figure 7-4).

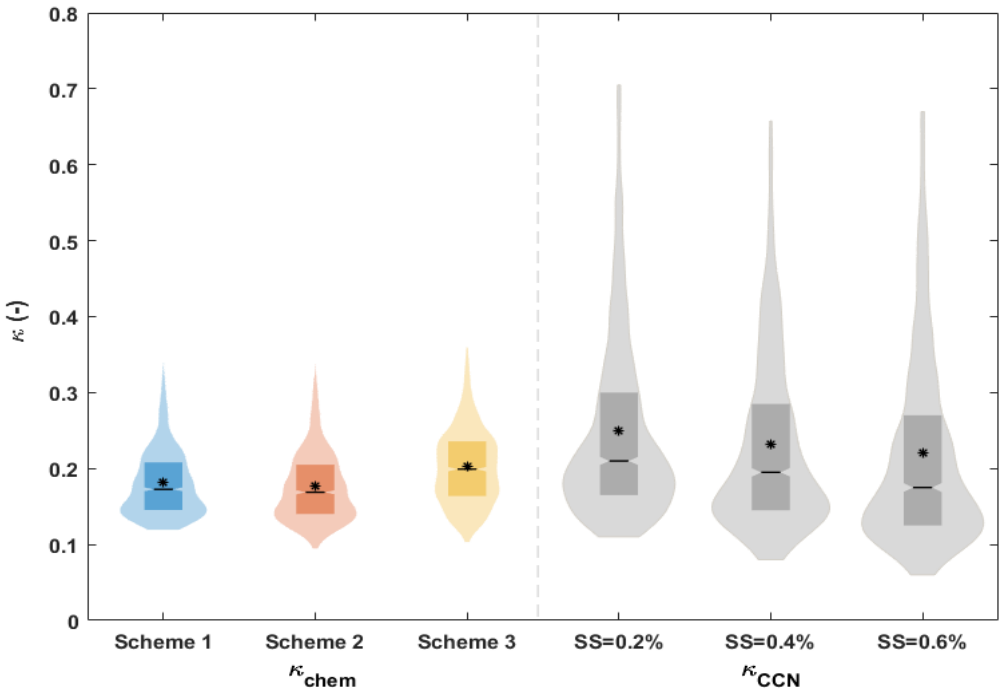

Figure 7-4. Violin plot of κ distribution data for the chemical schemes (κ_{CCN}) and the CCN calculation at different SS values (κ_{chem}). The boxes represent the interquartile distance, and the asterisk is the mean value.

The κ_{CCN} values show very different data distribution respect to κ_{chem} values. All κ_{CCN} PDF show a clear maximum and positive skewness with some outlier observations (higher mean than median values). This can be due to the larger variability of the parameters used to retrieve aerosol hygroscopicity in the supersaturated regime (i.e., N_{CCN} and PNSD via κ-Köhler theory) compared to changes in chemical composition. This is particularly important in the case of SNS since the sub-micron chemical composition is dominated by OA, and despite the changes in hygroscopicity among OA constituents the range of change is quite limited, being κ_{chem} less sensitive to temporal changes in composition. As anticipated, higher SS values result in a shift to lower values in the data distribution due to activation of less hygroscopic particles. Across all SS values, mean κ_{CCN} are higher than κ_{chem} for the different OA schemes. However, the differences between

κ_{CCN} and κ_{chem} median values are minimal. The OA schemes 1 and 2 (median values of 0.17) seem to explain better the κ_{CCN} at SS=0.6% (median values of 0.18), whereas scheme 3 (median value of 0.20) is closer to κ_{CCN} at low SS (median value of 0.21). It is important to remark some considerations about both methods to estimate the overall κ. The κ_{CCN} accounts only for activated particles in the CCNc, whereas κ_{chem} accounts only for aerosol particles in the size range allowed by the aerodynamic lens in the ToF-ACSM. Therefore, depending on the supersaturation considered, both instruments may be measuring particles in different size ranges (as mentioned in Section 3.2). This effect might influence more the analysis at SS=0.6% because the median D_{crit} is 60 nm at this site and is out of the range of the optimum size range of the ToF-ACSM (70-700 nm). Moreover, both methods assume internally mixed particles to estimate the overall κ, which is an important limitation in the case of externally mixed particles (Kulkarni et al., 2023; Ren et al., 2018; Wang et al., 2010).

Based on the obtained κ_{chem} values we estimated CCN number concentration using κ-Köhler theory with a time-resolution of 30-minutes. The comparison between predicted and measured N_{CCN} at the different SS values for the different OA schemes is shown in Figure 7-5. Also, it is included in the comparison the simplest approach to estimate N_{CCN} from PNSD data, which consists in assuming that particles above a certain size are activated. In this case, we selected 80 nm as the fixed activation diameter and N_{80} (number concentration of particles with diameter larger than 80 nm) is used as a proxy for N_{CCN}. This threshold diameter has been selected because at medium SS values (0.4-0.5%), the D_{crit} for a wide variety of aerosol types is constrained between 70-90 nm (as observed in Chapter 6). We observe that there is a dependency on the CCN closure with SS when the N_{80} approach is used. This is expected since this simple approach does not include the D_{crit} dependence with SS. In this case, the predicted N_{CCN} values overestimate the measurements at low SS and underestimate the measurements at high SS level. In

fact, at SS=0.4% the mean D_{crit} is 72±18 nm and, therefore, despite the diurnal and day-to-day variability in D_{crit} which might hampered the predictions using N_{80}, the N_{80} proxy explains very accurately the N_{CCN} observations at this specific SS with the best correlation coefficient (r=0.94) and slope of the regression (1.06).

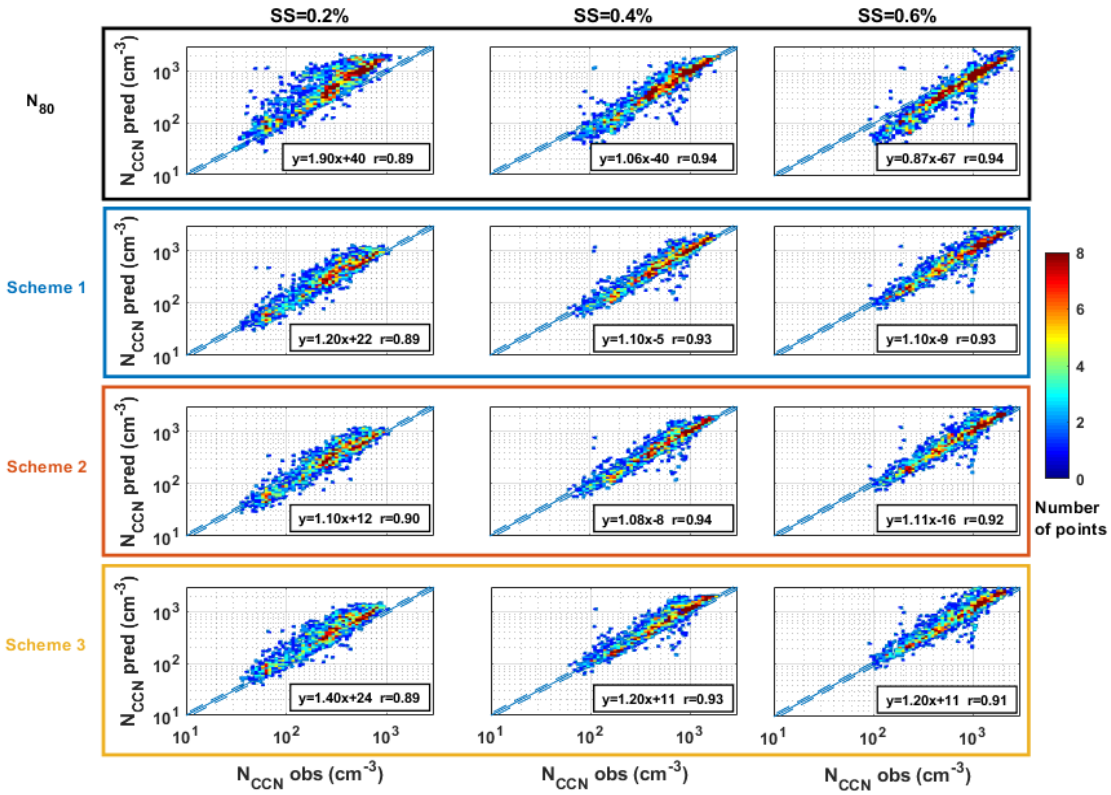

Figure 7-5. Log-log scatter plot of predicted CCN concentrations (N_{CCN} pred) as a function of observed CCN concentrations (N_{CCN} obs) using the four prediction schemes. The solid blue line represents the 1:1 line and the dashed lines are the +/-10%. The linear equation and Pearson correlation coefficient (r) are also included.

Concerning the chemical approaches under different OA schemes show similar CCN closures for all SS. The slopes and correlation coefficients are also in all cases near 1, except of scheme 3 that shows consistently higher slope values than the other two schemes (Figure 7-5). All the OA schemes overestimate the CCN observations with slope values ranging from 1.08 to 1.4 and correlation coefficients between

0.89-0.94. A slightly worse agreement between predictions and observations is observed at SS=0.2% probably due to higher discrepancy between κ_{CCN} and κ_{chem} at this SS, as previous results pointed out for low SS values (Cai et al., 2018; Mei et al., 2013). These results are in agreement with other CCN closures studies based on bulk chemical composition under varying assumptions of OA hygroscopicity (e.g, Kulkarni et al., 2023; Meng et al., 2014; Ren et al., 2018; Zhang et al., 2017). Closure results for schemes 1 and 2 are very similar due to the low contribution of HOA at SNS. Despite the observed difference in κ_{chem} values between both schemes (1 and 2) the impact on the CCN concentration estimation is minimal. Concerning scheme 3, the results evidence that assuming a lower/higher κ for LO-OOA/MO-OOA, respectively, rather than the standard κ_{OA}=0.1, leads to a higher overestimation of the predicted N_{CCN} (especially at SS=0.2%), which suggests that the κ values assumed for LO-OOA/MO-OOA as suggested by Cerully et al. (2015) are probably too high. However, scheme 3 results show no improvement in the correlation coefficients obtained, which are similar to those of scheme 1 and 2, denoting that including the variable contribution of OA sources does not improve the results. Despite the large variability observed in the OA components, our results demonstrate that the simple approach of assuming a constant κ_{OA} of 0.1, even at a complex environment dominated by OA, seems to provide satisfactory predictions of CCN concentration. Mei et al. (2013) obtained good CCN closures at OA-dominated sites (70-80% of PM_1) assuming a constant κ_{OA} of 0.08 and 0.13 (which is very close to κ_{OA}=0.1 used in this study). Rose et al. (2011) reported N_{CCN} overestimations of 20% assuming κ_{OA}=0.1 near Guangzhou area (China), but better results (overestimations of 10%) were observed when considering further assumptions about the hygroscopicity of low volatility particles. Assuming κ_{OA}=0.1 using both bulk and size-resolved chemical composition measurements, Meng et al. (2014) showed at a coastal site in Hong Kong that N_{CCN} overestimations reached values of 26% and 10%. These authors concluded that CCN closures can be less

sensitive to hygroscopicity considerations and mixing state considerations may play a role. Conversely, Ren et al. (2018) demonstrated at an urban environment that aerosol mixing state can play a minor role in CCN prediction when κ_{OA} exceeds 0.1 and obtained good closures (closure ratios of 1.0-1.16) using bulk chemical and internally mixture assumptions in Beijing urban area under clean conditions. Also, Siegel et al. (2022) obtained N_{CCN} closure (slopes between 0.82-0.91) in the Arctic under internally mixed assumptions by characterizing very precisely the organic hygroscopicity based on laboratory experiments and field observations. When considering remote sites without the influence of local emissions, Cai et al. (2018) demonstrated that either bulk or size-resolved chemical composition measurements can achieve practically the same agreement in N_{CCN} predictions. Therefore, the accuracy of N_{CCN} predictions can show a wide variety of results depending on the characteristics of the experimental site and the associated atmospheric conditions.

To get a deeper understanding of the performance of CCN predictions and gain knowledge on how the differences in OA composition along the day may or may not affect the CCN predictions, we calculated the diurnal evolution of the relative bias ($[N_{CCN}{}^{pred}-N_{CCN}{}^{obs}]/N_{CCN}{}^{obs}$) of the N_{80} approach and each OA scheme. Since there are no significant differences on the impact of different OA schemes on the estimation of the CCN at different SS values, from now on, we focus the analysis at SS=0.4%. Also, only at this SS the N_{80} approach performed satisfactorily because the D_{crit} is close to 80 nm. As explained in previous sections, the measurement site shows a strong diurnal variability that is reflected in differences in aerosol size distribution and chemical composition along the day, allowing us to investigate which atmospheric conditions favor better CCN predictions. Figure 7-6 shows the median diurnal evolution of the relative bias of each scheme for SS=0.4%. In this analysis we consider accurate CCN predictions when the associated uncertainty is within the range of ±10% (grey shadowed area in Figure 7-6), which is the instrument uncertainty associated to N_{CCN} (Schmale et al., 2017). All schemes show

a similar relative bias diurnal pattern with lower values during nighttime hours and higher during midday hours. There is a clear difference between the relative bias pattern obtained by N_{80} and the OA schemes. In Figure 7-6a the diurnal pattern of D_{crit} at 0.4% and the threshold size of 80 nm are also represented. As expected, the difference between the observed D_{crit} and the assumed threshold size (80 nm) is clearly related to the bias value and, in general, being positive/negative bias associated with D_{crit} values larger/smaller than 80 nm. The largest deviations respect to observations are found during nighttime hours (underestimations between 20-30%), when the D_{crit} is considerably below 80 nm. Therefore, the use of this approach should be limited to situations when the D_{crit} is fairly constant keeping in mind that the CCN prediction is limited to a specific SS.

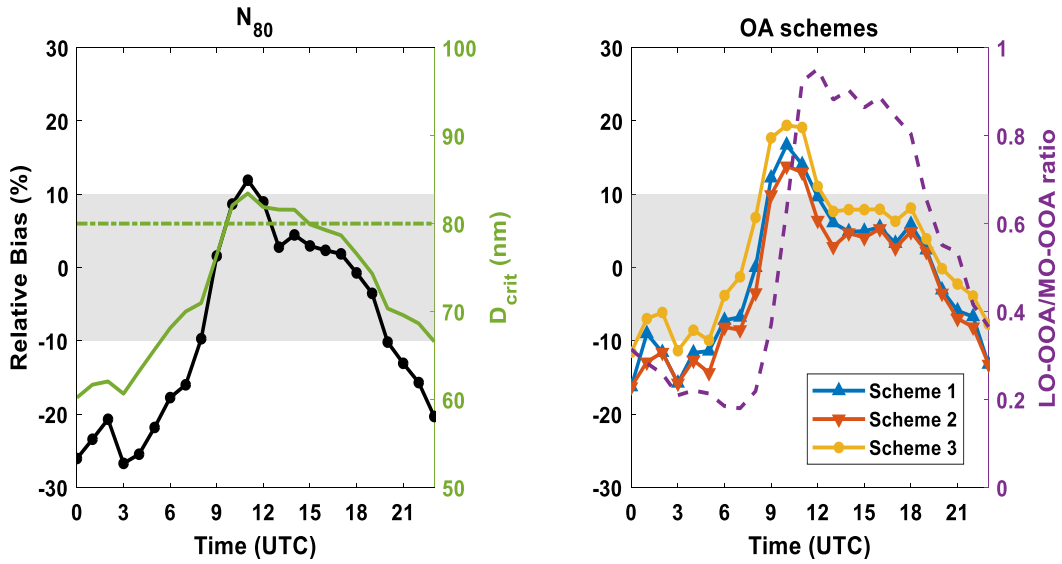

Figure 7-6. Diurnal evolution of the median relative bias in CCN predictions at SS=0.4% for each prediction scheme. The grey shaded area in all panels represents the ±10% relative bias. The D_{crit} at SS=0.4% is presented in panel a) and the horizontal line represents the threshold size of 80 nm. The ratio between LO-OOA and MO-OOA mass concentrations is presented in the right Y axis in panel b).

Concerning the OA schemes, the diurnal evolution of the relative bias is similar to the N_{80} approach with lower relative bias during nighttime and higher during daytime. The relative bias takes values in the range from -6% to -16% for all OA

schemes during nighttime period associated with free tropospheric conditions dominated by aged aerosol (OA is dominated by MO-OOA). Conversely, during morning/midday hours the relative bias increase from its minimum value at 6:00 UTC (3-8% underestimations) to it maximum value at 10:00 UTC (14-20% overestimations) (Figure 7-6b). The ratio of LO-OOA over MO-OOA is also included in Figure 7-6b to link the N_{CCN} relative bias with changes in the OA composition. We can observe that both diurnal patterns (LO-OOA/MO-OOA ratio and relative bias) show similar shape, but with 1 hour of delay between both maxima values. This fact reveals that the largest bias occurs when the relative contribution of LO-OOA and MO-OOA start changing. When the ratio LO-OOA/MO-OOA is constant the relative bias remains constant as well.

To sum up, our results evidence that the relative bias in CCN predictions with the OA schemes is highly dependent on the LO-OOA and MO-OOA variability and relative contribution to OA. Since both factors show different oxidation degree, in the next section we present a new OA scheme that describe κ_{OA} in terms of OA oxidation degree.

7.2.2 Retrieval of ambient κ_{OA} for evaluating CCN calculation

In this sub-section we calculate κ_{OA} based on κ_{CCN} and considering that κ_{IA} and κ_{BC} are well-known term using Eq. (4-3) (e.g., Cerully et al., 2015; Kuang et al., 2020b; Thalman et al., 2017):

$$\kappa_{OA} = \frac{\kappa_{CCN} - \kappa_{IA}\varepsilon_{IA} - \kappa_{BC}\varepsilon_{BC}}{\varepsilon_{OA}} \qquad \textbf{Eq. (7-2)}$$

Figure S0-8 shows the probability density function (PDF) for the effective κ_{OA} at SS=0.4% retrieved with this method. The mean and median values of κ_{OA} were 0.18 and 0.15, respectively, which is within the range of ambient κ_{OA} observations in the supersaturated regime (e.g., Gunthe et al., 2011; Kawana et al., 2016; Levin et al., 2014). The PDF distribution shows its maximum at κ_{OA}=0.11, which is similar

to the assumed κ_{OA} in previous sub-section (~ 0.1). Previous studies have parameterized κ_{OA} as a function of the oxidation degree using the f_{44} parameter (Kuang et al., 2020b and references therein). Therefore, we explore a potential improvement of κ_{OA} calculation at SNS by establishing a new OA scheme (named here as scheme 4) based on a linear relationship between κ_{OA} and f_{44}. In this way, we can calculate the κ_{chem} based on the mentioned parameterization as follows:

$$\kappa_{chem} = (m \cdot f_{44} + n)\varepsilon_{OA} + \kappa_{IA}\varepsilon_{IA} + \kappa_{BC}\varepsilon_{BC} \quad \textbf{Eq. (7-3)}$$

where m and n are the slope and the intercept of the linear relationship between κ_{OA} and f_{44}. To establish the parameterization, the dataset has been split randomly in two subsets: the first one is used to obtain the linear regression and the second one to check its performance for CCN calculation. Each data subset consists of 50% of the data. Furthermore, we re-sampled the f_{44} values into 80 bins and obtained the corresponding κ_{OA} values. Then, the empirical parameterization was obtained by establishing a linear regression between the averaged κ_{OA} values and f_{44}. As shown in Figure 7-7 there is a clear linear trend between the binned values of κ_{OA} and f_{44}. For high values of f_{44} (specially above 0.28) the κ_{OA} values show higher dispersion. The κ_{OA} and f_{44} relationship obtained in this analysis (slope of 3.24) is defined for high values of f_{44} (ranging from 0.2 to 0.32) due to the high oxidization degree of OA and the low contribution of HOA at this site. Previous studies that reported a linear relationship between κ_{OA} and f_{44} were developed for f_{44} values ranging from 0.05 to 0.20 (Chen et al., 2017; Duplissy et al., 2011; Kuang et al., 2020b; Mei et al., 2013). Those studies also reported lower slopes for the κ_{OA}-f_{44} relationship ranging between 2.1-2.4. These studies were performed at OA-dominated sites during warm season and observed lower f_{44} values due to a higher contribution of HOA and biomass burning related OA (Chang et al., 2010; Duplissy et al., 2011; Mei et al., 2013). For fresh emitted biomass burning particles, Chen et al. (2017)

obtained also lower slope value of 2.3 associated with low f_{44} values. Significantly lower slope for κ_{OA}-f_{44} relationship (1.04) was reported by Kuang et al. (2020b) at the north China plain during winter with higher contribution of HOA and coal combustion OA (f_{44}<0.15). The κ_{OA}-f_{44} relationship retrieved in this study lies in the opposite extreme, showing the largest slope in the κ_{OA}-f_{44} relationship. Therefore, our results suggest that κ_{OA}-f_{44} relationship depends on the oxygenation degree of the organic particles. Nevertheless, some of the variability observed among studies in the κ_{OA}-f_{44} relationship might arise from differences in κ_{OA} calculation, such as subsaturated or supersaturated regime or bulk or size-resolved measurements (Kuang et al., 2020a).

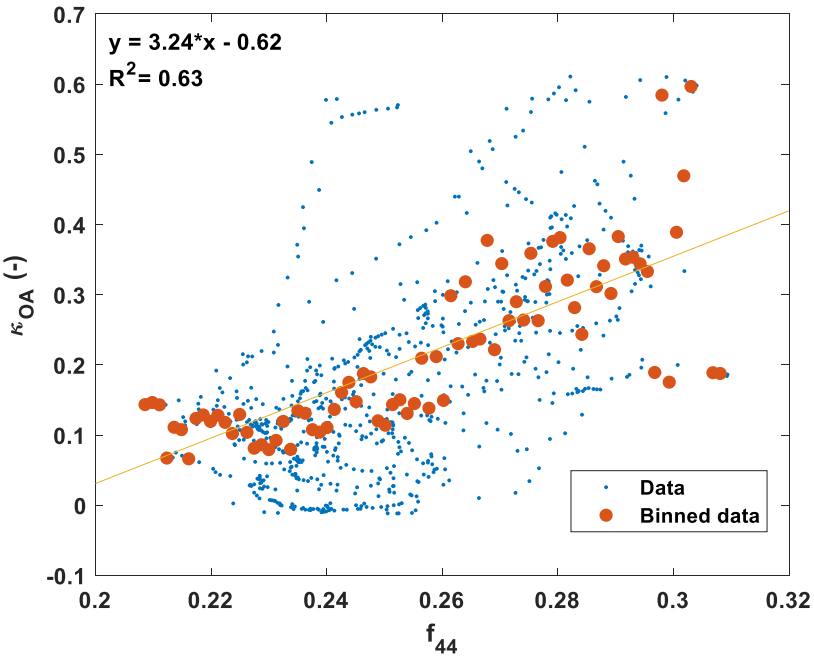

Figure 7-7. Scatter plot of κ_{OA} at SS=0.4% respect to f_{44}. The liner regression is applied to the binned data.

The CCN closure at SS=0.4% for this OA scheme shows similar slope and correlation coefficient than the other OA schemes (1.13 and 0.93, respectively, see Figure 7-8a). For high f_{44} values (>0.25) the CCN closure is better (slope of 1.05),

while for low f_{44} values (<0.25) the CCN predictions tend to overestimate the CCN concentrations and show higher data dispersion. This fact is also observed in the median diurnal pattern of the relative bias (Figure 7-8b). During nighttime conditions (when high f_{44} values are observed) the new OA scheme can explain the observations within the ±10% range and improves the results obtained with the previous OA schemes. However, the relative bias increases up to 35% (Figure 7-8b) during morning and midday hours which are characterized by lower f_{44} values associated with higher LO-OOA contribution. The sensitivity of κ_{OA} to changes in f_{44} is highly dependent on aerosol sources and atmospheric conditions, and significant deviations have been observed when POA dominates the organic aerosol mass (Kuang et al., 2020a). At SNS the contribution of POA is negligible and however, the new OA scheme including a specific parameterization of κ_{OA} as a function of f_{44} does not constitute a significant improvement for CCN predictions. Our results are comparable with Zhang et al. (2016) results that analyzed the impact of aerosol oxidation level on CCN predictions at a suburban site in Northern China using the κ_{OA}-f_{44} relation obtained by Mei et al. (2013). They showed for OA mass fractions higher than 0.6 that N_{CCN} predictions are very sensitive to f_{44} values and the best CCN closures were observed for f_{44}>0.15 with slope value around 0.94 at SS=0.39%. As observed in this study and in Zhang et al. (2016), accurate N_{CCN} predictions at OA-dominated sites using κ_{OA}-f_{44} relation is challenging since both κ_{OA} and N_{CCN} are very sensitive to f_{44} values.

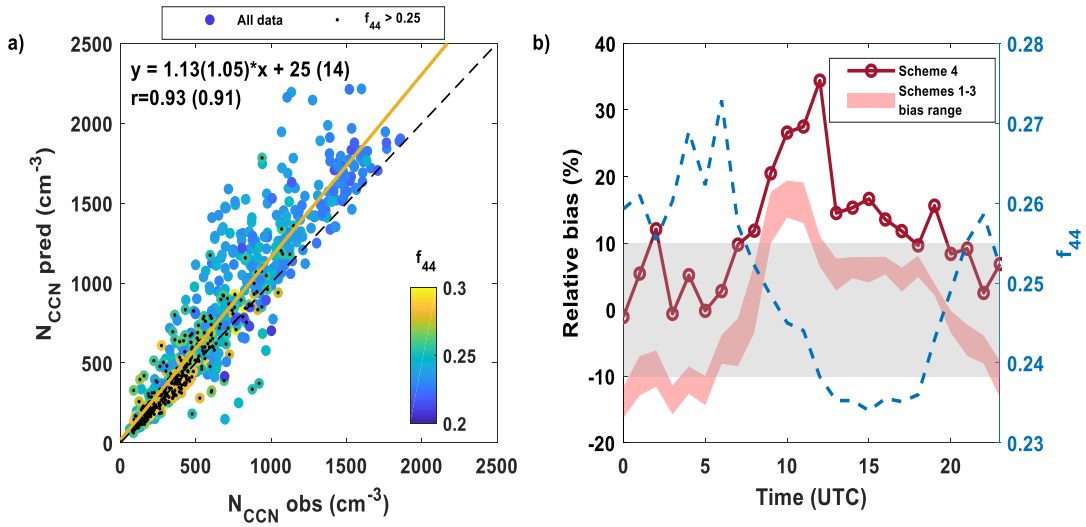

Figure 7-8. a) Scatter plot of predicted CCN concentrations (N_{CCN} pred) as a function of observed CCN concentrations (N_{CCN} obs) using the OA scheme 4. Datapoints are colored-coded by the corresponding f_{44} value. Datapoints with f_{44}>0.25 are also represented as small black dots The black dash line represents the 1:1 line. The linear equation and Pearson correlation coefficient (r) is also included for all data and for filtered data in parenthesis. b) Median diurnal evolution of the relative bias at SS=0.4% of the OA scheme 4 (left Y axis) and f_{44} (right Y axis). The grey shaded area represents the ±10% relative bias. The red shaded area represents the obtained relative bias range for the other OA schemes shown in Figure 6b.

To sum up, the new κ_{OA} calculation using f_{44} parameterization shows good agreement between CCN calculations and observations during nighttime (bias ranging between 0-10% from 21:00 UTC to 6:00 UTC), however involves worse predictions during morning and midday hours at SNS. After checking that all OA schemes for calculate κ_{OA} lead to practically the same results showing the highest bias values under these aerosol conditions influenced by vertical upslope transport of particles and/or NPF events, we conclude that predicting N_{CCN} using a bulk κ_{chem} always lead to disagreement with observations under these conditions since aerosol population properties are modified in a way that are not captured by any OA scheme. Other studies have suggested that at those sites where aerosol properties and atmospheric conditions clearly change along the day, mixing state assumptions for the aerosol population, like externally mixed aerosol or even combination of aerosol

populations with different mixing state, should be considered (Kulkarni et al., 2023; Ren et al., 2018; Zhang et al., 2017) instead of a more complex κ_{OA} characterization.

7.3 Conclusions

In this chapter, it is analyzed the influence of κ_{OA} on CCN estimations from bulk chemical composition measurements using different OA schemes to describe the overall aerosol hygroscopicity. To this end, we investigated the physicochemical properties and CCN activity of the aerosol population at a high-altitude mountain site (SNS station) in the south-eastern Iberian Peninsula, where atmospheric conditions can allow cloud formation.

Our results show the important contribution of OA to the total PM_1 mass concentration at SNS station that represents up to the 70% of the PM_1. After applying PMF analysis, we have identified that more oxidized oxygenated organic aerosol (MO-OOA) is the main factor that controls both OA and total PM_1, representing the 59% and 41% of the total OA and PM_1 mass concentration, respectively. However, despite OA controls the mass concentrations during the whole day, a strong diurnal pattern of all the chemical compounds have been observed. In this sense, during nighttime hours, associated with free troposphere conditions, the aerosol population is mainly dominated by accumulation and aged Aitken mode particles that, together with predominant contribution of MO-OOA and inorganic species, suggest the presence of aged aerosol particles showing the highest values of hygroscopicity along the day. Then, during the morning (6:00-10:00 UTC) the aerosol population start to be affected by orographic buoyant upward flows of aerosol from the urban area due to mountain-valley breeze regime and ABL influence. The aerosol population becomes more complex with higher relative influence of LO-OOA and BC (more related to fresher Aitken mode particles) and involve a decrease in the overall hygroscopicity. The aerosol

population properties continued changing during midday hours (11:00-16:00 UTC, highest insolation hours), when all chemical species showed their maximum concentrations, and the particle concentration of the nucleation mode achieved its maximum. The highest relative increase respect to nighttime conditions during these hours was observed for the LO-OOA factor, mainly caused by SOA formation through photochemical reactions among other sources such as upslope transport.

By using the results of the PMF analysis, the influence of OA hygroscopicity on the estimation of CCN concentrations has been assessed by using different hygroscopicity schemes of OA. The observed CCN concentrations during the whole campaign and the CCN estimations from the chemical composition and PNSD of aerosol population for all OA schemes showed slopes and correlations coefficients in the range between 1.08-1.40 and 0.89-0.94, respectively. Estimating CCN concentrations without considering chemical composition information achieved better overall results than the OA schemes at SS=0.4%. Thus, considering a fixed threshold size for particle activation is powerful tool when the D_{crit} and its variability is around the assumed size, otherwise high deviations respect observations are achieved. Our results reveal that stablishing different OA schemes to compute the overall hygroscopicity leads to similar CCN predictions. During nighttime, when aerosol properties are dominated by MO-OOA and inorganics, the relative bias at SS=0.4% of each OA scheme was clearly lower (between -16% and -6%) respect to morning and midday conditions (from 0% to 20%), when aerosol population is affected by ABL influence conditions. We observed that the diurnal patterns of bias for all schemes are influenced by the OA properties changes along the day, such as LO-OOA/MO-OOA ratio, and the different OA scheme cannot represent well κ_{OA} variability.

Finally, we retrieved κ_{OA} in the supersaturated regime from κ_{CCN} at SS=0.4% to establish a parameterization based on the f_{44} parameter, related to the oxidation degree of OA. The new OA scheme show similar overall values for the closure slope (1.13)

and correlation coefficient (0.93) compared to the other OA schemes, only improving the results for f_{44}>0.25. During nighttime conditions (21:00 UTC to 6:00 UTC, when f_{44} showed high values) the CCN observations were satisfactorily estimated (within the relative bias range of ±10%). Thus, this OA scheme improves the results respect to the other schemes, since κ_{OA} changes due to different oxidation degree is well described. However, during the other aerosol conditions (morning at midday hours) the new OA scheme did not improve the previous results and provided even higher overestimations (up to 35% at 12:00 UTC). Therefore, other considerations must be considered beyond the κ_{OA} characterization under these conditions.

We attribute that the observed positive bias of all OA schemes is related to two main reasons. First, the ToF-ACSM provide information of a limited aerosol size range often dominated by accumulation particles which is more affected by inorganic species and, therefore, the real κ_{chem} of the whole aerosol population might be overestimated by κ_{chem} measured with the ToF-ACSM. In addition, we must consider the effect of the well-known differences in the size ranges considered between the different instruments in this field campaign (ToF-ACSM, 70-700 nm; SMPS, 10-500 nm and CCNc, none size cutoff). Second, when the aerosol population consists of a complex mixture of particles, which at SNS can be observed during ABL influence conditions, the underlying assumptions for estimating CCN predictions based on internally mixed aerosol particles can introduce an intrinsic bias and κ_{OA} assumptions get a secondary role. These facts should be considered to have a more accurately representation of CCN concentrations worldwide when using bulk chemical composition measurements.

8 General conclusions and perspectives

This chapter contains the general conclusions obtained in the framework of this thesis dissertation that are based on the conclusions presented at the end of each of the results chapters. In particular, along this thesis, the research is focused on the activation properties of aerosol particles as CCN, potential aerosol sources and processes affecting the CCN concentration and the predictive capability of different empirical models to estimate CCN concentrations using ancillary aerosol properties. These topics have been investigated at two completely different environments (urban and high-altitude remote sites), but that are related due to their proximity and the influence that one exerts on the other.

Results show that both environment present very distinct characteristics in terms of aerosol properties and activation capacity as CCN. At the urban environment the activation properties are driven by anthropogenic primary sources, especially traffic emissions, while at the mountain site vertical transport due to upslope wind and secondary processes are the dominant factors. This is evident from the diurnal evolution of aerosol properties and activation parameters at both sites. While at Granada the diurnal pattern of N_{tot} and BC shows two clear maxima associated with traffic rush hours, at Sierra Nevada the maximum concentration is observed at midday. CCN concentrations have a similar diurnal pattern, while AF and kappa show the opposite pattern with two minima in Granada and one minimum in Sierra Nevada at midday.

It has been shown that at medium supersaturation (SS=0.5%), no more than 25% of urban aerosol particles can be activated on average due to the predominant small size (mean D_{geo} of 45 nm) and low hygroscopic nature, mean value of κ at

SS=0.5% varying between 0.08-0.15 depending on the season, while at the mountain environment the AF was higher (AF=0.47 on average). High CCN concentration are observed in Granada (N_{CCN} mean values around 2000-2500 at SS=0.5% depending on the season) as occur at other urban sites around the world, due to the high particle concentration, while remote environments show much lower concentrations (N_{CCN} mean values of 820 cm^{-3} at SS=0.5%).

Due to the large influence that urban emissions exert on the aerosol population observed in Sierra Nevada, the main aerosol population types were identified at the urban site using a clustering model for the PNSD data during warm period, from April to October. The identified aerosol population types are related to background conditions (associated with nighttime hours), traffic emissions (fresh and aged traffic particles) and NPF events influence (both freshly nucleated and grown particles). Aerosol populations associated with NPF events, separated in nucleation and growth categories, do not show a high contribution to the CCN concentration due to the small aerosol size of particles originated by NFP events at this site. On the other hand, traffic emissions have a limited contribution to CCN concentration, but can be an important CCN source when the freshly emitted particles suffer ageing (increasing their size and hygroscopicity) along the subsequent hours. The highest N_{CCN} values are observed during aged traffic conditions (mean value of 4000 cm^{-3} at SS=0.5%). Thus, aged traffic particles, that are present in high number concentration of CCN-active particles, could be transported to other remote environments modifying the aerosol population and its activation properties.

At the mountain station, the absence of local anthropogenic sources causes a clear reduction of approximately one order of magnitude in N_{tot} and BC concentrations compared to the urban site, showing a higher influence of larger particles. The chemical composition of the aerosol population is dominated by OA, which represents 70% of the PM_1, and according to the OA PMF analysis it is fairly

oxidized with contribution of LO-OOA and MO-OOA factors of 36% and 59%, respectively, to the total OA. During summer conditions the aerosol properties at this site show a clear diurnal pattern influenced by i) transported particles from Granada area due to ABL injections and orographic buoyant upward flow, and ii) the high frequency of NPF events. At nighttime when this site represents free tropospheric conditions, the aerosol population is dominated by accumulation mode particles and MO-OOA, revealing the aged nature of particles. During morning hours, there is an increase in Aitken and accumulation modes particles. This increase is accompanied by an increase in most chemical constituents, especially LO-OOA that shows the largest increase compared with night-time hours, due to SOA formation through photochemical oxidation during NPF events. Overall, although N_{CCN} (mean value of 820 cm^{-3} at SS=0.5%) is much lower compared to the urban site, the aerosol population is more hygroscopic, with mean κ value at SS=0.5% is 0.22 compared with 0.08 in Granada, which can be related to the high oxidation degree observed in Sierra Nevada. The minimum values of AF and κ are observed at midday hours due to the high concentration of nucleation particles and LO-OOA species, although this occurs in coincidence with the maximum CCN concentrations. NPF events are demonstrated to be an important source of CCN at the mountain site, with an estimated increase of 175% at SS=0.5% of CCN concentrations during NPF days compared to non-NPF days.

Finally, different empirical models to predict CCN concentrations based on ancillary aerosol properties have been tested at both locations. The simple empirical models based on parameterizing Twomey law fit coefficients using optical or physical properties (Chapter 5) show good agreement with observations at the urban site. However, at the mountain site those empirical models do not capture all the CCN variability and the CCN closures show a systematic underestimation of measurements and low correlation between measured and predicted CCN concentrations. Therefore, CCN coverage could be improve at urban environments by using these simple empirical

models based on some CCN proxy parameters (i.e., scattering coefficient and PNSD parameters), while at mountain sites these parameters are not sufficient to reproduce the measured CCN variability. Therefore, a different approach is necessary at mountain sites to estimate CCN concentrations. In this sense, a different approach to estimate CCN concentrations was conducted at Sierra Nevada using PNSD and bulk chemical composition measurements. Due to the dominance of OA at Sierra Nevada, the influence of OA hygroscopicity on CCN estimations was evaluated by assuming different OA schemes. Results reveal that CCN predictions for all OA schemes agree well with observation within a considerable error range and without noticeably differences between OA schemes. During nighttime hours, associated with free troposphere conditions, the OA scheme that includes the κ_{OA} variability led to more accurate predictions. However, during morning and midday hours, associated with ABL and NPF influenced conditions, detailed knowledge of OA sources and κ_{OA} are not sufficient to obtain reliable CCN predictions (overestimation up to 35%) and the underlying assumptions for estimating CCN concentrations based on internally mixed particles can introduce an intrinsic bias.

Further research will be essential to advance beyond the aspects addressed in this thesis, with a specific focus on certain topics:

- Performing CCN monodisperse measurements at both sites will provide the CCN size distribution allowing to distinguish the contribution of each aerosol mode to the CCN budget and infer some mixing state information of the activated particles. Therefore, the individual contribution of each of the sources and processes affecting the CCNs can be disclosed.
- An annual dataset of aerosol physicochemical properties and CCN activity at Sierra Nevada will allow to characterize their seasonal cycle and will provide useful information about differences between free-

troposphere and ABL influence conditions, with special emphasis on how OA components are affected at this site. Thus, a more comprehensive view on how the aerosol population and its activation properties are affected by transported particles from Granada and NPF events along the year would be obtained, as well as a better characterization of free tropospheric conditions.

- Evaluating the direct influence of NPF events on CCN, especially at Sierra Nevada, and how efficient is that influence depending on the origin of the NPF event, either biogenic or anthropogenic. To this end, characterizing the amount and types of VOCs and the bioaerosol fraction is needed.
- Performing in-cloud measurements will reveal the physicochemical properties of the cloud residuals which are the actual aerosol particles forming the cloud droplets. This will allow us to estimate the direct influence of natural and/or anthropogenic sources on clouds, as well as the ability of clouds to scavenge aerosol particles. Also, it can give direct information about the SS at which aerosol particles activate in the atmosphere.

Conclusiones generales y perspectivas

Este capítulo contiene las conclusiones generales obtenidas en el marco de esta tesis doctoral que se basan en las conclusiones presentadas al final de cada uno de los capítulos de resultados. En particular, a lo largo de esta tesis, la investigación se ha centrado en las propiedades de activación de las partículas del aerosol como CCN, las fuentes potenciales del aerosol, los procesos que afectan a la concentración de CCN y la capacidad predictiva de diferentes modelos empíricos para estimar las concentraciones de CCN utilizando propiedades auxiliares del aerosol. Estos temas se han investigado en dos entornos completamente diferentes: un emplazamiento urbano y otro remoto a gran altitud, pero que están relacionados debido a su proximidad y a la influencia que uno ejerce sobre el otro.

Los resultados muestran que ambos entornos presentan características muy distintas en cuanto a las propiedades del aerosol y su capacidad de activación como CCN. En el entorno urbano las propiedades de activación de las partículas están impulsadas por fuentes primarias antropogénicas, especialmente las emisiones del tráfico, mientras que en el emplazamiento de montaña el transporte vertical debido al viento ascendente y los procesos secundarios son los factores dominantes. Estas evidencias se obtienen a partir de la evolución diurna de las propiedades del aerosol y los parámetros de activación en ambos emplazamientos. Mientras que en Granada el patrón diurno de N_{tot} y BC muestra dos claros máximos asociados a las horas punta de tráfico, en Sierra Nevada la concentración máxima se observa a mediodía. Las concentraciones de CCN tienen un patrón diurno similar al de la concentración

de partículas, mientras que AF y κ muestran el patrón opuesto con dos mínimos en Granada y un mínimo en Sierra Nevada al mediodía.

Se ha demostrado que a una sobresaturación media (SS=0.5%), en valor medio no más del 25% de las partículas del aerosol urbano pueden ser activadas debido al pequeño tamaño predominante (D_{geo} promedio de 45 nm) y a la baja naturaleza higroscópica, con valor medio de κ a SS=0.5% entre 0.08-0.15, dependiendo de la época del año, mientras que en el entorno de montaña la AF fue mayor (AF=0.47 de valor medio). En Granada se observan altas concentraciones de CCN con valores medios de N_{CCN} en torno a 2000-2500 a SS=0.5%, dependiendo de la época del año, como ocurre en otros emplazamientos urbanos de todo el mundo, debido a la alta concentración de partículas, mientras que los entornos remotos muestran concentraciones mucho menores con valores medios de N_{CCN} de 820 cm^{-3} a SS=0.5%.

Debido a la gran influencia que las emisiones urbanas ejercen sobre la población de partículas del aerosol observada en Sierra Nevada, se identificaron los principales tipos de población de partículas en el emplazamiento urbano utilizando un modelo de agrupamiento o *clustering* para los datos de PNSD durante el periodo más cálido del año, de abril a octubre. Los tipos de población de partículas identificados están relacionados con las condiciones de fondo (asociadas a las horas nocturnas), las emisiones de tráfico (partículas de tráfico recién emitidas y envejecidas) y la influencia de eventos NPF (tanto partículas recién nucleadas como crecidas). Las poblaciones de partículas del aerosol asociadas a eventos NPF, separadas en categorías de nucleación y crecimiento, no muestran una contribución elevada a la concentración de CCN debido al pequeño tamaño de las partículas originadas por eventos NFP en este emplazamiento. Por otro lado, las emisiones de tráfico tienen una contribución limitada a la concentración de CCN, pero pueden ser una fuente importante de CCN cuando las partículas recién emitidas sufren

envejecimiento, aumentando su tamaño e higroscopicidad, a lo largo de las horas posteriores. Los valores más altos de CCN se observan en condiciones de tráfico envejecido (valor medio de 4000 cm^{-3} a SS=0.5%). Así, las partículas de tráfico envejecidas, que presentan una alta concentración numérica de partículas que se podrían activar como CCN, podrían ser transportadas a otros ambientes remotos modificando la población de partículas del aerosol y sus propiedades de activación.

En la estación de montaña, la ausencia de fuentes antropogénicas locales provoca una clara reducción de aproximadamente un orden de magnitud en las concentraciones de N_{tot} y BC, en comparación con el emplazamiento urbano, lo que muestra una mayor influencia de las partículas de mayor tamaño. La composición química de la población de partículas del aerosol está dominada por OA, que representa el 70% del PM_1, y según el análisis PMF dicho OA está bastante oxidado con una contribución de los factores LO-OOA y MO-OOA del 36% y 59%, respectivamente, respecto al total del OA. En condiciones estivales las propiedades del aerosol en este emplazamiento muestran un claro patrón diurno influenciado por i) partículas transportadas desde la zona de Granada debido a las inyecciones de aire de la ABL y al flujo ascendente orográfico, y ii) la alta frecuencia de eventos NPF. Durante la noche, cuando este emplazamiento presenta condiciones de troposfera libre, la población de partículas está dominada por partículas del modo de acumulación y MO-OOA, lo que revela la naturaleza envejecida de las partículas. Durante las horas de la mañana, se produce un aumento de las partículas de los modos Aitken y acumulación. Este aumento va acompañado de un incremento en la mayoría de los compuestos químicos, especialmente LO-OOA que muestra el mayor aumento en comparación con las horas nocturnas, debido a la formación de SOA a través de la oxidación fotoquímica durante los eventos NPF. En general, aunque N_{CCN}, cuyo valor medio es de 820 cm^{-3} a SS=0.5%, es mucho menor comparado con el valor que tiene en el emplazamiento urbano, la población de partículas es más higroscópica (valor medio de κ a SS=0.5% de 0.22, comparado con 0.08 en

Granada) lo que puede estar relacionado con el alto grado de oxidación de las partículas observadas en Sierra Nevada. Los valores mínimos de AF y κ se observan en las horas del mediodía debido a la alta concentración de partículas de nucleación y especies LO-OOA, aunque esto ocurre en coincidencia con las concentraciones máximas de CCN. Se ha demostrado que los eventos NPF son una fuente importante de CCN en el emplazamiento de montaña, con un aumento estimado del 175% a SS=0.5% de las concentraciones de CCN durante los días de NPF en comparación con los días de no NPF.

Por último, se han estudiado en ambos emplazamientos diferentes modelos empíricos para predecir las concentraciones de CCN basados en propiedades auxiliares del aerosol. Los modelos empíricos simples basados en la parametrización de los coeficientes de ajuste de la ley de Twomey, utilizando propiedades ópticas o físicas (Capítulo 5), muestran un buen acuerdo con las observaciones en el emplazamiento urbano. Sin embargo, en el emplazamiento de montaña esos modelos empíricos no explican toda la variabilidad de los CCN, y los correspondientes cierres de la concentración de CCN muestran una subestimación sistemática de las medidas y una baja correlación entre las concentraciones de CCN medidas y modeladas. Por lo tanto, la cobertura de datos de CCN podría mejorarse en entornos urbanos utilizando estos modelos empíricos simples basados en algunos parámetros predictores, como el coeficiente de dispersión o parámetros de la PNSD, mientras que en los emplazamientos de montaña estos parámetros no son suficientes para reproducir la variabilidad observada de los CCN. Por lo tanto, es necesario un enfoque diferente en los lugares de montaña para estimar las concentraciones de CCN. En este sentido, se ha llevado a cabo un enfoque diferente para estimar las concentraciones de CCN en Sierra Nevada utilizando datos de PNSD y medidas de composición química. Debido al predominio del OA en Sierra Nevada, se evaluó la influencia de la higroscopicidad del OA en las estimaciones de CCN suponiendo diferentes esquemas de OA. Los resultados revelan que las predicciones de CCN

para todos los esquemas de OA concuerdan bien con la observación dentro de un rango de error aceptable y sin diferencias notables entre los esquemas de OA. Durante las horas nocturnas, asociadas a condiciones de troposfera libre, el esquema de OA que incluye la variabilidad de κ_{OA} condujo a mejores resultados. Sin embargo, durante las horas de la mañana y el mediodía, asociadas a condiciones de influencia de ABL y eventos NPF, el conocimiento detallado de las fuentes de OA y κ_{OA} no son suficientes para obtener resultados fiables de CCN (sobreestimaciones de hasta el 35%), y las hipótesis subyacentes para estimar las concentraciones de CCN basadas en partículas mezcladas internamente pueden introducir un sesgo intrínseco.

Es importante seguir trabajando para avanzar más allá de los aspectos tratados en esta tesis. Por ejemplo, los estudios podrían centrarse específicamente en:

- La realización de medidas de la distribución de tamaños de CCN en ambos emplazamientos permitirá distinguir la contribución de cada modo del aerosol a la concentración total de CCN, e inferir información sobre el estado de mezcla de las partículas activadas. De este modo podríamos acercarnos a estimar la contribución individual de cada una de las fuentes y procesos que afectan a los CCN en ambos entornos.
- Una base de datos anual de las propiedades fisicoquímicas del aerosol y sus propiedades de activación como CCN en Sierra Nevada permitirá caracterizar su ciclo estacional y proporcionará información útil sobre las diferencias entre las condiciones de influencia de la troposfera libre y de la ABL, con especial énfasis en cómo se ven afectados los componentes del OA en este emplazamiento. Así, se podría obtener una visión más completa de cómo la población del aerosol y sus propiedades de activación se ven afectadas por las partículas transportadas desde

Granada y los eventos NPF a lo largo del año, así como una mejor caracterización de las condiciones de troposfera libre.

- Evaluar la influencia directa de los eventos NPF sobre la concentración de CCN, especialmente en Sierra Nevada, y cómo de eficiente es esa influencia dependiendo del origen del evento NPF, ya sea biogénico o antropogénico. Para ello sería necesario caracterizar la cantidad y tipos de compuestos orgánicos volátiles y la fracción de partículas de bioaerosol.
- La realización de medidas dentro de nubes podrá revelar las propiedades fisicoquímicas de las partículas que forman parte de la nube. Esto permitiría estimar la influencia directa de las fuentes naturales o antropogénicos en la formación de nubes. Además, se podría obtener información directa sobre la SS a la que las partículas del aerosol se activan en la atmósfera.

Appendix

Supplementary figures

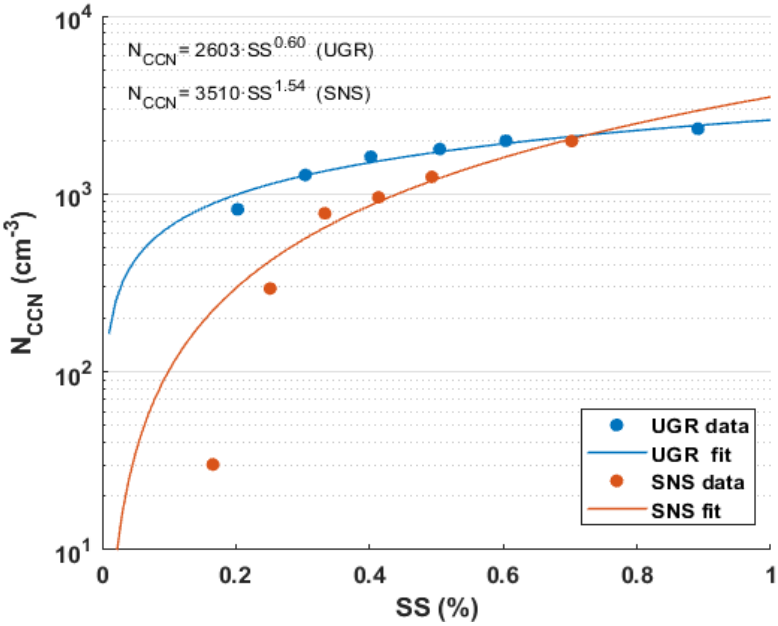

Figure S0-1. CCN spectra during a complete SS cycle at both stations and the corresponding fit according to Twomey power law. Each spectrum corresponds with a SS cycle: the UGR spectra is from 23-03-2019 at 12:00 and the SNS spectra from 02-06-2019 at 12:00.

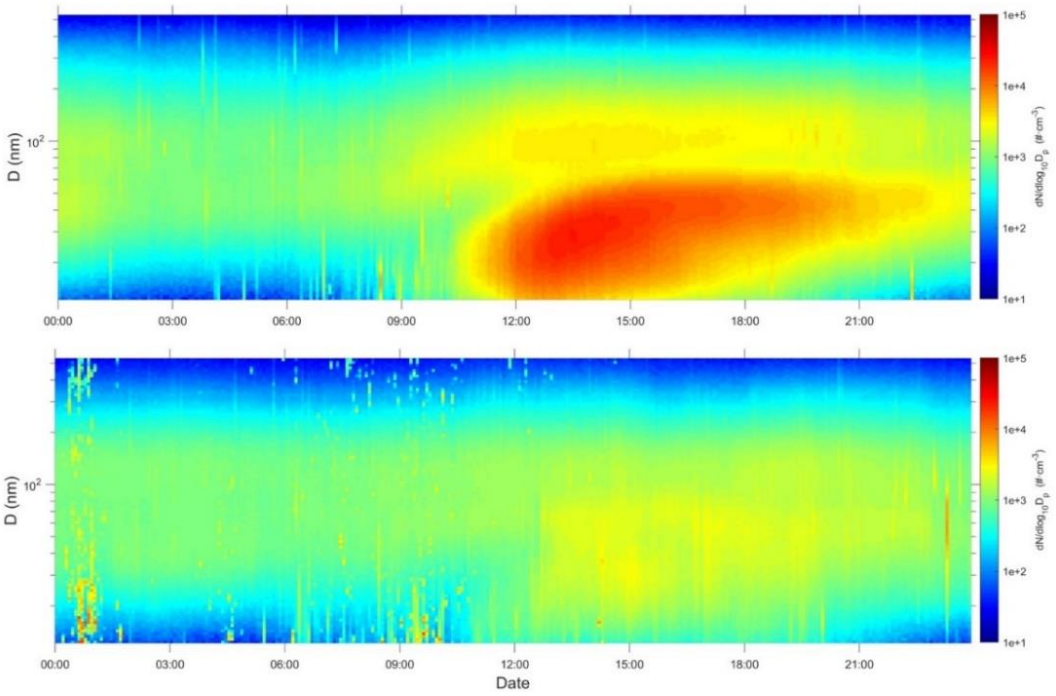

Figure S0-2. Aerosol size distribution during NPF event days (upper panel) and non-event days (lower panel).

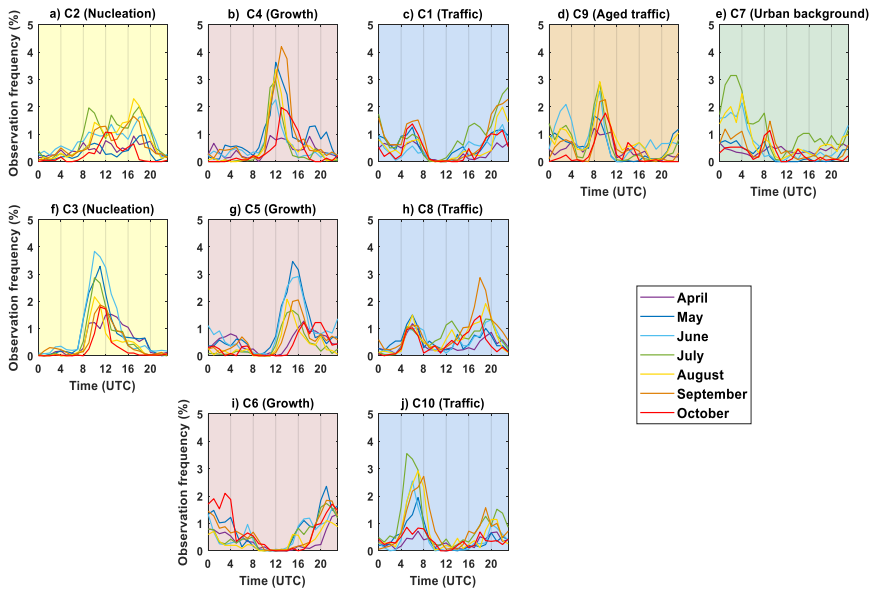

Figure S0-3. Diurnal evolution of the observed frequency of each cluster (C1-10) along all months during the measurement period.

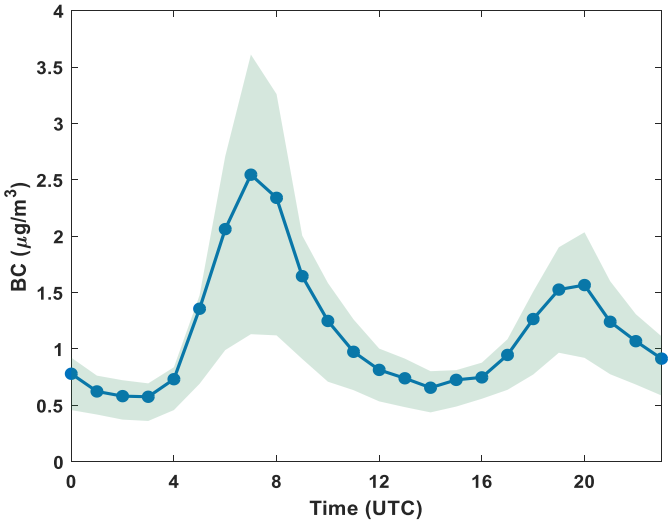

Figure S0-4. Mean diurnal of the equivalent black carbon mass concentration (BC) during the whole campaign. The shaded area represents the interquartile distance (percentiles 25th-75th).

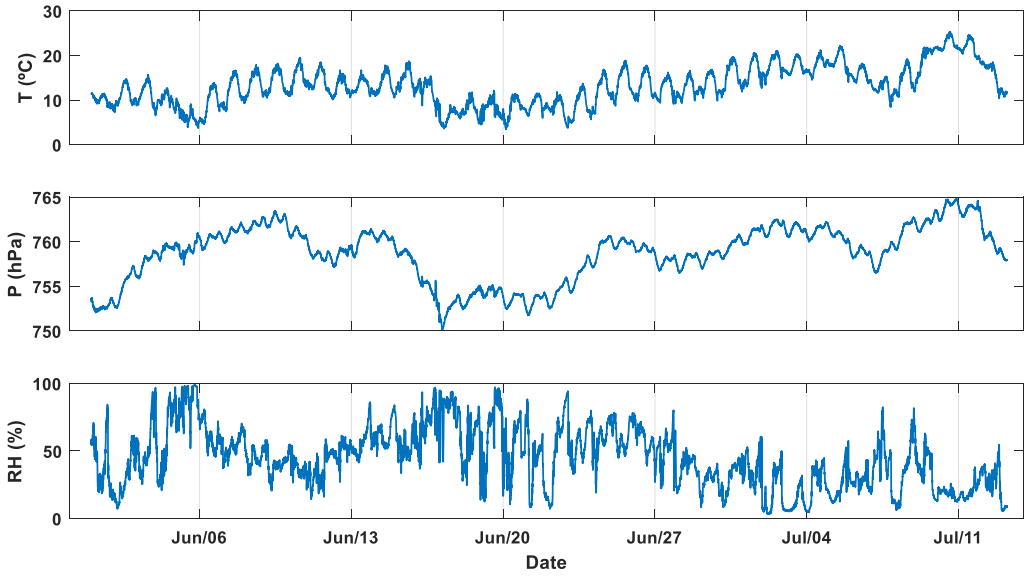

Figure S0-5. Time-series of temperature (T), pressure (P) and relative humidity (RH) along the campaign.

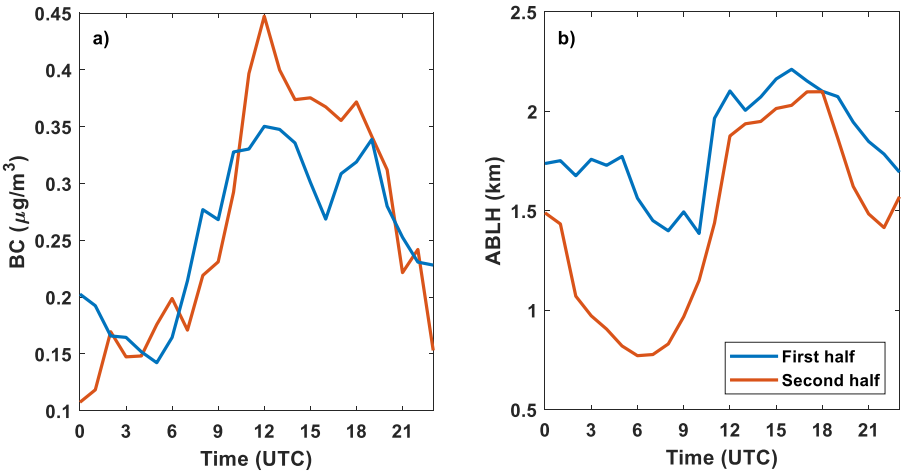

Figure S0-6. Diurnal evolution of a) BC mass concentration and b) ABL height during the first and second half of the campaign.

*The ABLH is determined using ceilometer measurements using the gradient method. The gradient method is presented in Moreira et al. (2020) and consists in detecting the minimum of gradient in the range corrected signal profile.

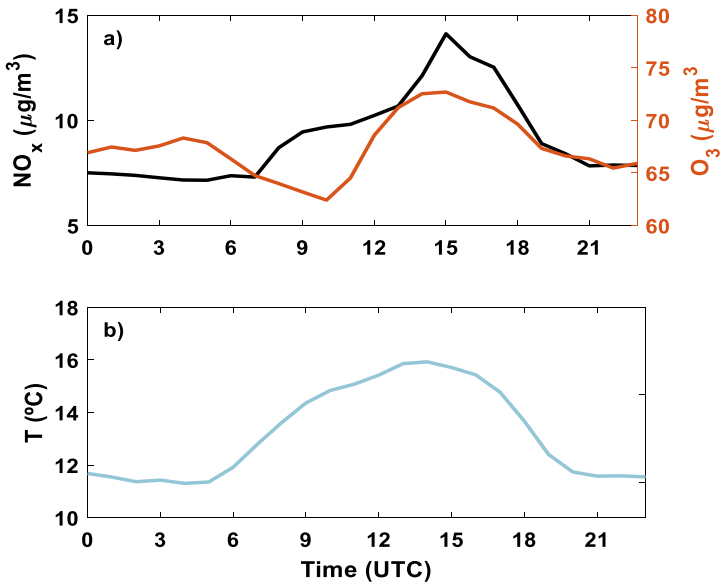

Figure S0-7. Mean diurnal evolution of a) NOx (left Y axis) and O3 concentration (right Y axis) and b) temperature along the campaign.

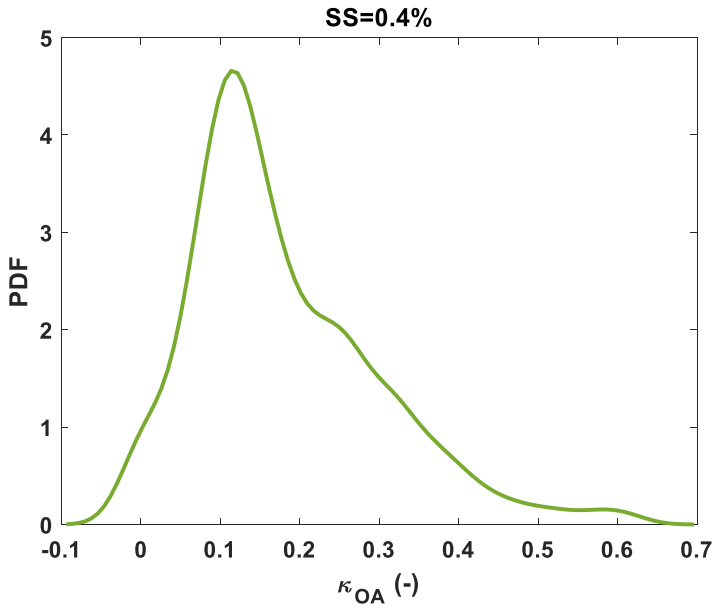

Figure S0-8. Probability density function (PDF) plot of κ_{OA} at SS=0.4%.

Supplementary tables

Table S0-1. Summary of mean activation parameters for each measurement location. For all studies listed, κ is derived from CCN measurements. In addition, relevant information about the campaign is listed in the table.

Site Location	Period	SS (%)	N_{CCN} (cm^{-3})	AF (-)	D_{crit}(nm)	κ (-)	Diameter range	Reference
Urban								
Vienna, Austria	interannual	0.50	820	0.13	162	-	13-929	Burkart et al. (2011)
Hong Kong, China	spring	0.50	1815	0.57	56	0.31	7-300	Meng et al. (2014)
Paris, France	winter	0.50	2248	-	76	0.11	10-413	Juranyi et al. (2013)
Granada, Spain	winter/spring	0.50	2500	0.21	91	0.08	10-500	This study
KORUS-AQ, South Korea	spring	0.60	3373	0.31	-	0.22	>10	Kim et al. (2018)
Seoul, South Korea	interannual	0.60	5323	0.30	-	-	10-414	Kim et al. (2014)
Beijing, China	summer	0.46					3-800	Gunthe et al. (2011)
aged pollution			8830	0.74	59	0.31		
fresh pollution			4980	0.25	74	0.18		
Rural/Remote								
Princess Elisabeth station, Antarctica	summer	0.50	177	0.51	-	-	>3	Herenz et al. (2019)
Amazon Basin, Brazil	annual	0.47	883	0.74	77	0.13	10-450	Pöhlker et al. (2016)
Noto Peninsula, Japan	autumn	0.52	-	-	60	0.24	-	Iwamoto et al. (2016)
Cape Fuguei, Taiwan	spring	0.54	1689	0.59	54	0.22	13-736	Cheung et al. (2020)
Finokalia, Crete	summer	0.51	2003	0.80	-	0.34	20-460	Bougiatioti et al. (2011)
Yangtze river delta, China	annual	0.45	6271	0.62	62	0.28	20-300	Che et al. (2017)
Mountain								
Jungfraujoch, Switzerland	summer	0.57	313	0.53	68	0.17	16-570	Juranyi et al. (2011)
Sierra Nevada, Spain	summer	0.50	820	0.47	66	0.22	10-500	This study
Puy de Dôme, France	summer	0.51	200-2000	-	65	0.22	10-400	Asmi et al. (2012)

Table S0-2. Statistical overview of particle concentration of different aerosol modes and the activation properties at SS=0.2, 0.4, 0.6%. The mean, median, standard deviation, percentile 25th (μ_{25}) and percentile 75th (μ_{75}) are presented.

Parameter		Mean	Median	STD	μ_{25}	μ_{75}
N_{tot} (cm^{-3})		2409	1488	2370	636	3358
N_{nucl} (cm^{-3})		768	282	1192	113	831
N_{Ait} (cm^{-3})		1215	767	1139	326	1801
N_{acc} (cm^{-3})		454	359	368	163	670
N_{CCN} (cm^{-3})	0.20%	321	276	216	145	465
	0.40%	638	563	423	282	913
	0.60%	813	713	531	359	1160
D_{crit} (nm)	0.20%	111	109	21	95	126
	0.40%	72	74	18	60	82
	0.60%	58	60	16	46	66
κ (-)	0.20%	0.22	0.18	0.12	0.13	0.25
	0.40%	0.22	0.15	0.17	0.11	0.25
	0.60%	0.20	0.13	0.19	0.09	0.24

Quick finder

List of symbols and acronyms

a.s.l.	Above Sea Level
AF	Activation Fraction
σ_{ap}	Aerosol absorption coefficient
σ_{bsp}	Aerosol back-scattering coefficient
AMS	Aerosol Mass Spectrometer
σ_{sp}	Aerosol Scattering Coefficient
ACTRIS	Aerosol, Clouds and Trace gases Infrastructure network
ACI	Aerosol-Cloud Interactions
ARI	Aerosol-Radiation Interactions
AE 33	Aethalometer Model 33
AGORA	Andalusian Global Observatory of the Atmosphere
IISTA	Andalusian Institute for Earth System Research
ABL	Atmospheric Boundary Layer
ABLH	Atmospheric Boundary Layer Height
GFAT	Atmospheric Physics Group
BSF	Back-Scatter Fraction
BC	Black Carbon

κ_{CCN}	CCN-derived Hygroscopicity Parameter
κ_{chem}	Chemical-derived Hygroscopicity Parameter
CCN	Cloud Condensation Nuclei
CCNc	Cloud Condensation Nuclei Counter
N_{CCN}	Cloud Condensation Nuclei number concentration
CPC	Condensation Particle Counter
D_{crit}	Critical Diameter
S_{crit}	Critical Saturation ratio
SS_{crit}	Critical Supersaturation ratio
DB	Davies-Bouldin index
R^2	Determination coefficient
DMA	Differential Mobility Analyzer
D_{dry}	Dry Diameter
EC	Elemental Carbon
S_{eq}	Equilibrium Saturation ratio
D_p	Equivalent Particle Diameter
D_{geo}	Geometric Diameter
UGR	Granada urban station
GR	Growth Rate
HTDMA	Humidity Tandem Differential Mobility Analyzer
HOA	Hydrocarbon-like Organic Aerosol
κ	Hygroscopicity Parameter
κ_{OA}	Hygroscopicity Parameter of Organic Aerosol
IA	Inorganic Aerosol
IPCC	Intergovernmental Panel on Climate Change

IE	Ionization Efficiency
LCL	Lifting Condensation Level
LO-OOA	Low-Oxidized Oxygenated Organic Aerosol
m/z	Mass-to-charge ratio
MO-OOA	More-Oxidized Oxygenated Organic Aerosol
MAAP	Multi-Angle Absorption Photometer
NOAA	National Oceanic and Atmospheric Administration
NPF	New Particle Formation
NFAN	NOAA Federated Aerosol Network
OPC	Optical Particle Counter
OA	Organic Aerosol
N	Particle number concentration
N_{xx}	Particle number concentration with diameters larger than XX nm
PNSD	Particle Number Size Distribution
r	Pearson correlation coefficient
PMF	Positive Matrix Factorization
POA	Primary Organic Aerosol
PDF	Probability Density Function
Q-ACSM	Quadrupole-Aerosol Chemical Speciation Monitor
RH	Relative humidity
RIE	Relative Ionization Efficiency
S	Saturation ratio
$P^0_{H_2O}$	Saturation water vapor pressure
SMPS	Scanning Mobility Particle Sizer
SAE	Scattering Ångström Exponent

SOA	Secondary Organic Aerosol
SNS	Sierra Nevada high-altitude remote station
SSA	Single Scattering Albedo
STD	Standard Deviation
SS	Supersaturation ratio
ToF-ACSM	Time of Flight-Aerosol Chemical Speciation Monitor
N_{tot}, N_{CN}	Total Particle number concentration
UFP	Ultrafine Particles
UTC	Universal Time Coordinated
VOCs	Volatile Organic Compounds
a_w	Water activity
P_{H_2O}	Water vapor pressure
λ	Wavelength

List of figures

List of tables

References

Agudelo-Castañeda, D. M., Teixeira, E. C., Braga, M., Rolim, S. B. A., Silva, L. F. O., Beddows, D. C. S., Harrison, R. M. and Querol, X.: Cluster analysis of urban ultrafine particles size distributions, Atmos. Pollut. Res., 10(1), 45–52, doi:10.1016/J.APR.2018.06.006, 2019.

del Águila, A., Sorribas, M., Lyamani, H., Titos, G., Olmo, F. J., Arruda-Moreira, G., Yela, M. and Alados-Arboledas, L.: Sources and physicochemical characteristics of submicron aerosols during three intensive campaigns in Granada (Spain), Atmos. Res., 213, 398–410, doi:10.1016/j.atmosres.2018.06.004, 2018.

Anderson, T. L. and Ogren, J. A.: Determining Aerosol Radiative Properties Using the TSI 3563 Integrating Nephelometer, Aerosol Sci. Technol., 29(1), 57–69, doi:10.1080/02786829808965551, 1998.

Andreae, M. O. and Rosenfeld, D.: Aerosol–cloud–precipitation interactions. Part 1. The nature and sources of cloud-active aerosols, Earth-Science Rev., 89(1–2), 13–41, doi:10.1016/j.earscirev.2008.03.001, 2008.

Andrews, E., Sheridan, P. J. P. J., Ogren, J. A. J. A., Hageman, D., Jefferson, A., Wendell, J., Alástuey, A., Alados-Arboledas, L., Bergin, M., Ealo, M., Sorribas, M., Sun, J., Gannet Hallar, A., Hoffer, A., Kalapov, I., Keywood, M., Kim, J., Kim, S. W., Kolonjari, F., Labuschagne, C., Lin, N. H., Macdonald, A., Mayol-Bracero, O. L., McCubbin, I. B., Pandolfi, M., Reisen, F., Sharma, S., Sherman, J. P., Sorribas, M. and Sun, J.: Overview of the NOAA/ESRL federated aerosol network, Bull. Am. Meteorol. Soc., 100(1), 123–135, doi:10.1175/BAMS-D-17-0175.1, 2019.

Arbelaitz, O., Gurrutxaga, I., Muguerza, J., Pérez, J. M. and Perona, I.: An extensive comparative study of cluster validity indices, Pattern Recognit., 46(1), 243–256, doi:10.1016/j.patcog.2012.07.021, 2013.

De Arruda Moreira, G., Guerrero-Rascado, J. L., Benavent-Oltra, J. A., Ortiz-Amezcua, P., Román, R., Bedoya-Velásquez, A. E., Bravo-Aranda, J. A., Reyes, F. J. O., Landulfo, E. and Alados-

Arboledas, L.: Analyzing the turbulent planetary boundary layer by remote sensing systems: The Doppler wind lidar, aerosol elastic lidar and microwave radiometer, Atmos. Chem. Phys., 19(2), 1263–1280, doi:10.5194/acp-19-1263-2019, 2019.

Asmi, A., Wiedensohler, A., Laj, P., Fjaeraa, A.-M., Sellegri, K., Birmili, W., Weingartner, E., Baltensperger, U., Zdimal, V., Zikova, N., Putaud, J.-P., Marinoni, A., Tunved, P., Hansson, H.-C., Fiebig, M., Kivekäs, N., Lihavainen, H., Asmi, E., Ulevicius, V., Aalto, P. P., Swietlicki, E., Kristensson, A., Mihalopoulos, N., Kalivitis, N., Kalapov, I., Kiss, G., de Leeuw, G., Henzing, B., Harrison, R. M., Beddows, D., O'Dowd, C., Jennings, S. G., Flentje, H., Weinhold, K., Meinhardt, F., Ries, L. and Kulmala, M.: Number size distributions and seasonality of submicron particles in Europe 2008–2009, Atmos. Chem. Phys., 11(11), 5505–5538, doi:10.5194/acp-11-5505-2011, 2011.

Asmi, E., Freney, E., Hervo, M., Picard, D., Rose, C., Colomb, A. and Sellegri, K.: Aerosol cloud activation in summer and winter at puy-de-Dôme high altitude site in France, Atmos. Chem. Phys., 12(23), 11589–11607, doi:10.5194/acp-12-11589-2012, 2012.

Atwood, S. A., Kreidenweis, S. M., DeMott, P. J., Petters, M. D., Cornwell, G. C., Martin, A. C. and Moore, K. A.: Classification of aerosol population type and cloud condensation nuclei properties in a coastal California littoral environment using an unsupervised cluster model, Atmos. Chem. Phys., 19(10), 6931–6947, doi:10.5194/acp-19-6931-2019, 2019.

Ball, G. H. and Hall, D. J.: ISODATA, A NOVEL METHOD OF DATA ANALYSIS AND PATTERN CLASSIFICATION., 1965.

Baron, P. A. and Willeke, K.: Aerosol fundamentals, Aerosol Meas. Princ. Tech. Appl., 2, 2001.

Beddows, D. C. S., Dall'Osto, M. and Harrison, R. M.: Cluster Analysis of Rural, Urban, and Curbside Atmospheric Particle Size Data, Environ. Sci. Technol., 43(13), 4694–4700, doi:10.1021/es803121t, 2009.

Bedoya-Velásquez, A. E., Navas-Guzmán, F., Granados-Muñoz, M. J., Titos, G., Román, R., Casquero-Vera, J. A., Ortiz-Amezcua, P., Benavent-Oltra, J. A., de Arruda Moreira, G., Montilla-Rosero, E., Hoyos, C. D., Artiñano, B., Coz, E., Olmo-Reyes, F. J., Alados-Arboledas, L. and Guerrero-Rascado, J. L.: Hygroscopic growth study in the framework of EARLINET during the SLOPE I campaign: synergy of remote sensing and in situ instrumentation, Atmos. Chem. Phys.,

18(10), 7001–7017, doi:10.5194/acp-18-7001-2018, 2018.

Birmili, W., Ries, L., Sohmer, R., Anastou, A., Sonntag, A., König, K. and Levin, I.: Fine and ultrafine aerosol particles at the GAW station Schneefernerhaus/Zugspitze | Feine und ultrafeine aerosolpartikeln an der GAW-station Schneefernerhaus/Zugspitze, Gefahrstoffe Reinhaltung der Luft, 69(1–2), 31–35, 2009.

Bougiatioti, A., Fountoukis, C., Kalivitis, N., Pandis, S. N., Nenes, A. and Mihalopoulos, N.: Cloud condensation nuclei measurements in the marine boundary layer of the eastern Mediterranean: CCN closure and droplet growth kinetics, Atmos. Chem. Phys., 9(18), 7053–7066, doi:10.5194/acp-9-7053-2009, 2009.

Bougiatioti, A., Bezantakos, S., Stavroulas, I., Kalivitis, N., Kokkalis, P., Biskos, G., Mihalopoulos, N., Papayannis, A. and Nenes, A.: Biomass-burning impact on CCN number, hygroscopicity and cloud formation during summertime in the eastern Mediterranean, Atmos. Chem. Phys., 16(11), 7389–7409, doi:10.5194/acp-16-7389-2016, 2016.

Bougiatioti, A., Nenes, A., Lin, J. J., Brock, C. A., de Gouw, J. A., Liao, J., Middlebrook, A. M. and Welti, A.: Drivers of cloud droplet number variability in the summertime in the southeastern United States, Atmos. Chem. Phys., 20(20), 12163–12176, doi:10.5194/acp-20-12163-2020, 2020.

Brines, M., Dall'Osto, M., Beddows, D. C. S., Harrison, R. M. and Querol, X.: Simplifying aerosol size distributions modes simultaneously detected at four monitoring sites during SAPUSS, Atmos. Chem. Phys., 14(6), 2973–2986, doi:10.5194/acp-14-2973-2014, 2014.

Brines, M., Dall'Osto, M., Beddows, D. C. S., Harrison, R. M., Gómez-Moreno, F., Núñez, L., Artíñano, B., Costabile, F., Gobbi, G. P., Salimi, F., Morawska, L., Sioutas, C. and Querol, X.: Traffic and nucleation events as main sources of ultrafine particles in high-insolation developed world cities, Atmos. Chem. Phys., 15(10), 5929–5945, doi:10.5194/acp-15-5929-2015, 2015.

Brown, S. G., Lee, T., Norris, G. A., Roberts, P. T., Collett Jr., J. L., Paatero, P. and Worsnop, D. R.: Receptor modeling of near-roadway aerosol mass spectrometer data in Las Vegas, Nevada, with EPA PMF, Atmos. Chem. Phys., 12(1), 309–325, doi:10.5194/acp-12-309-2012, 2012.

Burgos, M. A., Andrews, E., Titos, G., Alados-Arboledas, L., Baltensperger, U., Day, D., Jefferson, A., Kalivitis, N., Mihalopoulos, N., Sherman, J., Weingartner, E. and Zieger, P.: A global view on the effect of water uptake on aerosol particle light scattering, Sci. data, 6(1), 157, doi:10.1038/s41597-019-0158-7, 2019.

Burkart, J., Steiner, G., Reischl, G. and Hitzenberger, R.: Long-term study of cloud condensation nuclei (CCN) activation of the atmospheric aerosol in Vienna, Atmos. Environ., doi:10.1016/j.atmosenv.2011.07.022, 2011.

Cai, M., Tan, H., Chan, C. K., Qin, Y., Xu, H., Li, F., Schurman, M. I., Liu, L. and Zhao, J.: The size-resolved cloud condensation nuclei (CCN) activity and its prediction based on aerosol hygroscopicity and composition in the Pearl Delta River (PRD) region during wintertime 2014, Atmos. Chem. Phys., 18(22), doi:10.5194/acp-18-16419-2018, 2018.

Cai, M., Liang, B., Sun, Q., Zhou, S., Chen, X., Yuan, B., Shao, M., Tan, H. and Zhao, J.: Effects of continental emissions on cloud condensation nuclei (CCN) activity in the northern South China Sea during summertime 2018, Atmos. Chem. Phys., 20(15), 9153–9167, doi:10.5194/acp-20-9153-2020, 2020.

Cai, M., Huang, S., Liang, B., Sun, Q., Liu, L., Yuan, B., Shao, M., Hu, W., Chen, W., Song, Q., Li, W., Peng, Y., Wang, Z., Chen, D., Tan, H., Xu, H., Li, F., Deng, X., Deng, T., Sun, J. and Zhao, J.: Measurement report: Distinct size dependence and diurnal variation in organic aerosol hygroscopicity, volatility, and cloud condensation nuclei activity at a rural site in the Pearl River Delta (PRD) region, China, Atmos. Chem. Phys., 22(12), 8117–8136, doi:10.5194/acp-22-8117-2022, 2022.

Canagaratna, M. R., Onasch, T. B., Wood, E. C., Herndon, S. C., Jayne, J. T., Cross, E. S., Miake-Lye, R. C., Kolb, C. E. and Worsnop, D. R.: Evolution of Vehicle Exhaust Particles in the Atmosphere, J. Air Waste Manage. Assoc., 60(10), 1192–1203, doi:10.3155/1047-3289.60.10.1192, 2010.

Canagaratna, M. R., Jimenez, J. L., Kroll, J. H., Chen, Q., Kessler, S. H., Massoli, P., Hildebrandt Ruiz, L., Fortner, E., Williams, L. R., Wilson, K. R., Surratt, J. D., Donahue, N. M., Jayne, J. T. and Worsnop, D. R.: Elemental ratio measurements of organic compounds using aerosol mass spectrometry: characterization, improved calibration, and implications, Atmos. Chem. Phys., 15(1), 253–272, doi:10.5194/acp-15-253-2015, 2015.

Canonaco, F., Crippa, M., Slowik, J. G., Baltensperger, U. and Prévôt, A. S. H.: SoFi, an IGOR-based interface for the efficient use of the generalized multilinear engine (ME-2) for the source apportionment: ME-2 application to aerosol mass spectrometer data, Atmos. Meas. Tech., 6(12), 3649–3661, doi:10.5194/amt-6-3649-2013, 2013.

Cappa, C. D., Che, D. L., Kessler, S. H., Kroll, J. H. and Wilson, K. R.: Variations in organic aerosol optical and hygroscopic properties upon heterogeneous OH oxidation, J. Geophys. Res. Atmos., 116(D15), doi:https://doi.org/10.1029/2011JD015918, 2011.

Casans, A., Rejano, F., Maldonado-Valderrama, J., Casquero-Vera, J. A., Ruiz-Peñuela, S., van Drooge, B. L., Lyamani, H., Cazorla, A., Andrews, E., Lin, J. J., Mirza-Montoro, F., Pérez-Ramírez, D., Olmo, F. J., Alados-Arboledas, L., Cariñanos, P. and Titos, G.: Cloud condensation nuclei activation properties of Mediterranean pollen types considering organic chemical composition and surface tension effects, Atmos. Environ., 119961, doi:https://doi.org/10.1016/j.atmosenv.2023.119961, 2023.

Casquero-Vera, J. A., Lyamani, H., Titos, G., Borrás, E., Olmo, F. J. and Alados-Arboledas, L.: Impact of primary NO2 emissions at different urban sites exceeding the European NO2 standard limit, Sci. Total Environ., doi:10.1016/j.scitotenv.2018.07.360, 2019.

Casquero-Vera, J. A., Lyamani, H., Dada, L., Hakala, S., Paasonen, P., Román, R., Fraile, R., Petäjä, T., Olmo-Reyes, F. J. and Alados-Arboledas, L.: New particle formation at urban and high-altitude remote sites in the south-eastern Iberian Peninsula, Atmos. Chem. Phys., 20(22), 14253–14271, doi:10.5194/acp-20-14253-2020, 2020.

Casquero-Vera, J. A., Lyamani, H., Titos, G., Minguillón, M. C., Dada, L., Alastuey, A., Querol, X., Petäjä, T., Olmo, F. J. and Alados-Arboledas, L.: Quantifying traffic, biomass burning and secondary source contributions to atmospheric particle number concentrations at urban and suburban sites, Sci. Total Environ., 768, doi:10.1016/j.scitotenv.2021.145282, 2021.

Cassee, F., Morawska, L., Peters, A., Wierzbicka, A., Buonanno, G., Cyrys, J., SchnelleKreis, J., Kowalski, M., Riediker, M., Birmili, W., Querol, X., Yildirim, A. Ö., Elder, A., Yu, I. J., Øvrevik, J., Hougaard, K. S., Loft, S., Schmid, O., Schwarze, P. E., Stöger, T., Schneider, A., Okokon, E., Samoli, E., Stafoggia, M., Pickford, R., Zhang, S., Breitner, S., Schikowski, T., Lanki, T. and Aurelio, T.: White Paper Ambient ultrafine particles evidence for policy makers, 2019.

Cerully, K. M., Bougiatioti, A., Hite Jr., J. R., Guo, H., Xu, L., Ng, N. L., Weber, R. and Nenes, A.: On the link between hygroscopicity, volatility, and oxidation state of ambient and water-soluble aerosols in the southeastern United States, Atmos. Chem. Phys., 15(15), 8679–8694, doi:10.5194/acp-15-8679-2015, 2015.

Chang, R. Y.-W., Slowik, J. G., Shantz, N. C., Vlasenko, A., Liggio, J., Sjostedt, S. J., Leaitch,

W. R. and Abbatt, J. P. D.: The hygroscopicity parameter (κ) of ambient organic aerosol at a field site subject to biogenic and anthropogenic influences: relationship to degree of aerosol oxidation, Atmos. Chem. Phys., 10(11), 5047–5064, doi:10.5194/acp-10-5047-2010, 2010.

Charron, A., Birmili, W. and Harrison, R. M.: Fingerprinting particle origins according to their size distribution at a UK rural site, J. Geophys. Res., 113(D7), D07202, doi:10.1029/2007JD008562, 2008.

Che, H. C., Zhang, X. Y., Wang, Y. Q., Zhang, L., Shen, X. J., Zhang, Y. M., Ma, Q. L., Sun, J. Y., Zhang, Y. W. and Wang, T. T.: Characterization and parameterization of aerosol cloud condensation nuclei activation under different pollution conditions, Sci. Rep., 6, doi:10.1038/srep24497, 2016.

Chen, J., Budisulistiorini, S. H., Itoh, M., Lee, W.-C., Miyakawa, T., Komazaki, Y., Yang, L. D. Q. and Kuwata, M.: Water uptake by fresh Indonesian peat burning particles is limited by water-soluble organic matter, Atmos. Chem. Phys., 17(18), 11591–11604, doi:10.5194/acp-17-11591-2017, 2017.

Chen, L., Li, Q., Wu, D., Sun, H., Wei, Y., Ding, X., Chen, H., Cheng, T. and Chen, J.: Size distribution and chemical composition of primary particles emitted during open biomass burning processes: Impacts on cloud condensation nuclei activation, Sci. Total Environ., 674, 179–188, doi:10.1016/j.scitotenv.2019.03.419, 2019.

Cheung, H. C., Chou, C. C.-K., Lee, C. S. L., Kuo, W.-C. and Chang, S.-C.: Hygroscopic properties and cloud condensation nuclei activity of atmospheric aerosols under the influences of Asian continental outflow and new particle formation at a coastal site in eastern Asia, Atmos. Chem. Phys., 20(10), 5911–5922, doi:10.5194/acp-20-5911-2020, 2020.

Collaud Coen, M., Weingartner, E., Nyeki, S., Cozic, J., Henning, S., Verheggen, B., Gehrig, R. and Baltensperger, U.: Long-term trend analysis of aerosol variables at the high-alpine site Jungfraujoch, J. Geophys. Res. Atmos., 112(13), doi:10.1029/2006JD007995, 2007.

Costabile, F., Birmili, W., Klose, S., Tuch, T., Wehner, B., Wiedensohler, A., Franck, U., König, K. and Sonntag, A.: Spatio-temporal variability and principal components of the particle number size distribution in an urban atmosphere, Atmos. Chem. Phys., 9(9), 3163–3195, doi:10.5194/acp-9-3163-2009, 2009.

Crippa, M., DeCarlo, P. F., Slowik, J. G., Mohr, C., Heringa, M. F., Chirico, R., Poulain, L.,

Freutel, F., Sciare, J., Cozic, J., Di Marco, C. F., Elsasser, M., Nicolas, J. B., Marchand, N., Abidi, E., Wiedensohler, A., Drewnick, F., Schneider, J., Borrmann, S., Nemitz, E., Zimmermann, R., Jaffrezo, J.-L., Prévôt, A. S. H. and Baltensperger, U.: Wintertime aerosol chemical composition and source apportionment of the organic fraction in the metropolitan area of Paris, Atmos. Chem. Phys., 13(2), 961–981, doi:10.5194/acp-13-961-2013, 2013.

Crosbie, E., Youn, J.-S., Balch, B., Wonaschütz, A., Shingler, T., Wang, Z., Conant, W. C., Betterton, E. A. and Sorooshian, A.: On the competition among aerosol number, size and composition in predicting CCN variability: a multi-annual field study in an urbanized desert, Atmos. Chem. Phys., 15(12), 6943–6958, doi:10.5194/acp-15-6943-2015, 2015.

Cubison, M. J., Ervens, B., Feingold, G., Docherty, K. S., Ulbrich, I. M., Shields, L., Prather, K., Hering, S. and Jimenez, J. L.: The influence of chemical composition and mixing state of Los Angeles urban aerosol on CCN number and cloud properties, Atmos. Chem. Phys., 8(18), 5649–5667, doi:10.5194/acp-8-5649-2008, 2008.

Dal Maso, M., Kulmala, M., Riipinen, I., Wagner, R., Hussein, T., Aalto, P. P. P. and Lehtinen, K. E. J. K. E. J.: Formation and growth of fresh atmospheric aerosols: Eight years of aerosol size distribution data from SMEAR II, Hyytiälä, Finland, Boreal Environ. Res., 10(5), 323–336, 2005.

Dall'Osto, M., Monahan, C., Greaney, R., Beddows, D. C. S., Harrison, R. M., Ceburnis, D. and O'Dowd, C. D.: A statistical analysis of North East Atlantic (submicron) aerosol size distributions, Atmos. Chem. Phys., 11(24), 12567–12578, doi:10.5194/acp-11-12567-2011, 2011.

Dameto de España, C., Wonaschütz, A., Steiner, G., Rosati, B., Demattio, A., Schuh, H. and Hitzenberger, R.: Long-term quantitative field study of New Particle Formation (NPF) events as a source of Cloud Condensation Nuclei (CCN) in the urban background of Vienna, Atmos. Environ., 164, 289–298, doi:10.1016/j.atmosenv.2017.06.001, 2017.

Davies, D. L. and Bouldin, D. W.: A Cluster Separation Measure, IEEE Trans. Pattern Anal. Mach. Intell., PAMI-1(2), 224–227, doi:10.1109/TPAMI.1979.4766909, 1979.

Deng, Y., Kagami, S., Ogawa, S., Kawana, K., Nakayama, T., Kubodera, R., Adachi, K., Hussein, T., Miyazaki, Y. and Mochida, M.: Hygroscopicity of Organic Aerosols and Their Contributions to CCN Concentrations Over a Midlatitude Forest in Japan, J. Geophys. Res. Atmos., 123(17), 9703–9723, doi:https://doi.org/10.1029/2017JD027292, 2018.

Deng, Y., Yai, H., Fujinari, H., Kawana, K., Nakayama, T. and Mochida, M.: Diurnal variation

and size dependence of the hygroscopicity of organic aerosol at a forest site in Wakayama, Japan: their relationship to CCN concentrations, Atmos. Chem. Phys., 19(9), 5889–5903, doi:10.5194/acp-19-5889-2019, 2019.

Drinovec, L., Močnik, G., Zotter, P., Prévôt, A. S. H., Ruckstuhl, C., Coz, E., Rupakheti, M., Sciare, J., Müller, T., Wiedensohler, A. and Hansen, A. D. A.: The "dual-spot" Aethalometer: an improved measurement of aerosol black carbon with real-time loading compensation, Atmos. Meas. Tech., 8(5), 1965–1979, doi:10.5194/amt-8-1965-2015, 2015.

Duan, J., Wang, Y., Xie, X., Li, M., Tao, J., Wu, Y., Cheng, T., Zhang, R., Liu, Y., Li, X., Gao, W., Wang, J., He, Q., Gao, W. and Wang, J.: Influence of pollutants on activity of aerosol cloud condensation nuclei (CCN) during pollution and post-rain periods in Guangzhou, southern China, Sci. Total Environ., 642, 1008–1019, doi:https://doi.org/10.1016/j.scitotenv.2018.06.053, 2018.

Duplissy, J., DeCarlo, P. F., Dommen, J., Alfarra, M. R., Metzger, A., Barmpadimos, I., Prevot, A. S. H., Weingartner, E., Tritscher, T., Gysel, M., Aiken, A. C., Jimenez, J. L., Canagaratna, M. R., Worsnop, D. R., Collins, D. R., Tomlinson, J. and Baltensperger, U.: Relating hygroscopicity and composition of organic aerosol particulate matter, Atmos. Chem. Phys., 11(3), 1155–1165, doi:10.5194/acp-11-1155-2011, 2011.

Dusek, U., Frank, G. P., Hildebrandt, L., Curtius, J., Schneider, J., Walter, S., Chand, D., Drewnick, F., Hings, S., Jung, D., Borrmann, S. and Andreae, M. O.: Size matters more than chemistry for cloud-nucleating ability of aerosol particles, Science (80-.)., 312(5778), 1375–1378, doi:10.1126/science.1125261, 2006.

Ervens, B., Cubison, M. J., Andrews, E., Feingold, G., Ogren, J. A., Jimenez, J. L., Quinn, P. K., Bates, T. S., Wang, J., Zhang, Q., Flynn, M. and Allan, J. D.: CCN predictions using simplified assumptions of organic aerosol composition and mixing state: A synthesis from six different locations, Atmos. Chem. Phys., 10(10), 4795–4807, doi:10.5194/acp-10-4795-2010, 2010.

Fanourgakis, G. S., Kanakidou, M., Nenes, A., Bauer, S. E., Bergman, T., Carslaw, K. S., Grini, A., Hamilton, D. S., Johnson, J. S., Karydis, V. A., Wu, M. and Yu, F.: Evaluation of global simulations of aerosol particle and cloud condensation nuclei number, with implications for cloud droplet formation, Atmos. Chem. Phys., 19(13), 8591–8617, doi:10.5194/acp-19-8591-2019, 2019.

Fröhlich, R., Cubison, M. J., Slowik, J. G., Bukowiecki, N., Prévôt, A. S. H., Baltensperger, U., Schneider, J., Kimmel, J. R., Gonin, M., Rohner, U., Worsnop, D. R. and Jayne, J. T.: The ToF-

ACSM: a portable aerosol chemical speciation monitor with TOFMS detection, Atmos. Meas. Tech., 6(11), 3225–3241, doi:10.5194/amt-6-3225-2013, 2013.

Fröhlich, R., Crenn, V., Setyan, A., Belis, C. A., Canonaco, F., Favez, O., Riffault, V., Slowik, J. G., Aas, W., Aijälä, M., Alastuey, A., Artiñano, B., Bonnaire, N., Bozzetti, C., Bressi, M., Carbone, C., Coz, E., Croteau, P. L., Cubison, M. J., Esser-Gietl, J. K., Green, D. C., Gros, V., Heikkinen, L., Herrmann, H., Jayne, J. T., Lunder, C. R., Minguillón, M. C., Močnik, G., O'Dowd, C. D., Ovadnevaite, J., Petralia, E., Poulain, L., Priestman, M., Ripoll, A., Sarda-Estève, R., Wiedensohler, A., Baltensperger, U., Sciare, J. and Prévôt, A. S. H.: ACTRIS ACSM intercomparison – Part 2: Intercomparison of ME-2 organic source apportionment results from 15 individual, co-located aerosol mass spectrometers, Atmos. Meas. Tech., 8(6), 2555–2576, doi:10.5194/amt-8-2555-2015, 2015.

Fuchs, N. A.: On the stationary charge distribution on aerosol particles in a bipolar ionic atmosphere, Geofis. Pura e Appl., 56(1), 185–193, doi:10.1007/BF01993343, 1963.

Gentner, D. R., Isaacman, G., Worton, D. R., Chan, A. W. H., Dallmann, T. R., Davis, L., Liu, S., Day, D. A., Russell, L. M., Wilson, K. R., Weber, R., Guha, A., Harley, R. A. and Goldstein, A. H.: Elucidating secondary organic aerosol from diesel and gasoline vehicles through detailed characterization of organic carbon emissions., Proc. Natl. Acad. Sci. U. S. A., 109(45), 18318–23, doi:10.1073/pnas.1212272109, 2012.

Georgakaki, P., Bougiatioti, A., Wieder, J., Mignani, C., Ramelli, F., Kanji, Z. A., Henneberger, J., Hervo, M., Berne, A., Lohmann, U. and Nenes, A.: On the drivers of droplet variability in alpine mixed-phase clouds, Atmos. Chem. Phys., 21(14), 10993–11012, doi:10.5194/acp-21-10993-2021, 2021.

Gong, X., Wex, H., Voigtländer, J., Fomba, K. W., Weinhold, K., van Pinxteren, M., Henning, S., Müller, T., Herrmann, H. and Stratmann, F.: Characterization of aerosol particles at Cabo Verde close to sea level and at the cloud level -- Part 1: Particle number size distribution, cloud~condensation nuclei and their origins, Atmos. Chem. Phys., 20(3), 1431–1449, doi:10.5194/acp-20-1431-2020, 2020.

Gong, X., Wex, H., Müller, T., Henning, S., Voigtländer, J., Wiedensohler, A. and Stratmann, F.: Understanding aerosol microphysical properties from 10 years of data collected at Cabo Verde based on an unsupervised machine learning classification, Atmos. Chem. Phys., 22(8), 5175–5194, doi:10.5194/acp-22-5175-2022, 2022.

Gordon, H., Kirkby, J., Baltensperger, U., Bianchi, F., Breitenlechner, M., Curtius, J., Dias, A., Dommen, J., Donahue, N. M., Dunne, E. M., Yan, C. and Carslaw, K. S.: Causes and importance of new particle formation in the present-day and preindustrial atmospheres, J. Geophys. Res. Atmos., 122(16), 8739–8760, doi:10.1002/2017JD026844, 2017.

Gramsch, E., Muñoz, A., Langner, J., Morales, L., Soto, C., Pérez, P. and Rubio, M. A.: Black carbon transport between Santiago de Chile and glaciers in the Andes Mountains, Atmos. Environ., 232, doi:10.1016/j.atmosenv.2020.117546, 2020.

Grantz, D. A., Garner, J. H. B. and Johnson, D. W.: Ecological effects of particulate matter, Environ. Int., 29(2), 213–239, doi:https://doi.org/10.1016/S0160-4120(02)00181-2, 2003.

Gunthe, S. S., King, S. M., Rose, D., Chen, Q., Roldin, P., Farmer, D. K., Jimenez, J. L., Artaxo, P., Andreae, M. O., Martin, S. T. and Pöschl, U.: Cloud condensation nuclei in pristine tropical rainforest air of Amazonia: size-resolved measurements and modeling of atmospheric aerosol composition and CCN activity, Atmos. Chem. Phys., 9(19), 7551–7575, doi:10.5194/acp-9-7551-2009, 2009.

Gunthe, S. S., Rose, D., Su, H., Garland, R. M., Achtert, P., Nowak, A., Wiedensohler, A., Kuwata, M., Takegawa, N., Kondo, Y., Andreae, M. O. and Pöschl, U.: Cloud condensation nuclei (CCN) from fresh and aged air pollution in the megacity region of Beijing, Atmos. Chem. Phys., 11(21), 11023–11039, doi:10.5194/acp-11-11023-2011, 2011.

Gysel, M., Crosier, J., Topping, D. O., Whitehead, J. D., Bower, K. N., Cubison, M. J., Williams, P. I., Flynn, M. J., McFiggans, G. B. and Coe, H.: Closure study between chemical composition and hygroscopic growth of aerosol particles during TORCH2, Atmos. Chem. Phys., 7(24), 6131–6144, doi:10.5194/acp-7-6131-2007, 2007.

Hallquist, M., Wenger, J. C., Baltensperger, U., Rudich, Y., Simpson, D., Claeys, M., Dommen, J., Donahue, N. M., George, C., Goldstein, A. H., Hamilton, J. F., Herrmann, H., Hoffmann, T., Iinuma, Y., Jang, M., Jenkin, M. E., Jimenez, J. L., Kiendler-Scharr, A., Maenhaut, W., McFiggans, G., Mentel, T. F., Monod, A., Prévôt, A. S. H., Seinfeld, J. H., Surratt, J. D., Szmigielski, R. and Wildt, J.: The formation, properties and impact of secondary organic aerosol: current and emerging issues, Atmos. Chem. Phys., 9(14), 5155–5236, doi:10.5194/acp-9-5155-2009, 2009.

Hammer, E., Gysel, M., Roberts, G. C., Elias, T., Hofer, J., Hoyle, C. R., Bukowiecki, N., Dupont, J.-C., Burnet, F., Baltensperger, U. and Weingartner, E.: Size-dependent particle activation

properties in fog during the ParisFog 2012/13 field campaign, Atmos. Chem. Phys., 14(19), 10517–10533, doi:10.5194/acp-14-10517-2014, 2014.

Hegg, D. A., Radke, L. F. and Hobbs, P. V.: Measurements of Aitken nuclei and cloud condensation nuclei in the marine atmosphere and their relation to the DMS-cloud-climate hypothesis, J. Geophys. Res., 96(D10), doi:10.1029/91jd01870, 1991.

Heikkinen, L., Äijälä, M., Riva, M., Luoma, K., Dällenbach, K., Aalto, J., Aalto, P., Aliaga, D., Aurela, M., Keskinen, H., Makkonen, U., Rantala, P., Kulmala, M., Petäjä, T., Worsnop, D. and Ehn, M.: Long-term sub-micrometer aerosol chemical composition in the boreal forest: inter- and intra-annual variability, Atmos. Chem. Phys., 20(5), 3151–3180, doi:10.5194/acp-20-3151-2020, 2020.

Hirsikko, A., Bergman, T., Laakso, L., Dal Maso, M., Riipinen, I., Hõrrak, U. and Kulmala, M.: Identification and classification of the formation of intermediate ions measured in boreal forest, Atmos. Chem. Phys., 7(1), 201–210, doi:10.5194/acp-7-201-2007, 2007.

Horvath, H.: Aerosol - An introduction, J. Environ. Radioact., 51(1), 5–25, doi:10.1016/S0265-931X(00)00041-2, 2000.

Hoyle, C. R., Webster, C. S., Rieder, H. E., Nenes, A., Hammer, E., Herrmann, E., Gysel, M., Bukowiecki, N., Weingartner, E., Steinbacher, M. and Baltensperger, U.: Chemical and physical influences on aerosol activation in liquid clouds: a study based on observations from the Jungfraujoch, Switzerland, Atmos. Chem. Phys., 16(6), 4043–4061, doi:10.5194/acp-16-4043-2016, 2016.

Intergovernmental Panel on Climate Change (IPCC): IPCC: Climate Change 2021: The Physical Science Basis. [online] Available from: https://www.ipcc.ch/report/ar6/wg1/, 2021.

Jayne, J. T., Leard, D. C., Zhang, X., Davidovits, P., Smith, K. A., Kolb, C. E. and Worsnop, D. R.: Development of an Aerosol Mass Spectrometer for Size and Composition Analysis of Submicron Particles, Aerosol Sci. Technol., 33(1–2), 49–70, doi:10.1080/027868200410840, 2000.

Jefferson, A.: Empirical estimates of CCN from aerosol optical properties at four remote sites, Atmos. Chem. Phys., 10(14), 6855–6861, doi:10.5194/acp-10-6855-2010, 2010.

Jimenez, J. L., Jayne, J. T., Shi, Q., Kolb, C. E., Worsnop, D. R., Yourshaw, I., Seinfeld, J. H., Flagan, R. C., Zhang, X., Smith, K. A., Morris, J. W. and Davidovits, P.: Ambient aerosol sampling using the Aerodyne Aerosol Mass Spectrometer, J. Geophys. Res. Atmos., 108(D7),

doi:https://doi.org/10.1029/2001JD001213, 2003.

Jimenez, J. L., Canagaratna, M. R., Donahue, N. M., Prevot, A. S. H., Zhang, Q., Kroll, J. H., DeCarlo, P. F., Allan, J. D., Coe, H., Ng, N. L., Aiken, A. C., Docherty, K. S., Ulbrich, I. M., Grieshop, A. P., Robinson, A. L., Duplissy, J., Smith, J. D., Wilson, K. R., Lanz, V. A., Hueglin, C., Sun, Y. L., Tian, J., Laaksonen, A., Raatikainen, T., Rautiainen, J., Vaattovaara, P., Ehn, M., Kulmala, M., Tomlinson, J. M., Collins, D. R., Cubison, M. J., E., Dunlea, J., Huffman, J. A., Onasch, T. B., Alfarra, M. R., Williams, P. I., Bower, K., Kondo, Y., Schneider, J., Drewnick, F., Borrmann, S., Weimer, S., Demerjian, K., Salcedo, D., Cottrell, L., Griffin, R., Takami, A., Miyoshi, T., Hatakeyama, S., Shimono, A., Sun, J. Y., Zhang, Y. M., Dzepina, K., Kimmel, J. R., Sueper, D., Jayne, J. T., Herndon, S. C., Trimborn, A. M., Williams, L. R., Wood, E. C., Middlebrook, A. M., Kolb, C. E., Baltensperger, U. and Worsnop, D. R.: Evolution of Organic Aerosols in the Atmosphere, Science (80-.)., 326(5959), 1525–1529, doi:10.1126/science.1180353, 2009.

Jurányi, Z., Gysel, M., Weingartner, E., Bukowiecki, N., Kammermann, L. and Baltensperger, U.: A 17 month climatology of the cloud condensation nuclei number concentration at the high alpine site Jungfraujoch, J. Geophys. Res. Atmos., 116(10), doi:10.1029/2010JD015199, 2011.

Jurányi, Z., Tritscher, T., Gysel, M., Laborde, M., Gomes, L., Roberts, G., Baltensperger, U. and Weingartner, E.: Hygroscopic mixing state of urban aerosol derived from size-resolved cloud condensation nuclei measurements during the MEGAPOLI campaign in Paris, Atmos. Chem. Phys., 13(13), 6431–6446, doi:10.5194/acp-13-6431-2013, 2013.

Kalkavouras, P., Bougiatioti, A., Kalivitis, N., Stavroulas, I., Tombrou, M., Nenes, A. and Mihalopoulos, N.: Regional new particle formation as modulators of cloud condensation nuclei and cloud droplet number in the eastern Mediterranean, Atmos. Chem. Phys., 19(9), 6185–6203, doi:10.5194/acp-19-6185-2019, 2019.

Kanakidou, M., Seinfeld, J. H., Pandis, S. N., Barnes, I., Dentener, F. J., Facchini, M. C., Van Dingenen, R., Ervens, B., Nenes, A., Nielsen, C. J., Swietlicki, E., Putaud, J. P., Balkanski, Y., Fuzzi, S., Horth, J., Moortgat, G. K., Winterhalter, R., Myhre, C. E. L., Tsigaridis, K., Vignati, E., Stephanou, E. G. and Wilson, J.: Organic aerosol and global climate modelling: a review, Atmos. Chem. Phys., 5(4), 1053–1123, doi:10.5194/acp-5-1053-2005, 2005.

Karydis, V. A., Capps, S. L., Russell, A. G. and Nenes, A.: Adjoint sensitivity of global cloud droplet number to aerosol and dynamical parameters, Atmos. Chem. Phys., 12(19), 9041–9055, doi:10.5194/acp-12-9041-2012, 2012.

Kawana, K., Nakayama, T. and Mochida, M.: Hygroscopicity and CCN activity of atmospheric aerosol particles and their relation to organics: Characteristics of urban aerosols in Nagoya, Japan, J. Geophys. Res. Atmos., 121(8), 4100–4121, doi:https://doi.org/10.1002/2015JD023213, 2016.

Kerminen, V.-M., Paramonov, M., Anttila, T., Riipinen, I., Fountoukis, C., Korhonen, H., Asmi, E., Laakso, L., Lihavainen, H., Swietlicki, E., Kulmala, M. and Petäjä, T.: Cloud condensation nuclei production associated with atmospheric nucleation: A synthesis based on existing literature and new results, Atmos. Chem. Phys., 12(24), 12037–12059, doi:10.5194/acp-12-12037-2012, 2012.

Kerminen, V.-M., Chen, X., Vakkari, V., Petäjä, T., Kulmala, M. and Bianchi, F.: Atmospheric new particle formation and growth: review of field observations, Environ. Res. Lett., 13(10), 103003, doi:10.1088/1748-9326/aadf3c, 2018.

Kim, J. H., Yum, S. S., Shim, S., Kim, W. J., Park, M., Kim, J.-H., Kim, M.-H. and Yoon, S.-C.: On the submicron aerosol distributions and CCN number concentrations in and around the Korean Peninsula, Atmos. Chem. Phys., 14(16), 8763–8779, doi:10.5194/acp-14-8763-2014, 2014.

Köhler, H.: The nucleus in and the growth of hygroscopic droplets, Trans. Faraday Soc., 32(0), 1152–1161, doi:10.1039/TF9363201152, 1936.

Kroll, J. H. and Seinfeld, J. H.: Chemistry of secondary organic aerosol: Formation and evolution of low-volatility organics in the atmosphere, Atmos. Environ., 42(16), 3593–3624, doi:https://doi.org/10.1016/j.atmosenv.2008.01.003, 2008.

Kruskal, W. H. and Wallis, W. A.: Use of ranks in one-criterion variance analysis., J. Am. Stat. Assoc., 47, 583–621, doi:10.2307/2280779, 1952.

Kuang, Y., Xu, W., Tao, J., Ma, N., Zhao, C. and Shao, M.: A Review on Laboratory Studies and Field Measurements of Atmospheric Organic Aerosol Hygroscopicity and Its Parameterization Based on Oxidation Levels, Curr. Pollut. Reports, 6(4), 410–424, doi:10.1007/s40726-020-00164-2, 2020a.

Kuang, Y., He, Y., Xu, W., Zhao, P., Cheng, Y., Zhao, G., Tao, J., Ma, N., Su, H., Zhang, Y., Sun, J., Cheng, P., Yang, W., Zhang, S., Wu, C., Sun, Y. and Zhao, C.: Distinct diurnal variation in organic aerosol hygroscopicity and its relationship with oxygenated organic aerosol, Atmos. Chem. Phys., 20(2), 865–880, doi:10.5194/acp-20-865-2020, 2020b.

Kulkarni, G., Mei, F., Shilling, J. E., Wang, J., Reveggino, R. P., Flynn, C., Zelenyuk, A. and Fast, J.: Cloud Condensation Nuclei Closure Study Using Airborne Measurements Over the Southern

Great Plains, J. Geophys. Res. Atmos., 128(5), e2022JD037964, doi:https://doi.org/10.1029/2022JD037964, 2023.

Laj, P., Bigi, A., Rose, C., Andrews, E., Lund Myhre, C., Collaud Coen, M., Wiedensohler, A., Schultz, M., Ogren, J. A., Fiebig, M., Gliß, J., Mortier, A., Pandolfi, M., Petäjä, T., Kim, S.-W., Aas, W., Putaud, J.-P., Mayol-Bracero, O., Keywood, M., Labrador, L., Aalto, P., Ahlberg, E., Alados Arboledas, L., Alastuey, A., Andrade, M., Art\'\iñano, B., Ausmeel, S., Arsov, T., Asmi, E., Backman, J., Baltensperger, U., Bastian, S., Bath, O., Beukes, J. P., Brem, B. T., Bukowiecki, N., Conil, S., Couret, C., Day, D., Dayantolis, W., Degorska, A., Dos Santos, S. M., Eleftheriadis, K., Fetfatzis, P., Favez, O., Flentje, H., Gini, M. I., Gregorič, A., Gysel-Beer, M., Hallar, G. A., Hand, J., Hoffer, A., Hueglin, C., Hooda, R. K., Hyvärinen, A., Kalapov, I., Kalivitis, N., Kasper-Giebl, A., Kim, J. E., Kouvarakis, G., Kranjc, I., Krejci, R., Kulmala, M., Labuschagne, C., Lee, H.-J., Lihavainen, H., Lin, N.-H., Löschau, G., Luoma, K., Marinoni, A., Meinhardt, F., Merkel, M., Metzger, J.-M., Mihalopoulos, N., Nguyen, N. A., Ondracek, J., Peréz, N., Perrone, M. R., Petit, J.-E., Picard, D., Pichon, J.-M., Pont, V., Prats, N., Prenni, A., Reisen, F., Romano, S., Sellegri, K., Sharma, S., Schauer, G., Sheridan, P., Sherman, J. P., Schütze, M., Schwerin, A., Sohmer, R., Sorribas, M., Steinbacher, M., Sun, J., Titos, G., Tokzko, B., et al.: A global analysis of climate-relevant aerosol properties retrieved from the network of GAW near-surface observatories, Atmos. Meas. Tech. Discuss., 2020, 1–70, doi:10.5194/amt-2019-499, 2020.

Lance, S., Nenes, A., Medina, J. and Smith, J. N.: Mapping the Operation of the DMT Continuous Flow CCN Counter, Aerosol Sci. Technol., 40(4), 242–254, doi:10.1080/02786820500543290, 2006.

Lee, Y., Choi, Y., An, H., Park, J. and Ghim, Y. S.: Cluster analysis of atmospheric particle number size distributions at a rural site downwind of Seoul, Korea, Atmos. Pollut. Res., 12(6), 101086, doi:10.1016/J.APR.2021.101086, 2021.

Leng, C., Zhang, Q., Tao, J., Zhang, H., Zhang, D., Xu, C., Li, X., Kong, L., Cheng, T., Zhang, R., Wang, H. and Chen, C.: Impacts of new particle formation on aerosol Cloud Condensation Nuclei (CCN) activity in Shanghai: Case study, Atmos. Chem. Phys., 14(20), 11353–11365, doi:10.5194/acp-14-11353-2014, 2014.

Levin, E. J. T., Prenni, A. J., Palm, B. B., Day, D. A., Campuzano-Jost, P., Winkler, P. M., Kreidenweis, S. M., DeMott, P. J., Jimenez, J. L. and Smith, J. N.: Size-resolved aerosol composition and its link to hygroscopicity at a forested site in Colorado, Atmos. Chem. Phys., 14(5), 2657–2667,

doi:10.5194/acp-14-2657-2014, 2014.

Liu, P., Song, M., Zhao, T., Gunthe, S. S., Ham, S., He, Y., Qin, Y. M., Gong, Z., Amorim, J. C., Bertram, A. K. and Martin, S. T.: Resolving the mechanisms of hygroscopic growth and cloud condensation nuclei activity for organic particulate matter, Nat. Commun., 9(1), 4076, doi:10.1038/s41467-018-06622-2, 2018.

Liu, P. S. K., Deng, R., Smith, K. A., Williams, L. R., Jayne, J. T., Canagaratna, M. R., Moore, K., Onasch, T. B., Worsnop, D. R. and Deshler, T.: Transmission Efficiency of an Aerodynamic Focusing Lens System: Comparison of Model Calculations and Laboratory Measurements for the Aerodyne Aerosol Mass Spectrometer, Aerosol Sci. Technol., 41(8), 721–733, doi:10.1080/02786820701422278, 2007.

Liu, X. and Wang, J.: How important is organic aerosol hygroscopicity to aerosol indirect forcing?, Environ. Res. Lett., 5(4), 44010, doi:10.1088/1748-9326/5/4/044010, 2010.

Lloyd, S.: Least squares quantization in PCM, IEEE Trans. Inf. Theory, 28(2), 129–137, doi:10.1109/TIT.1982.1056489, 1982.

Lohmann, U. and Feichter, J.: Global indirect aerosol effects: A review, Atmos. Chem. Phys., 5(3), 715–737, doi:10.5194/acp-5-715-2005, 2005.

Lyamani, H., Olmo, F. J. and Alados-Arboledas, L.: Saharan dust outbreak over southeastern Spain as detected by sun photometer, Atmos. Environ., 39(38), 7276–7284, doi:10.1016/j.atmosenv.2005.09.011, 2005.

Lyamani, H., Olmo, F. J., Alcántara, A. and Alados-Arboledas, L.: Atmospheric aerosols during the 2003 heat wave in southeastern Spain I: Spectral optical depth, Atmos. Environ., 40(33), 6453–6464, doi:10.1016/j.atmosenv.2006.04.048, 2006.

Lyamani, H., Olmo, F. J. and Alados-Arboledas, L.: Light scattering and absorption properties of aerosol particles in the urban environment of Granada, Spain, Atmos. Environ., 42(11), 2630–2642, doi:10.1016/j.atmosenv.2007.10.070, 2008.

Lyamani, H., Olmo, F. J., Foyo, I. and Alados-Arboledas, L.: Black carbon aerosols over an urban area in south-eastern Spain: Changes detected after the 2008 economic crisis, Atmos. Environ., 45(35), 6423–6432, doi:10.1016/j.atmosenv.2011.07.063, 2011.

Lyamani, H., Fernández-Gálvez, J., Pérez-Ramírez, D., Valenzuela, A., Antón, M., Alados, I.,

Titos, G., Olmo, F. J. and Alados-Arboledas, L.: Aerosol properties over two urban sites in South Spain during an extended stagnation episode in winter season, Atmos. Environ., 62, 424–432, doi:10.1016/j.atmosenv.2012.08.050, 2012.

MacQueen, J.: Some methods for classification and analysis of multivariate observations., 1967.

McMurry, P. H.: A review of atmospheric aerosol measurements, Atmos. Environ., 34(12), 1959–1999, doi:https://doi.org/10.1016/S1352-2310(99)00455-0, 2000.

Mei, F., Setyan, A., Zhang, Q. and Wang, J.: CCN activity of organic aerosols observed downwind of urban emissions during CARES, Atmos. Chem. Phys., 13(24), 12155–12169, doi:10.5194/acp-13-12155-2013, 2013.

Meng, J. W., Yeung, M. C., Li, Y. J., Lee, B. Y. L. and Chan, C. K.: Size-resolved cloud condensation nuclei (CCN) activity and closure analysis at the HKUST Supersite in Hong Kong, Atmos. Chem. Phys., 14(18), 10267–10282, doi:10.5194/acp-14-10267-2014, 2014.

Merikanto, J., Spracklen, D. V., Mann, G. W., Pickering, S. J. and Carslaw, K. S.: Impact of nucleation on global CCN, Atmos. Chem. Phys., 9(21), 8601–8616, doi:10.5194/acp-9-8601-2009, 2009.

Minguillón, M. C., Pérez, N., Marchand, N., Bertrand, A., Temime-Roussel, B., Agrios, K., Szidat, S., van Drooge, B., Sylvestre, A., Alastuey, A., Reche, C., Ripoll, A., Marco, E., Grimalt, J. O. and Querol, X.: Secondary organic aerosol origin in an urban environment: influence of biogenic and fuel combustion precursors, Faraday Discuss., 189(0), 337–359, doi:10.1039/C5FD00182J, 2016.

Moore, R. H., Karydis, V. A., Capps, S. L., Lathem, T. L. and Nenes, A.: Droplet number uncertainties associated with CCN: an assessment using observations and a global model adjoint, Atmos. Chem. Phys., 13(8), 4235–4251, doi:10.5194/acp-13-4235-2013, 2013.

Morawska, L., Ristovski, Z., Jayaratne, E. R., Keogh, D. U. and Ling, X.: Ambient nano and ultrafine particles from motor vehicle emissions: Characteristics, ambient processing and implications on human exposure, Atmos. Environ., 42(35), 8113–8138, doi:https://doi.org/10.1016/j.atmosenv.2008.07.050, 2008.

Moreira, G. de A., Guerrero-Rascado, J. L., Bravo-Aranda, J. A., Foyo-Moreno, I., Cazorla, A., Alados, I., Lyamani, H., Landulfo, E. and Alados-Arboledas, L.: Study of the planetary boundary

layer height in an urban environment using a combination of microwave radiometer and ceilometer, Atmos. Res., 240, 104932, doi:https://doi.org/10.1016/j.atmosres.2020.104932, 2020.

Motos, G., Schmale, J., Corbin, J. C., Zanatta, M., Baltensperger, U. and Gysel-Beer, M.: Droplet activation behaviour of atmospheric black carbon particles in fog as a function of their size and mixing state, Atmos. Chem. Phys., 19(4), 2183–2207, doi:10.5194/acp-19-2183-2019, 2019.

Müller, T., Henzing, J. S., de Leeuw, G., Wiedensohler, A., Alastuey, A., Angelov, H., Bizjak, M., Collaud Coen, M., Engström, J. E., Gruening, C., Hillamo, R., Hoffer, A., Imre, K., Ivanow, P., Jennings, G., Sun, J. Y., Kalivitis, N., Karlsson, H., Komppula, M., Laj, P., Li, S.-M., Lunder, C., Marinoni, A., Martins dos Santos, S., Moerman, M., Nowak, A., Ogren, J. A., Petzold, A., Pichon, J. M., Rodriquez, S., Sharma, S., Sheridan, P. J., Teinilä, K., Tuch, T., Viana, M., Virkkula, A., Weingartner, E., Wilhelm, R. and Wang, Y. Q.: Characterization and intercomparison of aerosol absorption photometers: result of two intercomparison workshops, Atmos. Meas. Tech., 4(2), 245–268, doi:10.5194/amt-4-245-2011, 2011.

Ng, N. L., Canagaratna, M. R., Zhang, Q., Jimenez, J. L., Tian, J., Ulbrich, I. M., Kroll, J. H., Docherty, K. S., Chhabra, P. S., Bahreini, R., Murphy, S. M., Seinfeld, J. H., Hildebrandt, L., Donahue, N. M., DeCarlo, P. F., Lanz, V. A., Prévôt, A. S. H., Dinar, E., Rudich, Y. and Worsnop, D. R.: Organic aerosol components observed in Northern Hemispheric datasets from Aerosol Mass Spectrometry, Atmos. Chem. Phys., 10(10), 4625–4641, doi:10.5194/acp-10-4625-2010, 2010.

Ng, N. L., Herndon, S. C., Trimborn, A., Canagaratna, M. R., Croteau, P. L., Onasch, T. B., Sueper, D., Worsnop, D. R., Zhang, Q., Sun, Y. L. and Jayne, J. T.: An Aerosol Chemical Speciation Monitor (ACSM) for Routine Monitoring of the Composition and Mass Concentrations of Ambient Aerosol, Aerosol Sci. Technol., 45(7), 780–794, doi:10.1080/02786826.2011.560211, 2011.

O'Dowd, C. D., Hämeri, K., Mäkelä, J., Väkeva, M., Aalto, P., De Leeuw, G., Kunz, G. J., Becker, E., Hansson, H.-C., Allen, A. G., Jennings, S. G. and Kulmala, M.: Coastal new particle formation: Environmental conditions and aerosol physicochemical characteristics during nucleation bursts, J. Geophys. Res. Atmos., 107(19), doi:10.1029/2000JD000206, 2002.

Paatero, P.: The Multilinear Engine—A Table-Driven, Least Squares Program for Solving Multilinear Problems, Including the n-Way Parallel Factor Analysis Model, J. Comput. Graph. Stat., 8(4), 854–888, doi:10.1080/10618600.1999.10474853, 1999.

Paatero, P. and Hopke, P. K.: Rotational tools for factor analytic models, J. Chemom., 23(2),

91–100, doi:https://doi.org/10.1002/cem.1197, 2009.

Paatero, P. and Tapper, U.: Positive matrix factorization: A non-negative factor model with optimal utilization of error estimates of data values, Environmetrics, 5(2), 111–126, doi:https://doi.org/10.1002/env.3170050203, 1994.

Pandolfi, M., Alados-Arboledas, L., Alastuey, A., Andrade, M., Angelov, C., Artiñano, B., Backman, J., Baltensperger, U., Bonasoni, P., Bukowiecki, N., Collaud Coen, M., Conil, S., Coz, E., Crenn, V., Dudoitis, V., Ealo, M., Eleftheriadis, K., Favez, O., Fetfatzis, P., Fiebig, M., Flentje, H., Ginot, P., Gysel, M., Henzing, B., Hoffer, A., Holubova Smejkalova, A., Kalapov, I., Kalivitis, N., Kouvarakis, G., Kristensson, A., Kulmala, M., Lihavainen, H., Lunder, C., Luoma, K., Lyamani, H., Marinoni, A., Mihalopoulos, N., Moerman, M., Nicolas, J., O'Dowd, C., Petäjä, T., Petit, J. E., Marc Pichon, J., Prokopciuk, N., Putaud, J. P., Rodríguez, S., Sciare, J., Sellegri, K., Swietlicki, E., Titos, G., Tuch, T., Tunved, P., Ulevicius, V., Vaishya, A., Vana, M., Virkkula, A., Vratolis, S., Weingartner, E., Wiedensohler, A. and Laj, P.: A European aerosol phenomenology - 6: Scattering properties of atmospheric aerosol particles from 28 ACTRIS sites, Atmos. Chem. Phys., 18(11), 7877–7911, doi:10.5194/acp-18-7877-2018, 2018.

Paramonov, M., Kerminen, V.-M., Gysel, M., Aalto, P. P., Andreae, M. O., Asmi, E., Baltensperger, U., Bougiatioti, A., Brus, D., Frank, G. P., Good, N., Gunthe, S. S., Hao, L., Irwin, M., Jaatinen, A., Jurányi, Z., King, S. M., Kortelainen, A., Kristensson, A., Lihavainen, H., Kulmala, M., Lohmann, U., Martin, S. T., McFiggans, G., Mihalopoulos, N., Nenes, A., O'Dowd, C. D., Ovadnevaite, J., Petäjä, T., Pöschl, U., Roberts, G. C., Rose, D., Svenningsson, B., Swietlicki, E., Weingartner, E., Whitehead, J., Wiedensohler, A., Wittbom, C. and Sierau, B.: A synthesis of cloud condensation nuclei counter (CCNC) measurements within the EUCAARI network, Atmos. Chem. Phys., 15(21), 12211–12229, doi:10.5194/acp-15-12211-2015, 2015.

Patrón, D., Lyamani, H., Titos, G., Casquero-Vera, J. A., Cardell, C., Močnik, G., Alados-Arboledas, L. and Olmo, F. J.: Monumental heritage exposure to urban black carbon pollution, Atmos. Environ., 170, 22–32, doi:10.1016/j.atmosenv.2017.09.030, 2017.

Petters, M. D. and Kreidenweis, S. M.: A single parameter representation of hygroscopic growth and cloud condensation nucleus activity, Atmos. Chem. Phys., 7(8), 1961–1971, doi:10.5194/acp-7-1961-2007, 2007.

Petzold, A. and Schönlinner, M.: Multi-angle absorption photometry—a new method for the measurement of aerosol light absorption and atmospheric black carbon, J. Aerosol Sci., 35(4), 421–

441, doi:10.1016/J.JAEROSCI.2003.09.005, 2004.

Petzold, A., Schloesser, H., Sheridan, P. J., Arnott, W. P., Ogren, J. A. and Virkkula, A.: Evaluation of Multiangle Absorption Photometry for Measuring Aerosol Light Absorption, Aerosol Sci. Technol., 39(1), 40–51, doi:10.1080/027868290901945, 2005.

Petzold, A., Ogren, J. A., Fiebig, M., Laj, P., Li, S.-M., Baltensperger, U., Holzer-Popp, T., Kinne, S., Pappalardo, G., Sugimoto, N., Wehrli, C., Wiedensohler, A. and Zhang, X.-Y.: Recommendations for reporting "black carbon" measurements, Atmos. Chem. Phys., 13(16), 8365–8379, doi:10.5194/acp-13-8365-2013, 2013.

Pey, J., Pérez, N., Castillo, S., Viana, M., Moreno, T., Pandolfi, M., López-Sebastián, J. M., Alastuey, A. and Querol, X.: Geochemistry of regional background aerosols in the Western Mediterranean, Atmos. Res., 94(3), 422–435, doi:10.1016/j.atmosres.2009.07.001, 2009.

Pruppacher, H. R. and Klett, J. D.: Microphysics of Clouds and Precipitation, Springer Netherlands, Dordrecht., 2010.

Raatikainen, T. and Laaksonen, A.: A simplified treatment of surfactant effects on cloud drop activation, Geosci. Model Dev., 4(1), 107–116, doi:10.5194/gmd-4-107-2011, 2011.

Raoult, F.-M.: Loi générale des tensions de vapeur des dissolvants, CR Hebd. Seances Acad. Sci, 104, 1430–1433, 1887.

Rastak, N., Pajunoja, A., Acosta Navarro, J. C., Ma, J., Song, M., Partridge, D. G., Kirkevåg, A., Leong, Y., Hu, W. W., Taylor, N. F., Lambe, A., Cerully, K., Bougiatioti, A., Liu, P., Krejci, R., Petäjä, T., Percival, C., Davidovits, P., Worsnop, D. R., Ekman, A. M. L., Nenes, A., Martin, S., Jimenez, J. L., Collins, D. R., Topping, D. O., Bertram, A. K., Zuend, A., Virtanen, A. and Riipinen, I.: Microphysical explanation of the RH-dependent water affinity of biogenic organic aerosol and its importance for climate, Geophys. Res. Lett., 44(10), 5167–5177, doi:https://doi.org/10.1002/2017GL073056, 2017.

Reche, C., Querol, X., Alastuey, A., Viana, M., Pey, J., Moreno, T., Rodríguez, S., González, Y., Fernández-Camacho, R., De La Campa, A. M. S. M. S., Harrison, R. M. M., Quincey, P., De La Rosa, J., Dall'Osto, M., Prévôt, A. S. H., Hueglin, C., Harrison, R. M. M. and Quincey, P.: New considerations for PM, Black Carbon and particle number concentration for air quality monitoring across different European cities, Atmos. Chem. Phys., 11(13), 6207–6227, doi:10.5194/acp-11-6207-2011, 2011.

Rejano, F., Titos, G., Casquero-Vera, J. A., Lyamani, H., Andrews, E., Sheridan, P., Cazorla, A., Castillo, S., Alados-Arboledas, L. and Olmo, F. J.: Activation properties of aerosol particles as cloud condensation nuclei at urban and high-altitude remote sites in southern Europe, Sci. Total Environ., 762, 143100, doi:10.1016/j.scitotenv.2020.143100, 2021.

Ren, J., Zhang, F., Wang, Y., Collins, D., Fan, X., Jin, X., Xu, W., Sun, Y., Cribb, M. and Li, Z.: Using different assumptions of aerosol mixing state and chemical composition to predict CCN concentrations based on field measurements in urban Beijing, Atmos. Chem. Phys., 18(9), 6907–6921, doi:10.5194/acp-18-6907-2018, 2018.

Reutter, P., Su, H., Trentmann, J., Simmel, M., Rose, D., Gunthe, S. S., Wernli, H., Andreae, M. O. and Pöschl, U.: Aerosol- and updraft-limited regimes of cloud droplet formation: influence of particle number, size and hygroscopicity on the activation of cloud condensation nuclei (CCN), Atmos. Chem. Phys., 9(18), 7067–7080, doi:10.5194/acp-9-7067-2009, 2009.

Riemer, N., Ault, A. P., West, M., Craig, R. L. and Curtis, J. H.: Aerosol Mixing State: Measurements, Modeling, and Impacts, Rev. Geophys., 57(2), 187–249, doi:https://doi.org/10.1029/2018RG000615, 2019.

Ripoll, A., Minguillón, M. C., Pey, J., Jimenez, J. L., Day, D. A., Sosedova, Y., Canonaco, F., Prévôt, A. S. H., Querol, X. and Alastuey, A.: Long-term real-time chemical characterization of submicron aerosols at Montsec (southern Pyrenees, 1570 m a.s.l.), Atmos. Chem. Phys., 15(6), 2935–2951, doi:10.5194/acp-15-2935-2015, 2015.

Rivas, I., Beddows, D. C. S., Amato, F., Green, D. C., Järvi, L., Hueglin, C., Reche, C., Timonen, H., Fuller, G. W., Niemi, J. V, Pérez, N., Aurela, M., Hopke, P. K., Alastuey, A., Kulmala, M., Harrison, R. M., Querol, X. and Kelly, F. J.: Source apportionment of particle number size distribution in urban background and traffic stations in four European cities, Environ. Int., 135, 105345, doi:https://doi.org/10.1016/j.envint.2019.105345, 2020.

Roberts, G. C. and Nenes, A.: A continuous-flow streamwise thermal-gradient CCN chamber for atmospheric measurements, Aerosol Sci. Technol., 39(3), 206–221, doi:10.1080/027868290913988, 2005.

Robinson, A. L., Donahue, N. M., Shrivastava, M. K., Weitkamp, E. A., Sage, A. M., Grieshop, A. P., Lane, T. E., Pierce, J. R. and Pandis, S. N.: Rethinking Organic Aerosols: Semivolatile Emissions and Photochemical Aging, Science (80-.)., 315(5816), 1259–1262,

doi:10.1126/science.1133061, 2007.

Rönkkö, T., Kuuluvainen, H., Karjalainen, P., Keskinen, J., Hillamo, R., Niemi, J. V., Pirjola, L., Timonen, H. J., Saarikoski, S., Saukko, E., Järvinen, A., Silvennoinen, H., Rostedt, A., Olin, M., Yli-Ojanperä, J., Nousiainen, P., Kousa, A. and Dal Maso, M.: Traffic is a major source of atmospheric nanocluster aerosol., Proc. Natl. Acad. Sci. U. S. A., 114(29), 7549–7554, doi:10.1073/pnas.1700830114, 2017.

Rose, C., Sellegri, K., Moreno, I., Velarde, F., Ramonet, M., Weinhold, K., Krejci, R., Andrade, M., Wiedensohler, A., Ginot, P., Laj, P., Ginot, P. and Laj, P.: CCN production by new particle formation in the free troposphere, Atmos. Chem. Phys., 17(2), 1529–1541, doi:10.5194/acp-17-1529-2017, 2017.

Rose, D., Gunthe, S. S., Mikhailov, E., Frank, G. P., Dusek, U., Andreae, M. O. and Pöschl, U.: Calibration and measurement uncertainties of a continuous-flow cloud condensation nuclei counter (DMT-CCNC): CCN activation of ammonium sulfate and sodium chloride aerosol particles in theory and experiment, Atmos. Chem. Phys., 8(5), 1153–1179, doi:10.5194/acp-8-1153-2008, 2008.

Rose, D., Nowak, A., Achtert, P., Wiedensohler, A., Hu, M., Shao, M., Zhang, Y., Andreae, M. O. and Pöschl, U.: Cloud condensation nuclei in polluted air and biomass burning smoke near the mega-city Guangzhou, China – Part 1: Size-resolved measurements and implications for the modeling of aerosol particle hygroscopicity and CCN activity, Atmos. Chem. Phys., 10(7), 3365–3383, doi:10.5194/acp-10-3365-2010, 2010.

Rose, D., Gunthe, S. S., Su, H., Garland, R. M., Yang, H., Berghof, M., Cheng, Y. F., Wehner, B., Achtert, P., Nowak, A., Wiedensohler, A., Takegawa, N., Kondo, Y., Hu, M., Zhang, Y., Andreae, M. O. and Pöschl, U.: Cloud condensation nuclei in polluted air and biomass burning smoke near the mega-city Guangzhou, China – Part 2: Size-resolved aerosol chemical composition, diurnal cycles, and externally mixed weakly CCN-active soot particles, Atmos. Chem. Phys., 11(6), 2817–2836, doi:10.5194/acp-11-2817-2011, 2011.

Salimi, F., Ristovski, Z., Mazaheri, M., Laiman, R., Crilley, L. R., He, C., Clifford, S. and Morawska, L.: Assessment and application of clustering techniques to atmospheric particle number size distribution for the purpose of source apportionment, Atmos. Chem. Phys., 14(21), 11883–11892, doi:10.5194/acp-14-11883-2014, 2014.

Salma, I., Thén, W., Vörösmarty, M. and Gyöngyösi, A. Z.: Cloud activation properties of aerosol particles in a continental Central European urban environment, Atmos. Chem. Phys., 21(14), 11289–11302, doi:10.5194/acp-21-11289-2021, 2021.

Schmale, J., Henning, S., Henzing, B., Keskinen, H., Sellegri, K., Ovadnevaite, J., Bougiatioti, A., Kalivitis, N., Stavroulas, I., Jefferson, A., Park, M., Schlag, P., Kristensson, A., Iwamoto, Y., Pringle, K., Reddington, C., Aalto, P., Äijälä, M., Baltensperger, U., Bialek, J., Birmili, W., Bukowiecki, N., Ehn, M., Fjæraa, A. M., Fiebig, M., Frank, G., Fröhlich, R., Frumau, A., Furuya, M., Hammer, E., Heikkinen, L., Herrmann, E., Holzinger, R., Hyono, H., Kanakidou, M., Kiendler-Scharr, A., Kinouchi, K., Kos, G., Kulmala, M., Mihalopoulos, N., Motos, G., Nenes, A., O'Dowd, C., Paramonov, M., Petäjä, T., Picard, D., Poulain, L., Prévôt, A. S. H., Slowik, J., Sonntag, A., Swietlicki, E., Svenningsson, B., Tsurumaru, H., Wiedensohler, A., Wittbom, C., Ogren, J. A., Matsuki, A., Yum, S. S., Myhre, C. L., Carslaw, K., Stratmann, F. and Gysel, M.: Collocated observations of cloud condensation nuclei, particle size distributions, and chemical composition, Sci. Data, 4(1), 170003, doi:10.1038/sdata.2017.3, 2017.

Schmale, J., Henning, S., Decesari, S., Henzing, B., Keskinen, H., Sellegri, K., Ovadnevaite, J., Pöhlker, M., Brito, J., Bougiatioti, A., Baltensperger, U. and Gysel, M.: Long-term cloud condensation nuclei number concentration, particle number size distribution and chemical composition measurements at regionally representative observatories, Atmos. Chem. Phys., 18(4), 2853–2881, doi:10.5194/acp-18-2853-2018, 2018.

Seinfeld, J. H. and Pandis, S. N.: From air pollution to climate change, Atmos. Chem. Phys., 1326, 1998.

Seinfeld, J. H., Bretherton, C., Carslaw, K. S., Coe, H., DeMott, P. J., Dunlea, E. J., Feingold, G., Ghan, S., Guenther, A. B., Kahn, R., Kraucunas, I., Kreidenweis, S. M., Molina, M. J., Nenes, A., Penner, J. E., Prather, K. A., Ramanathan, V., Ramaswamy, V., Rasch, P. J., Ravishankara, A. R., Rosenfeld, D., Stephens, G. and Wood, R.: Improving our fundamental understanding of the role of aerosol-cloud interactions in the climate system., Proc. Natl. Acad. Sci. U. S. A., 113(21), 5781–90, doi:10.1073/pnas.1514043113, 2016.

Shen, Y., Virkkula, A., Ding, A., Luoma, K., Keskinen, H., Aalto, P. P., Chi, X., Qi, X., Nie, W., Huang, X., Petäjä, T., Kulmala, M. and Kerminen, V.-M.: Estimating CCN number concentrations using aerosol optical properties: Role of particle number size distribution and parameterization, Atmos. Chem. Phys. Discuss., 1–40, doi:10.5194/acp-2019-149, 2019.

Siegel, K., Neuberger, A., Karlsson, L., Zieger, P., Mattsson, F., Duplessis, P., Dada, L., Daellenbach, K., Schmale, J., Baccarini, A., Krejci, R., Svenningsson, B., Chang, R., Ekman, A. M. L., Riipinen, I. and Mohr, C.: Using Novel Molecular-Level Chemical Composition Observations of High Arctic Organic Aerosol for Predictions of Cloud Condensation Nuclei, Environ. Sci. \& Technol., 56(19), 13888–13899, doi:10.1021/acs.est.2c02162, 2022.

Sotiropoulou, R.-E. P., Medina, J. and Nenes, A.: CCN predictions: Is theory sufficient for assessments of the indirect effect?, Geophys. Res. Lett., 33(5), doi:https://doi.org/10.1029/2005GL025148, 2006.

Stokes, R. H. and Robinson, R. A.: Interactions in Aqueous Nonelectrolyte Solutions. I. Solute-Solvent Equilibria, J. Phys. Chem., 70(7), 2126–2131, doi:10.1021/j100879a010, 1966.

Svenningsson, B., Rissler, J., Swietlicki, E., Mircea, M., Bilde, M., Facchini, M. C., Decesari, S., Fuzzi, S., Zhou, J., Mønster, J. and Rosenørn, T.: Hygroscopic growth and critical supersaturations for mixed aerosol particles of inorganic and organic compounds of atmospheric relevance, Atmos. Chem. Phys., 6(7), 1937–1952, doi:10.5194/acp-6-1937-2006, 2006.

Thalman, R., de Sá, S. S., Palm, B. B., Barbosa, H. M. J., Pöhlker, M. L., Alexander, M. L., Brito, J., Carbone, S., Castillo, P., Day, D. A., Kuang, C., Manzi, A., Ng, N. L., Sedlacek III, A. J., Souza, R., Springston, S., Watson, T., Pöhlker, C., Pöschl, U., Andreae, M. O., Artaxo, P., Jimenez, J. L., Martin, S. T. and Wang, J.: CCN activity and organic hygroscopicity of aerosols downwind of an urban region in central Amazonia: seasonal and diel variations and impact of anthropogenic emissions, Atmos. Chem. Phys., 17(19), 11779–11801, doi:10.5194/acp-17-11779-2017, 2017.

Titos, G., Jefferson, A., Sheridan, P. J., Andrews, E., Lyamani, H., Alados-Arboledas, L. and Ogren, J. A.: Aerosol light-scattering enhancement due to water uptake during the TCAP campaign, Atmos. Chem. Phys., 14(13), 7031–7043, doi:10.5194/acp-14-7031-2014, 2014a.

Titos, G., Lyamani, H., Pandolfi, M., Alastuey, A. and Alados-Arboledas, L.: Identification of fine (PM1) and coarse (PM10-1) sources of particulate matter in an urban environment, Atmos. Environ., 89, 593–602, doi:10.1016/j.atmosenv.2014.03.001, 2014b.

Titos, G., del Águila, A., Cazorla, A., Lyamani, H., Casquero-Vera, J. A., Colombi, C., Cuccia, E., Gianelle, V., Močnik, G., Alastuey, A., Olmo, F. J. and Alados-Arboledas, L.: Spatial and temporal variability of carbonaceous aerosols: Assessing the impact of biomass burning in the urban environment, Sci. Total Environ., 578, 613–625, doi:10.1016/j.scitotenv.2016.11.007, 2017.

Tunved, P., Ström, J. and Hansson, H.-C.: An investigation of processes controlling the evolution of the boundary layer aerosol size distribution properties at the Swedish background station Aspvreten, Atmos. Chem. Phys., 4(11/12), 2581–2592, doi:10.5194/acp-4-2581-2004, 2004.

Twomey, S.: The nuclei of natural cloud formation part II: The supersaturation in natural clouds and the variation of cloud droplet concentration, Geofis. pura e Appl., 43(1), 243–249, doi:10.1007/BF01993560, 1959.

Twomey, S.: The Influence of Pollution on the Shortwave Albedo of Clouds, J. Atmos. Sci., 34(7), 1149–1152, doi:10.1175/1520-0469(1977)034<1149:TIOPOT>2.0.CO;2, 1977.

Valenzuela, A., Olmo, F. J., Lyamani, H., Antón, M., Quirantes, A. and Alados-Arboledas, L.: Aerosol radiative forcing during African desert dust events (2005-2010) over Southeastern Spain, Atmos. Chem. Phys., 12(21), 10331–10351, doi:10.5194/acp-12-10331-2012, 2012.

Varanda Rizzo, L., Roldin, P., Brito, J., Backman, J., Swietlicki, E., Krejci, R., Tunved, P., Petäjä, T., Kulmala, M. and Artaxo, P.: Multi-year statistical and modeling analysis of submicrometer aerosol number size distributions at a rain forest site in Amazonia, Atmos. Chem. Phys., 18(14), 10255–10274, doi:10.5194/acp-18-10255-2018, 2018.

Venzac, H., Sellegri, K., Villani, P., Picard, D. and Laj, P.: Seasonal variation of aerosol size distributions in the free troposphere and residual layer at the puy de Dôme station, France, Atmos. Chem. Phys., 9(4), 1465–1478, doi:10.5194/acp-9-1465-2009, 2009.

Via, M., Minguillón, M. C., Reche, C., Querol, X. and Alastuey, A.: Increase in secondary organic aerosol in an urban environment, Atmos. Chem. Phys., 21(10), 8323–8339, doi:10.5194/acp-21-8323-2021, 2021.

Wang, J., Cubison, M. J., Aiken, A. C., Jimenez, J. L. and Collins, D. R.: The importance of aerosol mixing state and size-resolved composition on CCN concentration and the variation of the importance with atmospheric aging of aerosols, Atmos. Chem. Phys., 10(15), 7267–7283, doi:10.5194/acp-10-7267-2010, 2010.

Weger, M., Heinold, B., Engler, C., Schumann, U., Seifert, A., Fößig, R., Voigt, C., Baars, H., Blahak, U., Borrmann, S., Hoose, C., Kaufmann, S., Krämer, M., Seifert, P., Senf, F., Schneider, J. and Tegen, I.: The impact of mineral dust on cloud formation during the Saharan dust event in April 2014 over Europe, Atmos. Chem. Phys., 18(23), 17545–17572, doi:10.5194/acp-18-17545-2018, 2018.

Weingartner, E., Burtscher, H. and Baltensperger, U.: Hygroscopic properties of carbon and diesel soot particles, Atmos. Environ., 31(15), 2311–2327, doi:https://doi.org/10.1016/S1352-2310(97)00023-X, 1997.

Wiedensohler, A.: An approximation of the bipolar charge distribution for particles in the submicron size range, J. Aerosol Sci., 19(3), 387–389, doi:10.1016/0021-8502(88)90278-9, 1988.

Wiedensohler, A., Wiesner, A., Weinhold, K., Birmili, W., Hermann, M., Merkel, M., Müller, T., Pfeifer, S., Schmidt, A., Tuch, T., Velarde, F., Quincey, P., Seeger, S. and Nowak, A.: Mobility particle size spectrometers: Calibration procedures and measurement uncertainties, Aerosol Sci. Technol., 52(2), 146–164, doi:10.1080/02786826.2017.1387229, 2018.

Wilks, D. S.: Statistical Methods in Atmoshperic Sciences, Stat. Methods Atmos. Sci., 617–668, 2019.

Wu, T. and Boor, B. E.: Urban aerosol size distributions: a global perspective, Atmos. Chem. Phys., 21(11), 8883–8914, doi:10.5194/acp-21-8883-2021, 2021.

Wu, Z., Zheng, J., Wang, Y., Shang, D., Du, Z., Zhang, Y. and Hu, M.: Chemical and physical properties of biomass burning aerosols and their CCN activity: A case study in Beijing, China, Sci. Total Environ., 579, 1260–1268, doi:10.1016/j.scitotenv.2016.11.112, 2017.

Wu, Z. J., Poulain, L., Birmili, W., Größ, J., Niedermeier, N., Wang, Z. B., Herrmann, H. and Wiedensohler, A.: Some insights into the condensing vapors driving new particle growth to CCN sizes on the basis of hygroscopicity measurements, Atmos. Chem. Phys., 15(22), 13071–13083, doi:10.5194/acp-15-13071-2015, 2015.

Wu, Z. J., Zheng, J., Shang, D. J., Du, Z. F., Wu, Y. S., Zeng, L. M., Wiedensohler, A. and Hu, M.: Particle hygroscopicity and its link to chemical composition in the urban atmosphere of Beijing, China, during summertime, Atmos. Chem. Phys., 16(2), 1123–1138, doi:10.5194/acp-16-1123-2016, 2016.

Yli-Juuti, T., Riipinen, N., Aalto, P. P., Nieminen, T., Maenhaut, W., Janssens, I. A., Claeys, M., Salma, I., Ocskay, R., Hoffer, A., Lmre, K. and Kulmala, M.: Characteristics of new particle formation events and cluster ions at K-puszta, Hungary, Boreal Environ. Res., 14(4), 683–698, 2009.

Zeb, B., Alam, K., Nasir, J., Mansha, M., Ahmad, I., Bibi, S., Malik, S. M. and Ali, M.: Black Carbon aerosol characteristics and radiative forcing over the high altitude glacier region of Himalaya-Karakorum-Hindukush, Atmos. Environ., 238, doi:10.1016/j.atmosenv.2020.117711, 2020.

Zhang, F., Li, Z., Li, Y., Sun, Y., Wang, Z., Li, P., Sun, L., Wang, P., Cribb, M., Zhao, C., Fan, T., Yang, X. and Wang, Q.: Impacts of organic aerosols and its oxidation level on CCN activity from measurement at a suburban site in China, Atmos. Chem. Phys., 16(8), 5413–5425, doi:10.5194/acp-16-5413-2016, 2016.

Zhang, F., Wang, Y., Peng, J., Ren, J., Collins, D., Zhang, R., Sun, Y., Yang, X. and Li, Z.: Uncertainty in Predicting CCN Activity of Aged and Primary Aerosols, J. Geophys. Res. Atmos., 122(21), 11,711-723,736, doi:10.1002/2017JD027058, 2017.

Zhang, Q., Jimenez, J. L., Canagaratna, M. R., Allan, J. D., Coe, H., Ulbrich, I., Alfarra, M. R., Takami, A., Middlebrook, A. M., Sun, Y. L., Dzepina, K., Dunlea, E., Docherty, K., DeCarlo, P. F., Salcedo, D., Onasch, T., Jayne, J. T., Miyoshi, T., Shimono, A., Hatakeyama, S., Takegawa, N., Kondo, Y., Schneider, J., Drewnick, F., Borrmann, S., Weimer, S., Demerjian, K., Williams, P., Bower, K., Bahreini, R., Cottrell, L., Griffin, R. J., Rautiainen, J., Sun, J. Y., Zhang, Y. M. and Worsnop, D. R.: Ubiquity and dominance of oxygenated species in organic aerosols in anthropogenically-influenced Northern Hemisphere midlatitudes, Geophys. Res. Lett., 34(13), doi:https://doi.org/10.1029/2007GL029979, 2007.